Wavefront curvatures: dynamic ray focusing and diffraction classification

Dissertation

with the aim of achieving a doctoral degree

at the Faculty of Mathematics, Informatics and Natural Sciences

Department of Earth Sciences

at Universität Hamburg

Submitted by Pavel Znak

from St. Petersburg, Russia

Hamburg, 2019

Accepted as Dissertation at the Department of Earth Sciences

Day of oral defense:	13.12.2019
Reviewers:	Prof. Dr. Dirk Gajewski Prof. Dr. Boris Kashtan
Chair of the Subject Doctoral Committee:	Prof. Dr. Dirk Gajewski
Dean of Faculty of MIN:	Prof. Dr. Heinrich Graener

Abstract

Seismic inversion requires various physically reasonable processing steps, including building of the starting velocity model, identification and separation of the wave modes. The most intuitive and fruitful physical interpretation of seismic waves is given by the high-frequency theory, which operates with the notions of rays and wavefronts. In this work, I concentrate on the fundamental properties of the wavefront curvatures in order to formulate the important steps necessary for the effective seismic inversion.

I formulate building of macro-velocity models as dynamic ray focusing of normal-incidence-point-waves and diffractions. It minimizes reverse-time propagated geometrical spreading at focusing time. The wavefront curvatures and the slowness vector serve as the initial conditions for the time-reversal kinematic and dynamic extrapolation. When compared to the conventional wavefront tomography, where data are fitted on the registration surface, the new objective functional contains a single physical quantity and depends only on the velocity model. This significantly decreases the size of the inversion matrix and improves the data/unknowns ratio leading to a well-conditioned and stable inversion with fully relaxed regularization. The gradient of objective functional is computed using the ray perturbation theory, in terms of Fréchet derivatives or alternatively in terms of the adjoint dynamic ray tracing operator. Anticipating potential of ray focusing tomography in anisotropic media, I develop a reduced ray perturbation theory in the wavefront-orthonormal coordinates.

Besides the velocity model building, I aim at identification of edge and point diffractions to separate them for a subsequent dedicated processing. Edge diffractions are produced by geological structures such as faults, highly curved folds, cracks, and stratigraphic traps. Small-scale inhomogeneities and tips produce point diffractions. I complement the wavefront curvature based classification of wave phenomena by formulating a missing criterion for diffraction from an arbitrarily oriented and possibly curved edge. Additionally, I propose a new method, also based on the wavefront curvatures, for sorting seismic traces into specific groups in order to get ray focusing of edge diffractions during back propagation. This is a premise for including edge diffractions in ray focusing tomography.

Extracting the wavefront curvatures from recorded data is also of great importance. The conventional common-reflection-surface (CRS) method exploits an amplitude-coherency analysis of the vertical component. However, all three vector components of the elastic wavefield are often recorded during seafloor or land surveys. To account for this data redundancy, I generalize the conventional method. The new multicomponent CRS performs a vector-semblance optimization. The component weights are determined with a local polarization approximation. The proposed approach not only results in enhancing the data by a more physically accurate stacking, but it also enables to automatically pick the central polarization and polarization derivatives in offset and midpoint directions. These new polarization attributes turn out to be closely related to the wavefront curvatures. They have many potential applications, including building of the local velocity model at the receiver side, which can subsequently be used for constraining the global velocity model building.

Zusammenfassung

Seismische Inversion erfordert eine Reihe an physikalisch sinnvollen Verarbeitungsschritten, darin eingeschlossen die Verwendung eines guten anfänglichen Geschwindigkeitsmodells und die Identifikation und Trennung der Wellenmoden. Die intuitivste und am meisten gewinnbringende Interpretation seismischer Wellen, in Hinsicht auf ihre physikalische Eigenschaften, ist durch die Hochfrequenzapproximation gegeben, welche durch das Konzept von Strahlen und Wellenfronten geprägt ist. In dieser Arbeit konzentriere ich mich auf die grundlegenden Eigenschaften der Wellenfrontkrümmungen, um die wichtigen Schritte zu formulieren, die zu einer effektiven seismischen Inversion führen.

Ich fasse die Bildung von Makro-Geschwindigkeitsmodellen als dynamische strahlenbasierte Fokussierung von Normal-Incidence-Point Wellen und Diffraktionen auf. Das minimiert die sich in umgekehrter Zeit ausbreitende geometrische Streuung bei der Fokussierungszeit. Die Krümmungen von Wellenfronten und der Langsamkeitsvektor dienen als feste Anfangsbedingungen für die kinematische und dynamische Extrapolation in Rückwärtsrichtung. Im Vergleich zur konventionellen Wellenfronttomographie, bei der die Anpassung der modellierten Daten an die seismischen Daten an der Registrierungsoberfläche stattfindet, wird das neue Zielfunktional durch eine einzige physikalische Größe parametrisiert und hängt demzufolge nur vom Geschwindigkeitsmodell ab. Dies verringert signifikant die Größe der Inversionsmatrix und verbessert das Verhältnis zwischen Messdaten und Unbekannten, was zu einer gut konditionierten und stabilen Inversion ohne Anwendung von üblichen Regularisierungsverfahren führt. Der Gradient der Zielfunktion wird mit Hilfe der Strahlstörungstheorie berechnet, im Hinblick auf die Fréchet Ableitungen, oder alternativ mit Hilfe des adjungierten Operators der dynamischen Strahlverfolgung. Das Potenzial von Strahlfokussierungstomographie in anisotropen Medien betrachtend, entwickle ich einen Ansatz für eine sogenannte reduzierte Störungstheorie der Strahlverfolgung, wobei ich das wellenfrontorthonormale Koordinatensystem benutze.

Neben der Bildung von Geschwindigkeitsmodellen befasse ich mich mit der Identifizierung und Trennung von Punkt- und Kantendiffraktionen, um eine speziell auf sie zugeordnete Bearbeitung zu ermöglichen. Kantendiffraktionen werden durch geologische Strukturen wie Verwerfungen, hochgebogene Falten, Risse und stratigraphische Fallen erzeugt. Kleinskalige Inhomogenitäten und Spitzen erzeugen Punktdiffraktionen. Ich ergänze die, auf der Wellenfrontkrümmung basierte, Klassifikation der Wellenkomponenten durch ein neues Kriterium für Diffraktionen entstehend durch willkürlich ausgerichtete und gekrümmte Kanten. Zusätzlich schlage ich ein neues Verfahren vor, welches ebenfalls auf den Krümmungen von Wellenfronten basiert, um seismische Spuren in bestimmte Gruppen einzuordnen. Dadurch wird eine Strahlenfokussierung von Kantendiffraktionen während der Backpropagation möglich. Dies ist eine Voraussetzung für die Benutzung von Kantendiffraktionen in der Strahlfokussierungstomographie.

Das Extrahieren der Wellenfrontkrümmungen aus seismischen Daten ist ebenfalls von großer Bedeutung. Das konventionelle Common-Reflection-Surface (CRS) -Verfahren nutzt

dafür eine Kohärenzanalyse. Üblicherweise werden dabei nur die Amplituden der vertikalen Komponente der aufgezeichneten Verschiebung berücksichtigt. Oft werden bei See- und Landseismik allerdings alle drei Komponenten des Verschiebungsvektors der elastischen Welle aufgezeichnet. Ich verallgemeinere daher die herkömmliche Kohärenzanalyse im CRS-Verfahren, um alle Komponenten des Verschiebungsvektors zu berücksichtigen. Das neue mehrkomponenten CRS-Verfahren führt eine vektorielle Semblance-Optimierung durch. Die Gewichte der Komponenten werden durch eine lokale Näherung der Polarisation bestimmt. Der vorgeschlagene Ansatz führt nicht nur dazu, dass die seismischen Spuren genauer und physikalisch korrekter gestapelt werden, sondern ermöglicht auch eine automatische Auswahl von Polarisation und räumlichen Polarisationsableitungen in Offset- und Mittelpunktrichtung. Es zeigt sich, dass die neuen Polarisationsattribute in einem engen Zusammenhang mit den Wellenfrontkrümmungen stehen. Diese Attribute haben viele potenzielle Anwendungen, einschließlich der Bildung lokaler Geschwindigkeitsmodelle auf Empfängerseite. Dies kann anschließend als Einschränkung beim Erstellen des globalen Geschwindigkeitsmodells verwendet werden.

Contents

List of Figures

1 Introduction

Seismic waves is the main source of information about the Earth interior. Contemporary technologies allow one to register and store broadband seismic signals. At first glance, to utilize them at a time seems tempting and promising. How wonderful it could be, to create a magic box converting the recorded data to detailed and geologically plausible subsurface models. Many work has been done on this way towards inversion of the full waveforms (for a comprehensive review see the paper by Virieux and Operto (2009)). However, it still remains a very subtle ill-posed and ill-conditioned problem. Primarily, the full-waveform inversion is very sensitive to the quality of the initial models. For successful convergence, it may be necessary to start from a seismic velocity model, which is already accurate up to the wavelength. Secondly, different wave modes, e.g., the reflected and diffracted component of the wavefield, exhibit different propagation properties, such as diverse intensity and illumination. This results in different sensitivity of the wavefield constituents to subsurface parameters (e.g., Dell et al., 2019), which needs to be compensated by a waveform separation.

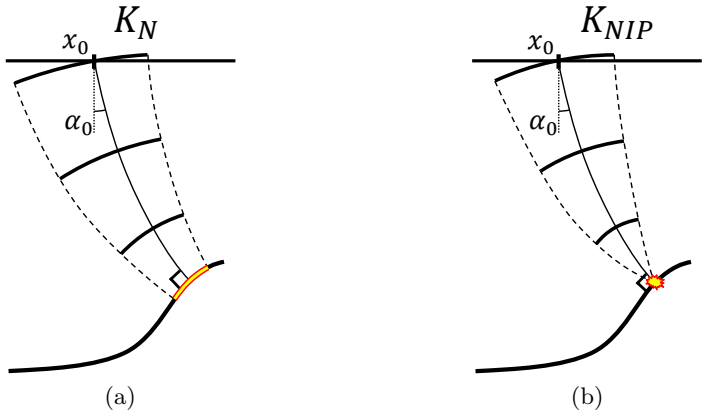

Figure 1.1: Two hypothetical eigenwaves: N-wave (a) is triggered by exploding reflector. NIP-wave (b) is excited by a point source at the normal-incidence-point (NIP) on the reflector. Curvature of the eigenfronts, K_N and K_{NIP}, is extracted from seismic data.

Multiparameter and multidimensional stacking techniques routinely serve for preconditioning of zero-offset stacks (Mann et al., 1999; Jäger et al., 2001; Landa et al., 2010; Fomel and Kazinnik, 2013) and pre-stack data (Baykulov and Gajewski, 2009; Hoecht et al., 2009), i.e., for trace regularization and signal-to-noise ratio (S/N) enhancement. In addition to that, stacking framework produces physically meaningful wavefront attributes. In other words, the wavefront attributes are extracted from unmigrated seismic data. In this thesis, I mainly concentrate on the zero-offset wavefront attributes. To give them exact meaning, we first need to discuss two eigenwaves, hypothetical wavefronts defined by Hubral (1983). "N-wave" is a fictitious wave that is triggered by the exploding reflector element (Figure

1.1a). Another fictitious wave induced by a source placed at the normal-incidence-point (NIP) on the reflector is called NIP-wave (Figure 1.1b). These imaginary waves are eigenwaves in a sense that they are sufficient to describe local behavior of the actual two-way reflected wave, including its traveltime and geometrical spreading. The zero-offset wavefront attributes in the 3D case are eight quantities. Two of them are horizontal components of the zero-offset slowness vector, which is common for both N- and NIP-wave. Other six quantities represent the second-order derivatives of the eigenwave traveltimes. Since matrices composed of the second-order derivatives can be transformed into the wavefront curvature matrices, I often use the term "wavefront curvature matrix" for both matrices. Since the wavefront attributes locally characterize the wavefronts, they can be utilized for various steps in seismic processing, among others true-amplitude migration (Hubral, 1983), velocity model building (Duveneck, 2004; Dell et al., 2014; Bauer et al., 2017; Diekmann et al., 2019), and diffraction separation (Dell and Gajewski, 2011; Berkovitch et al., 2009; Asgedom et al., 2013; Rad et al., 2018).

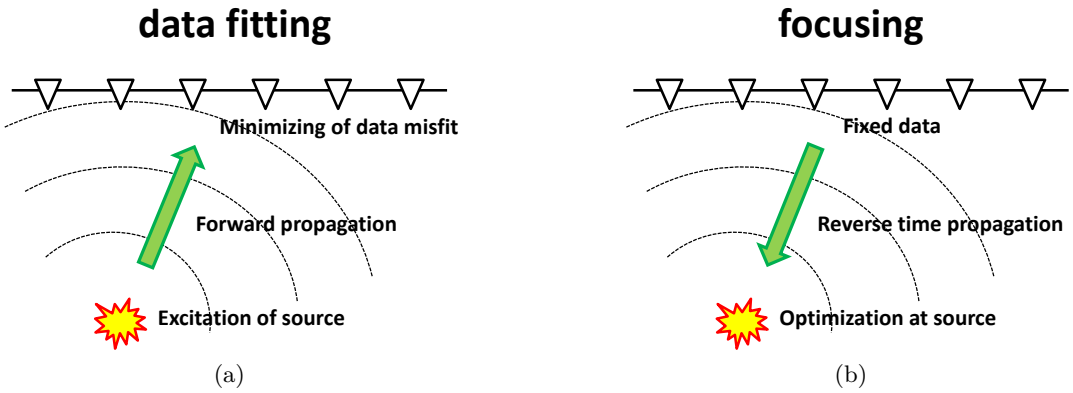

Figure 1.2: Two approaches in the velocity model building: conventional – fitting in the data domain (a); new – focusing in the depth domain (b).

1.1 Wavefront curvatures for velocity model building

A reliable and fast tomographic workflow for building smooth velocity models is of great importance for full-waveform inversion and depth migration. It is, however, usually ill-conditioned and requires regularization (Hansen, 1998; Costa et al., 2008; Chavent, 2010). Applying regularization reduces resolution of the resulting velocity models. A smaller size of the inversion matrix would relax the regularization. Furthermore, a rule of thumb for the least-squares optimization states that the amount of data points should significantly exceed the amount of unknowns.

I categorize the velocity model building methods into two major classes: methods fitting data on the registration surface and methods that optimize a quantity in depth, which is computed with extrapolation of measurements into the subsurface (see Figure 1.2). Let us briefly outline the milestones in both directions.

Bishop et al. (1985) formulated reflection tomography as a nonlinear least-squares problem of minimizing misfits between modeled and measured traveltimes with respect to veloci-

ties and depth coordinates of continuous reflectors. Stereotomography proposed by Billette and Lambaré (1998) introduced spatial positions and dips of reflector elements as independent unknowns corresponding to the source-receiver pairs. In addition to times, the objective functional was complemented with misfits of emergence coordinates and slopes. To incorporate the wavefront attributes as an extra input, Duveneck (2004) extended the objective functional by adding misfits of the wavefront curvatures. The space of unknowns, inherited from stereotomography, consisted of the velocity model and the independent reflector elements. Note in this method, the wavefront attributes are modeled with upward kinematic and dynamic ray tracing from the reflector elements to the registration surface (Figure 1.2a).

The methods optimizing an objective functional in depth are formulated mostly in the image domain. It has been recognized that flattening of migrated reflections with respect to the source-receiver offsets indicates a velocity model which is consistent with data. First, Al-Yahya (1989) introduced this idea for the common receiver gathers after shot migration. Stork (1992) developed a migration velocity analysis in common image gathers, produced by independent imaging of common offset gathers. Chauris et al. (2002) and Nguyen et al. (2008) later described the curved events in common image gathers as being composed of locally coherent ones with dips to be minimized.

Comparing to the standard tomographic methods in the data domain, migration velocity analysis has an advantage since the velocity model plays the role of the single unknown during the inversion. Redundant and pick-dependent coordinates and dips of the scattering elements are not present in the set of unknowns. On the other hand, data-domain tomographic methods don't require multiple runs of depth migration, which still may be computationally costly. Moreover, picking in the migrated domain for geologies with complex internal stratigraphy, including high velocity contrasts, folds, and multiple faulting such as salt rollers, is a challenging task.

Accordingly, this thesis regards velocity model building by means of wave focusing in depth (Figure 1.2b) rather than fitting data on the registration surface (Figure 1.2a). Inversion based on the wave focusing optimizes a measure of focusing in the subsurface. A focusing measure is computed with reverse time extrapolation of data. In the process of focusing, the observed data are not predicted but serve as the boundary conditions for the back propagation of rays. This is very efficient if compared to the multiple runs of depth migration.

1.2 Wavefront curvatures for diffraction classification

The second application of the wavefront curvatures, which I am concentrated on, is wave type classification. Under classification, I assume data-driven automatic identification of wave modes in the seismic sections. Generally speaking, body waves can be categorized according to dimensionality of scatterers. In the 3D formulation, commonly used specular reflections are scattered by 2D boundaries between the geological formations. Intermediate 1D objects, present in such geological structures as faults, highly curved folds, cracks, or pinch-outs, response as edge diffractions. Finally, Null-D small-scale inhomogeneities or tips produce point diffractions. I aim to distinguish not only between the diffracted and reflected components, but also between diffractions of different kinds. This would pave a way to advanced waveform and attribute separation and subsequent dedicated processing.

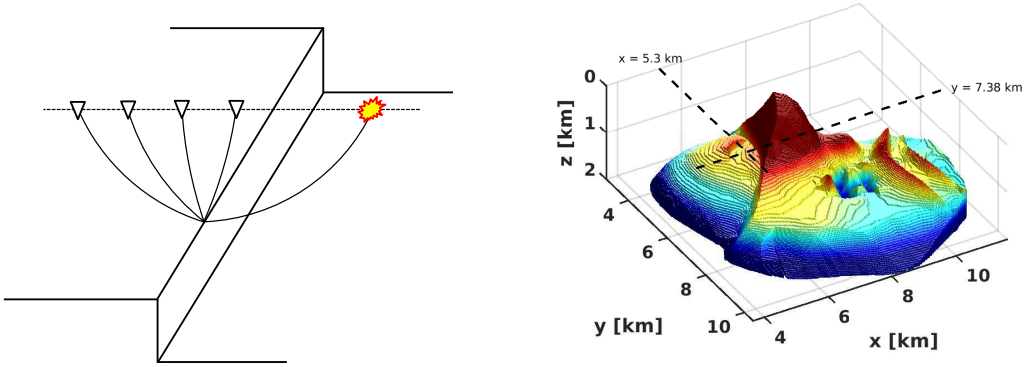

(a) (b)

Figure 1.3: Edge diffractors: (a) scetch of a 3D acquisition, where the 2D criterion is fulfilled; (b) topography of the salt body with edge diffractors in the SEG/EAGE model.

The criterion for identifying point diffraction in 3D media by fronts of the NIP- and N-wave considers that both matrices of wavefront curvatures fully coincide. This follows from the fact of full coincidence of the eigenfronts in this case. The same criterion holds for 2D diffraction, where the matrices of wavefront curvatures reduce to the scalar curvatures. Dell and Gajewski (2011); Rad et al. (2018) applied this equality condition to identify and separate diffractions from reflections using a binary reflection filter. Berkovitch et al. (2009); Asgedom et al. (2013) used the coherent summation along diffraction traveltimes to enhance diffracted events. This implies the reflected amplitudes to be incoherently summed up along the stacking operator, which is parametrized in terms of the single wavefront curvature. Schwarz (2019) proposed an adaptive filter exploiting the coherent data summation and subtraction based on the wavefront attributes. All the methods, either based on coherent summation and subtraction or on binary filtering, allow for discriminating diffracted waves, for separating them from the reflected ones, and for a dedicated diffraction processing (see e.g., in Alonaizi et al., 2013; Bauer et al., 2017; Dell et al., 2018; Keydar and Landa, 2019; Yin and Nakata, 2019).

Moreover, both a point and an edge diffractor produce kinematically equivalent responses in the 2D case (see e.g., in Dell et al., 2018). This means the wavefront curvatures are equal independently of the type of the diffracting object and the same separation criterion can be used to isolate both point and edge diffraction. In the 3D case, however, response of an edge diffractor differs from response of a point diffractor. The 2D criterion holds only for particular edge types and acquisition symmetry. For instance, an orthogonal to the edge acquisition line is illustrated in Figure 1.3a. However, if we look at the topography of the realistic geological body, as in Figure 1.3b, we clearly see the pronounced inclined and curved edge structures. This is the top of salt in the famous synthetic SEG/EAGE model. These edge diffractors definitely scatter large amount of seismic energy, which naturally needs special processing.

In this work, arbitrarily oriented curved edges are considered. I give a criterion to identify them formulating in terms of the eigenwave curvature matrices. I assume edge diffractors to be embedded in a 3D anisotropic and heterogeneous medium. To justify the criterion, I

perform numerical tests, correspondingly, in a heterogeneous and in an anisotropic environment. Additionally, I verify the method using realistic wavefront attributes extracted from the SEG/EAGE dataset.

I also develop a technique for including the edge diffractions in tomography based on the focusing principle. Kinematic focusing in reverse time implies minimizing distances between endpoints of back propagated rays. For point diffractions, this method requires tagging of individual diffractions (Bauer et al., 2019). For edge diffractions, it is not sufficient. Additionally, it requires grouping of receivers in a special way that they are back projected to single points on the edge. I formulate the method of grouping using the wavefront curvatures. The fundamentals of this approach are closely related to the edge diffraction identification criterion.

Structure of the thesis

The thesis is composed of four papers prepared for publication in top rank scientific journals. Accordingly, they follow the introductory **Chapter 1**, which outlines basic concepts of the subject, using wavefront curvatures in applied seismics.

Chapter 2 – the paper "Velocity model building by dynamic ray focusing". In this paper, I formulate a new approach of macro-velocity model building using the zero-offset wavefront attributes for time-reversal dynamic ray tracing and for minimizing of geometrical spreading.

Chapter 3 – the paper "Ray perturbation theory in wavefront-orthonormal coordinates: generally anisotropic 3D elastic solids". This auxiliary work establishes and examines an alternative formulation of the ray perturbation theory in anisotropic media. The ray perturbation theory serves for Fréchet derivatives computing in velocity model building.

Chapter 4 – the paper "Identification and focusing of edge diffractions with wavefront attributes". It gives a new criterion based on wavefront curvatures allowing to distinguish seismic events between point diffractions, edge diffractions, and reflections. Additionally, an original approach for edge diffraction focusing is formulated.

Chapter 5 – the paper "Polarization-consistent stacking of multicomponent seismic data". This paper generalizes the conventional common-reflection-surface method in order to incorporate the multicomponent seismic data using vector coherency analysis and new polarization attributes related to the wavefront curvatures.

In **Chapter 6**, results of the thesis are summarized and major conclusions are given. Finally, I outlook future potential benefits and the road ahead in **Chapter 7**. For convenience of a reader, appendices of the papers comprising many technical details are given at the end of the thesis in the corresponding order.

Contributions of co-authors

Direct content comprising the prepared papers was generated mostly by myself. However, the papers appeared as a result of intensive collaboration of all co-authors. Prof. Dr. Dirk Gajewski usually outlines broad picture of the problem and shares his vision based on physical intuition motivating other members of the group. When a result is achieved, he participates in continuous and critical discussions supervising the work. When a significant

result is achieved, he makes tremendous efforts improving structure and readability of my texts to emphasize the added value. Prof. Dr. Boris Kashtan usually enjoys theory and makes significant contributions to mathematical aspects of the problem. Having a strong background in wave physics, he always tries to make initially vague ideas sufficiently rigorous and clear. Dr. Sergius Dell, in addition to the continuous discussions and proofreading of papers, makes a contribution to testing of the developed methods by modeling and data processing.

2 Velocity model building by dynamic ray focusing

Abstract

We formulate and examine a method of tomography by dynamic ray focusing of normal-incidence-point-waves and diffractions. Dynamic ray focusing minimizes reverse time propagated geometrical spreading of individual rays at focusing time. Slopes and wavefront curvatures serve as fixed initial conditions for the time-reversal kinematic and dynamic extrapolation. The method is essentially local, i.e., it requires only short offsets. The new objective functional contains a single physical quantity and depends only on the velocity model. When compared to conventional methods fitting data on the registration surface, this significantly decreases the size of the inversion matrix and improves the data/unknowns ratio. Moreover, there is no need to balance different physical quantities. Thus, the proposed method includes advantages of the image domain tomographies but is formulated in the data domain. We provide expressions for computing the gradient of the objective functional in terms of Fréchet derivatives of the geometrical spreading and also in terms of the adjoint dynamic ray tracing operator. We successfully apply the approach, combined with a quasi-Newton solver, to synthetic data containing a salt body. We also tested it on a field data example which includes complex salt tectonics. The reverse time migration reveals well-focused salt rollers and dipping events. In all provided examples, no regularization was required, which confirms that the new method is well-conditioned and stable.

2.1 Introduction

A reliable and fast tomographic workflow for building smooth velocity models is of great importance for subsequent depth migration or full-waveform inversion, which benefits from geologically reasonable initial velocity models. Seismic tomography, however, is ill-conditioned. Stable inversion usually requires regularization, which reduces resolution of the velocity models (Hansen, 1998; Costa et al., 2008; Chavent, 2010). A smaller size of the inversion matrix leads to a better conditioning and stability of the algorithm. Moreover, a stable and unique inversion usually requires an amount of data that significantly exceeds the amount of unknowns.

With respect to formulation of the inversion problem, we categorize the methods into two major classes: methods fitting data on the registration surface and methods that optimize a quantity in depth, which is computed with extrapolation of measurements to the subsurface.

Bishop et al. (1985) formulated reflection tomography as a nonlinear least-squares problem of minimizing misfits between modeled and measured traveltimes with respect to velocities and depth coordinates of continuous reflectors. Stereotomography proposed by Billette

and Lambaré (1998) introduced spatial positions and dips of reflector elements as independent unknowns corresponding to source-receiver pairs. In addition to times, the objective functional was complemented with misfits of emergence coordinates and slopes.

Duveneck (2004) extended the objective functional of stereotomography by adding extra misfits of the wavefront curvatures. This wavefront tomography uses kinematics of the one-way normal-incidence-point (NIP) waves, which are triggered by point sources located at the normal-incidence-points on a reflector. The space of unknowns, inherited from stereotomography, consists of the velocity model and independent reflector elements. Individual rays are traced from the reflector elements, which is followed by computing the wavefront curvatures with dynamic ray tracing. In the domain of time-migrated reflections, additional wavefront curvatures of vertically arriving image-rays can be picked and also utilized for the depth velocity model building (Dell et al., 2014). The wavefront attributes including slopes and curvatures of NIP-waves can be extracted, e.g., by the zero-offset hyperbolic or non-hyperbolic common-reflection-surface (CRS) stack (Jäger et al., 2001; Dell et al., 2012; Fomel and Kazinnik, 2013).

Stereotomography undoubtedly has an advantage over wavefront tomography with respect to illumination by rays since it is formulated for broader, finite-offset, data (see, e.g., a detailed comparison of the two methods in Dümmong et al., 2008). However, for point diffractions, the total ray coverage doesn't depend on available source-receiver offsets (Bauer et al., 2016). Because of the back scattering, any ray of the diffracted event is a zero-offset ray and the moveout is preserved in the stacking process. Using the wavefront attributes of diffractions complementary to reflections, thus, has the potential to increase illumination. Due to this fact, the interest in using diffractions in inversion and velocity model building for challenging geological areas increased (Bauer et al., 2017).

For the methods, which optimize an objective functional formulated in depth, we first refer to the work by Sword (1986). He suggested utilizing data domain slopes as fixed initial conditions for subsurface ray extrapolation. In his implementation, the objective functional measures lateral distance between source- and receiver-rays at depth corresponding to the two-way traveltime. However, further approaches have been developed mostly in the image domain. It has been recognized that flattening of migrated reflections with respect to the source-receiver offsets indicates a velocity model which is consistent with data. First, Al-Yahya (1989) introduced this idea for the common receiver gathers after shot migration. Stork (1992) developed migration velocity analysis in common image gathers produced by independent imaging of common offset gathers. Chauris et al. (2002) and Nguyen et al. (2008) later described the curved events in common image gathers as being composed of locally coherent ones with dips to be minimized. They also introduced picking of slopes, required for the stereotomography, in the image domain.

Comparing to the standard tomographic methods in the data domain, migration velocity analysis has an advantage since the velocity model plays the role of the single unknown during the inversion. Redundant and pick-dependent coordinates and dips of the scattering elements are not present in the set of unknowns. On the other hand, data-domain tomographic methods don't require multiple runs of depth migration, which still may be computationally costly. Moreover, picking in the migrated domain for geologies with complex internal stratigraphy, including high velocity contrasts, folds, and multiple faulting such as salt rollers, is a challenging task.

This motivated us to study velocity model building by means of wave focusing in depth

rather than fitting data on the registration surface. Under focusing, we assume a process that optimizes a focusing measure in the subsurface. This measure is computed with reverse time extrapolation of data. In the process of focusing, the observed data are not predicted but serve as boundary conditions for the back propagation of rays which is very efficient if compared to multiple runs of depth migration. Lellouch and Landa (2018) also applied a time-reversal focusing criterion for velocity model building but with full waveforms. It was implemented for a crosswell acquisition with a priori known positions of the sources. A global optimization was based on the time symmetry of focusing. Another kind of inverse problem reformulation to reduce the number of unknowns was recently presented by Sambolian et al. (2019). The authors revised the slope tomography to parametrize it with the velocity model as the only unknown. They used the fact that for a given trial velocity model the reflecting elements can be determined and therefore depend on the velocity model. For the wavefront tomography, both concepts were previously formulated by Znak et al. (2017, 2018).

The adjoint-state method efficiently computes the gradient of the objective functional (Plessix, 2006). Initially introduced to applied seismics in the context of full-waveform inversion (Virieux and Operto, 2009), the adjoint-state approach has found its path to many other techniques including transmission and reflection tomographies (Leung and Qian, 2006; Tavakoli et al., 2017).

In this paper, we present a ray tomography based on the physical principle of focusing with dynamic ray tracing. As the measure of focusing, we use geometrical spreading propagated back in time to the scatterers in depth. The method utilizes traveltimes, slopes, and wavefront curvatures as input. During the inversion, they remain fixed at the acquisition surface and serve as initial conditions for kinematic and dynamic time-reversal ray tracing. Minimization of spreading is equivalent to shrinking the wavefront or maximizing the amplitude. Therefore, the new method lies in-between kinematics and dynamics: using the dynamic objective functional but picking the necessary data from wavefront curvatures and not from amplitudes. The inverse problem turns out to be naturally parametrized by the velocity model as the only unknown similarly to the method of Sword (1986). It significantly decreases the inversion matrix dimension and considerably improves the data/unknowns ratio if compared to the conventional wavefront tomography. The proposed formulation of the objective functional is shortened and exhibits a straightforward computing of gradient with the adjoint-state method. We successfully apply it, in a combination with the quasi-Newton L-BFGS-B iterative optimization (Byrd et al., 1995), to the inversion of a synthetic salt body model and also to a challenging field data example comprising complex salt neotectonics. The new approach does not require weight balancing of different physical quantities in the objective functional since velocity is the sole inversion parameter. Moreover, it allows an inversion without extra regularizing terms. Both features are crucial for getting reproducible results.

2.2 Theory and method

We formulate velocity model building as dynamic ray focusing. This implies a reverse time extrapolation of dynamic characteristics along the rays to the subsurface and minimization of geometrical spreading at scattering locations. This is equivalent to maximizing focusing

amplitude and forcing a wavefront to shrink to a point. Focusing is relevant for diffractions and reflections. According to the NIP-wave theorem (Chernjak and Gritsenko, 1979; Fomel and Grechka, 2001), reflection moveout can locally be associated with diffraction moveout. In this sense, we can think of a reflector as being composed of point diffractors, each of which backscatters in a narrow sector orthogonal to the reflector. These virtual diffractions are called NIP-waves (Hubral, 1983).

The proposed tomographic method relies on well determined wavefront attributes. These are the zero-offset one-way traveltimes, the zero-offset slopes and curvatures of the wave fronts. The attributes are determined from multiparameter stacking operators. In heterogeneous media it is essential to apply the operators locally, i.e., with small offsets and midpoint displacements. Under these conditions, wavefront attributes can be reliably determined even in the case of strong heterogeneity (Xie and Gajewski, 2019). We employ the zero-offset CRS stacking techniques to automatically extract characteristics of the wavefront from seismic records.

2.2.1 Unsupervised determination of wavefront attributes

Common-reflection-surface (CRS) stacking improves the signal-to-noise ratio by utilizing the inherent redundancy of seismic data. However, this multiparameter and multidimensional method works also as a convenient tool for an automatic extraction of kinematic wavefield characteristics. In 2D, the CRS stacking domain is spanned by the scalar half-offset, $h = \frac{1}{2}(x_r - x_s)$, and the scalar midpoint displacement, $\triangle x_m = x_m - x_0$, $x_m = \frac{1}{2}(x_r + x_s)$. Here, x_s and x_r stand for the lateral coordinates of the source and receiver, and x_0 denotes the coordinate of the central midpoint. A local traveltime approximation is used to detect coherent events in the data domain and to determine their wavefront attributes. For instance, the hyperbolic CRS approximation (Jäger et al., 2001) centered at midpoint x_0 reads

$$t^2(\triangle x_m, h) = (t_0 + 2\,p_x \triangle x_m)^2 + 2\,t_0 \left(M_{NIP}^{(x)}\, h^2 + M_N^{(x)} \triangle x_m^2 \right), \tag{2.1}$$

where t_0 is two-way traveltime along the central ray, and p_x stands for horizontal slowness of the central ray (slope). Interpretation of two other parameters, $M_{NIP}^{(x)}$ and $M_N^{(x)}$, relies on two imaginary experiments. The NIP-wave is a hypothetical wave that is generated by a point source at the NIP location. The N-wave is the second hypothetical wave that is triggered by exploding the CRS (the reflector segment). Respectively, second traveltime derivatives of these waves with respect to the lateral coordinate are denoted as $M_{NIP}^{(x)}$ and $M_N^{(x)}$. Wavefront attributes, p_x, $M_{NIP}^{(x)}$, and $M_N^{(x)}$, are determined during the coherency analysis for every time sample and midpoint location. Picked automatically using a coherency criterion, they comprise the input of wavefront tomography and dynamic ray focusing.

N-wavefront curvatures are not required for the velocity model building in the current paper. However, they can be used for the diffraction separation. If a 2D diffraction is considered, the wavefront attributes describe the actual wavefront with $M_{NIP}^{(x)} = M_N^{(x)}$. This allows the independent treatment of diffractions and reflections during the tomographic inversion (Dell and Gajewski, 2011; Bauer et al., 2017, 2019). It is important to note that diffractions should be properly considered already in preprocessing, i.e., prestack data enhancement and denoising, trace regularization, and interpolation should acknowledge

steep dips (Xie and Gajewski, 2017).

To formulate the inversion in a concise way, we express the second-derivative attribute $M_{NIP}^{(x)}$ w.r.t. the ray-centered coordinate system and get the dynamic ray tracing quantity M_{NIP} (e.g., Červený, 2001). It is linearly related to the wavefront curvature through the surface velocity: $K_{NIP} = vM_{NIP}$. For the sake of readability, we often refer to M_{NIP} as to wavefront curvature. If the surface velocity is assumed to be locally homogeneous, then it is sufficient to have a value of the emergence angle α to determine M_{NIP}: $M_{NIP}^{(x)} = \cos^2\alpha\, M_{NIP}$ (e.g., Duveneck, 2004). The cosine is obtained from the slope attribute and the value of the surface velocity ($p_x = \sin\alpha/v$).

Further throughout the paper, we will omit the subscripts "$_{NIP}$" and "$_0$" and assume a discrete data set of N_{data} picks $\{x_i, t_i, p_{xi}, M_i\}_{i=1}^{N_{data}}$ for the inversion, where for the i-th pick, x_i is the central midpoint coordinate, p_{x_i} and M_i are the slope and NIP-curvature attributes, and t_i is one-way traveltime from the corresponding scattering point (normal-incidence-point or diffractor) to the central midpoint with the coordinate x_i.

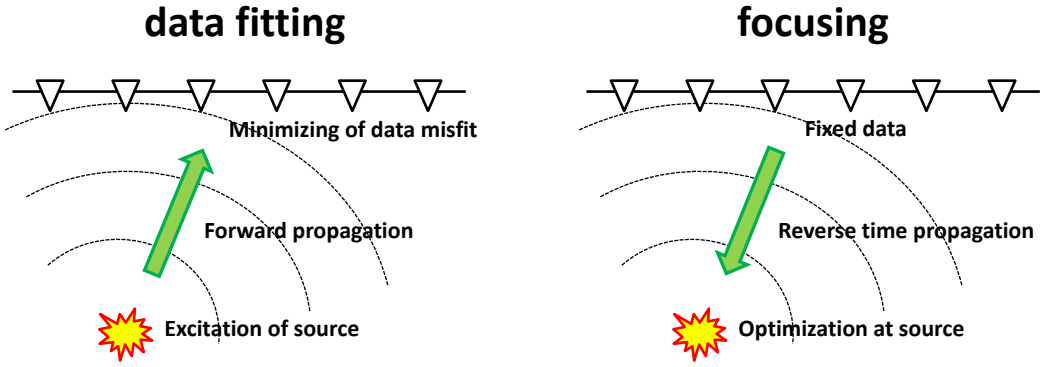

Figure 2.1: The concept of focusing used for formulating the inverse problem. Instead of fitting in the data domain, a quantity controlling focusing is minimized in the depth domain. It is computed in a trial velocity model by reverse time propagation while keeping the data input fixed and used as boundary (initial) conditions.

2.2.2 Dynamic ray focusing

Dynamic ray focusing represents a novel variant of the currently used wavefront tomography (Duveneck, 2004; Dell et al., 2014; Bauer et al., 2017). Our goal is to achieve a natural formulation of the inverse problem with an optimization conducted solely in the velocity model parameter space. This means, we aim at deriving an objective functional which depends on the data vector and the velocity only, in order to remove redundant unknowns describing the scatterer positions and scattering angles. Such functional would increase stability and reliability of the inversion.

We understand the general concept of focusing as minimizing a measure of focusing in depth. For a trial subsurface model, the focusing quantity is computed with reverse time propagation. The data input serves as initial (boundary) conditions for the back propagation, i.e., it is not predicted in each iteration step. Focusing is illustrated in comparison to the standard data fitting formulation in Figure 4.4.

Both, the auxiliary NIP-waves and the 2D diffractions are kinematically equivalent to waves triggered by the corresponding point sources in the subsurface. Therefore, in a velocity model consistent with the data, their geometrical spreading vanishes when propagated back in time up to the excitation. We simultaneously minimize the geometrical spreading of all NIP- and/or diffracted waves picked in the data domain. This implies fixing the wavefront attributes p_{xi}, M_i and using them as initial conditions for the kinematic and dynamic time-reversal ray tracing from the midpoint location x_i until the time interval t_i is reached. Each attribute pick of the data set $\{x_i, t_i, p_{xi}, M_i\}_{i=1}^{N_{data}}$ is considered independently, corresponding to an individual ray. Because of the time translation invariance, we consider all rays being triggered in the subsurface at the same reference time $t = 0$ and arriving at the registration surface with coordinates x_i, slope p_{xi}, and curvature M_i at time t_i. The ray tracing is performed for the i-th pick starting from the time t_i at the surface until the reference time $t = 0$ is reached in the subsurface, where the focusing occurs (Figure 2.2).

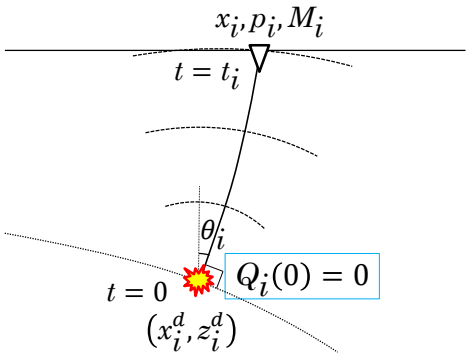

Figure 2.2: The principle of the dynamic ray focusing. The reverse time propagated geometrical spreading Q vanishes at the reference time $t = 0$ for each pick. The wavefront attributes p_{xi} and M_i are fixed during the optimization and serve as initial conditions for the time-reversal kinematic and dynamic ray tracing from the midpoint with coordinate x_i at time $t = t_i$ to the scatterer (NIP or diffractor) at time $t = 0$.

Reverse time kinematic ray tracing provides a ray $\mathbf{x}(t)$ and its corresponding slowness $\mathbf{p}(t)$. Dynamic ray tracing along the ray is formulated as a solution of a linear homogeneous system of ordinary differential equations (e.g., Červený, 2001)

$$\frac{d}{dt}\begin{pmatrix} Q \\ P \end{pmatrix} = S\begin{pmatrix} Q \\ P \end{pmatrix}, \quad S = \begin{pmatrix} 0 & v^2 \\ -\frac{v_{qq}}{v} & 0 \end{pmatrix} \tag{2.2}$$

with respect to the geometrical spreading of rays $Q = \left(\frac{\partial \mathbf{x}}{\partial \gamma}, \mathbf{e}_q\right)$ and the geometrical spreading of slowness $P = \left(\frac{\partial \mathbf{p}}{\partial \gamma}, \mathbf{e}_q\right)$, where γ is a ray coordinate complementary to time t, $\mathbf{e}_q$ is a basis vector of the ray-centered coordinate system, v and v_{qq} stand for the velocity and its second-derivative with respect to the ray-centered coordinate. Geometrical spreading is related to the Jacobian of the mapping from the ray coordinates to the Cartesian coordinates, $J = \frac{\partial(x_1, x_2)}{\partial(t, \gamma)} = vQ$, and affects amplitude and phase of the zero-order ray series approximation by the factor $\frac{1}{\sqrt{J}}$.

We now specify the initial conditions for the dynamic ray tracing. Q and P on a ray are defined up to the multiplication with a constant that depends on the ray-fan parametrization, specifying the ray-coordinate γ. If we choose a common parametrization with a shooting angle around the source in depth, the corresponding dynamic ray tracing quantities $Q_i^d(t_i)$ and $P_i^d(t_i)$ ("^{d}" for the parametrization in depth) of the one-way upgoing wave do not appear in the set of wavefront attributes. However, the wavefront curvature attribute is related to them since $M_i = P_i^d(t_i)/Q_i^d(t_i)$. Although tracing of the M-quantity is theoretically possible by solving the Riccati equation (e.g., Červený, 2001), it is challenging due to the unlimited growth in the vicinity of the point sources and caustics. Therefore, we will nevertheless use system 2.2 but apply parametrization scaling to cope with this difficulty. With the help of the determined wavefront curvature, we are able to extrapolate geometrical spreading that is normalized at the acquisition line with initial conditions

$$Q_i(t_i) = 1, \qquad P_i(t_i) = M_i Q_i(t_i) = M_i \tag{2.3}$$

for each pick. The acquisition-normalized geometrical spreading corresponds to the ray-fan parametrization with length of the emerging wavefront.

For the time-reversal extrapolation, we use a propagator matrix of the dynamic ray tracing system that is computed backwards in time ($t < t_i$) to the subsurface

$$\Pi_i(t, t_i) = \begin{pmatrix} Q_i^{(1)}(t, t_i) & Q_i^{(2)}(t, t_i) \\ P_i^{(1)}(t, t_i) & P_i^{(2)}(t, t_i) \end{pmatrix}, \qquad \Pi_i(t_i, t_i) = I, \tag{2.4}$$

where I stands for the identity matrix. Correspondingly, the time reverse propagated acquisition-normalized dynamic quantities are expressed as follows:

$$\begin{pmatrix} Q_i(t) \\ P_i(t) \end{pmatrix} = \Pi_i(t, t_i) \begin{pmatrix} 1 \\ M_i \end{pmatrix}. \tag{2.5}$$

To avoid a confusion, we consider elements of the propagator $Q^{(1)}$ and $P^{(2)}$ to have no units, which results in the following units for the remaining elements: $[P^{(1)}] = [M]$, $[Q^{(2)}] = [1/M]$. If we now look at the propagator representation for the dynamic quantities Q_i^d and P_i^d, we immediately conclude that they are proportional to the acquisition-normalized pair Q_i and P_i:

$$\begin{pmatrix} Q_i^d(t) \\ P_i^d(t) \end{pmatrix} = \Pi_i(t, t_i) \begin{pmatrix} Q_i^d(t_i) \\ P_i^d(t_i) \end{pmatrix} = Q_i^d(t_i) \begin{pmatrix} Q_i(t) \\ P_i(t) \end{pmatrix}. \tag{2.6}$$

The quotient equals the value of the depth-parametrized spreading at the registration line.

Regardless of ray-fan parametrization, geometrical spreading has to vanish at the source time for a velocity model consistent with the data. Accordingly, we introduce an objective functional as a sum over all data picks of squared acquisition-normalized geometrical spreading that is reverse time propagated:

$$J[v] = \frac{1}{2} \sum_{i=1}^{N_{data}} Q_i^2(0), \qquad Q_i(0) = Q_i^{(1)}(0, t_i) + Q_i^{(2)}(0, t_i) M_i. \tag{2.7}$$

We refer to minimization of this functional with respect to the velocity model as dynamic ray focusing. During the convergence of velocity model, reflector elements and diffractors

are localized as well. The simplest example of the cost functional, in the homogeneous medium, is illustrated in Appendix A.1.

Following Duveneck (2004), we describe the velocity model by B-spline functions of 4-th order distributed on the rectangular $N_z \times N_x$ grid of nodes:

$$v = \sum_{j=1}^{N_z} \sum_{k=1}^{N_x} v_{jk} \beta_j(z) \beta_k(x). \tag{2.8}$$

The extent of the basis functions is directly related to the grid spacing since the sequences of grid coordinates (lateral and in-depth) are used as nodes to define the B-splines. Additionally, we extrapolate the grid out of the model by relating the outer node values with node values at the boundary of the model. This makes the velocity model homogeneous in the case of equal coefficients v_{jk}, having no decay at the boundaries. The order of the B-splines is chosen to achieve continuity of the 3rd derivative in the Cauchy problem for the dynamic ray tracing perturbations.

Since we describe the model in terms of rather smooth B-splines and optimize only in the velocity space, we could avoid any additional smoothing by regularization terms (e.g., Costa et al., 2008) for all examples presented in this paper. Scaling the mesh from coarse to fine plays a role of regularization by model parametrization (Chavent, 2010). If we make the grid even more denser, inversion would naturally require a regularizing functional, which would decrease the expected resolution. When we reduce the number of grid nodes, we automatically extend the basis functions and introduce an additional smoothing of the model.

To stabilize inversion and avoid local minima of the objective functional, it can be augmented with an additional term based on a priory information constraining the velocity model for certain regions, such as the earth surface or water column. We apply optimization by the L-BFGS-B algorithm (Byrd et al., 1995), which is a quasi-Newton method, i.e., it uses values of the gradient to approximate the Hessian of the objective functional.

2.2.3 Comparing the focusing and the data fitting tomography

The wavefront tomography (Duveneck, 2004) is formulated as a higher-order extension of a sequence of tomographic data-domain fitting approaches, such as traveltime tomography (Bishop et al., 1985) and stereotomography (Lambaré, 2008). It utilizes zero-offset curvatures instead of times and slopes. An objective functional

$$J(\mathbf{m}) = \sum_{i=1}^{N_{data}} (x_i - x_i(\mathbf{m}_i))^2 + \sum_{i=1}^{N_{data}} (t_i - t_i(\mathbf{m}_i))^2 + \sum_{i=1}^{N_{data}} (p_{xi} - p_{xi}(\mathbf{m}_i))^2 + \sum_{i=1}^{N_{data}} (M_i - M_i(\mathbf{m}_i))^2 \tag{2.9}$$

illustrates this method. Implementations may vary depending on the considered set of attributes, emergence angle α instead of slowness p_x, second-derivative of traveltime in Cartesian coordinates $M^{(x)}$ instead of M in ray-centered coordinates. However with respect to the settings of the inverse problem, the functional remains a sum of squared attribute misfits over N_{data} wavefront attribute picks. Thus, it is a data fitting method (Figure 4.4). Also, dimension calibration of physically different quantities is necessary as well as additional constraints. A vector of unknowns $\mathbf{m}$ comprises coordinates x_i^d, z_i^d of scatterers

(reflector elements and diffractors) and zero-offset ray scattering angles θ_i for each pick (see Figure 2.2) together with the velocity model as described in equation 2.8. For the i-th pick, predicted attributes depend on a reduced vector $\mathbf{m}_i = (x_i^d, z_i^d, \theta_i^d, \mathbf{v})$, where $\mathbf{v}$ is used to denote a set of model defining coefficients v_{jk}.

This implies $4N_{data}$ data quantities and $3N_{data} + N_z N_x$ unknowns. A block of the wavefront tomography inversion matrix for one pick with number i

$$\begin{pmatrix} \frac{\partial t_i}{\partial x_i^d} & \frac{\partial t_i}{\partial z_i^d} & \frac{\partial t_i}{\partial \theta_i} & \frac{\partial t_i}{\partial v_{11}} & \frac{\partial t_i}{\partial v_{21}} & \cdots & \frac{\partial t_i}{\partial v_{N_z N_x}} \\ \frac{\partial x_i}{\partial x_i^d} & \frac{\partial x_i}{\partial z_i^d} & \frac{\partial x_i}{\partial \theta_i} & \frac{\partial x_i}{\partial v_{11}} & \frac{\partial x_i}{\partial v_{21}} & \cdots & \frac{\partial x_i}{\partial v_{N_z N_x}} \\ \frac{\partial p_{xi}}{\partial x_i^d} & \frac{\partial p_{xi}}{\partial z_i^d} & \frac{\partial p_{xi}}{\partial \theta_i} & \frac{\partial p_{xi}}{\partial v_{11}} & \frac{\partial p_{xi}}{\partial v_{21}} & \cdots & \frac{\partial p_{xi}}{\partial v_{N_z N_x}} \\ \frac{\partial M_i}{\partial x_i^d} & \frac{\partial M_i}{\partial z_i^d} & \frac{\partial M_i}{\partial \theta_i} & \frac{\partial M_i}{\partial v_{11}} & \frac{\partial M_i}{\partial v_{21}} & \cdots & \frac{\partial M_i}{\partial v_{N_z N_x}} \end{pmatrix} \tag{2.10}$$

is significantly larger than a block of the dynamic ray focusing inversion matrix corresponding to the same pick

$$\begin{pmatrix} \frac{\partial Q_i}{\partial v_{11}} & \frac{\partial Q_i}{\partial v_{21}} & \cdots & \frac{\partial Q_i}{\partial v_{N_z N_x}} \end{pmatrix}. \tag{2.11}$$

The dynamic ray focusing is an inversion with N_{data} data-vector dimension and the $N_z \times N_x$ - dimensional space of unknown velocity coefficients. Reducing dimensions of the inversion matrix is crucial for conditioning the problem.

Moreover, in the wavefront tomography, the number of unknowns directly depends on the number of data picks. Adding a pick to the data set automatically appends three additional unknowns describing position and angle of scattering. In the best case, when the number of data picks N_{data} significantly exceeds the number of velocity grid nodes, $N_z \times N_x$, it leads to a ratio of the number of data points and the number of unknowns equal to $\frac{4}{3}$. When a higher velocity sampling is considered, it leads to even smaller ratios close to one. Usually, least-squares problems should be highly overdetermined. The more independent data values are present, the higher is the ratio of the number of data points and the number of unknowns, the more stable is the inversion. This is not achievable with the currently used variant of wavefront tomography. However, with dynamic ray focusing we can choose any grid node spacing for a given data amount, naturally adjusting the acceptable resolution.

Optimization in the focusing approach is naturally performed on parameters sharing the same physical dimension. When regularization is applied, it concerns all the present unknowns. Additionally, the new approach doesn't need adjustments by weights controlling the misfits of different physical quantities. Such a reduction of adjustable parameters leads to easily reproducible results.

2.2.4 Fréchet derivatives of geometrical spreading and adjoint-state method

Fréchet derivative of the objective functional 2.7 can be expressed through Fréchet derivatives of the reverse time propagated geometrical spreading as

$$\triangle J = \sum_{i=1}^{N_{data}} Q_i(0) \triangle Q_i(0). \tag{2.12}$$

To calculate perturbations of the dynamic quantities, we apply the linear differential equations system given by Farra and Madariaga (1987) for the ray-centered description of rays that are paraxial to the rays in the perturbed medium:

$$\frac{d}{dt}\begin{pmatrix}\triangle Q\\ \triangle P\end{pmatrix} = S\begin{pmatrix}\triangle Q\\ \triangle P\end{pmatrix} + \triangle S\begin{pmatrix}Q\\ P\end{pmatrix}, \qquad \triangle S = S_{q,p} + S_{\triangle v},$$

$$S_{q,p} = \begin{pmatrix} 2vv_qp & 2vv_qq \\ \left(\frac{3}{v^2}v_qv_{qq} - \frac{1}{v}v_{qqq}\right)q & -2vv_qp \end{pmatrix}, \qquad S_{\triangle v} = \begin{pmatrix} 0 & v\triangle v \\ -\left(\frac{\triangle v}{v}\right)_{qq} + \frac{v_{qq}}{v^2}\triangle v & 0 \end{pmatrix}, \quad (2.13)$$

where $q(t)$ and $p(t)$ are the ray-centered coordinate and slowness of the perturbed ray, correspondingly. They are evaluated by means of another linear differential equations system with the same matrix S:

$$\frac{d}{dt}\begin{pmatrix}q\\ p\end{pmatrix} = S\begin{pmatrix}q\\ p\end{pmatrix} + \begin{pmatrix}0\\ \frac{v_q}{v^2}\triangle v - \frac{1}{v}(\triangle v)_q\end{pmatrix}. \quad (2.14)$$

The perturbations $\triangle Q_i$ and $\triangle P_i$ have zero initial conditions because the downward propagator is the identity matrix at $t = t_i$ regardless of a velocity model and because M_i is a fixed number determined from the data (see equation 5.1). The reverse ray starting point is fixed at the receiver and $q_i(t_i) = 0$. If the surface velocity remains unchanged, $p_i(t_i)$ approaches zero as well, $p_i(t_i) = 0$. In principle, we can relax this constraint and use an initial condition (see Appendix A.2)

$$p_i(t_i) = \frac{1}{v(x_i,0)}\frac{p_{xi}}{\sqrt{1 - v^2(x_i,0){p_{xi}}^2}}\triangle v(x_i,0). \quad (2.15)$$

The inhomogeneous system 2.13 is solved with the propagator of the homogeneous one (see, e.g, Gilbert and Backus, 1966), which results in an expression for computing the Fréchet derivative of the geometrical spreading:

$$\triangle Q_i(0) = \begin{pmatrix}Q_i^{(1)}(0,t_i)\\ Q_i^{(2)}(0,t_i)\end{pmatrix}^T \int_{t_i}^{0} \Pi_i^{-1}(t,t_i)\triangle S_i(t)\begin{pmatrix}Q_i(t)\\ P_i(t)\end{pmatrix} dt. \quad (2.16)$$

Due to symplecticity, the inverse of the propagator matrix is computed as follows (e.g., Červený, 2001):

$$\Pi_i^{-1}(t,t_i) = \begin{pmatrix} P_i^{(2)}(t,t_i) & -Q_i^{(2)}(t,t_i) \\ -P_i^{(1)}(t,t_i) & Q_i^{(1)}(t,t_i) \end{pmatrix}. \quad (2.17)$$

If we now combine equations 2.12 and 2.16 bringing the multipliers to the integrand, we obtain the derivative of the objective functional in the form of the adjoint-state method (e.g., Plessix, 2006; Chavent, 2010):

$$\triangle J = \sum_{i=1}^{N_{data}} \int_{t_i}^{0} \begin{pmatrix}\lambda_i^Q & \lambda_i^P\end{pmatrix}\triangle S_i\begin{pmatrix}Q_i\\ P_i\end{pmatrix} dt, \quad (2.18)$$

where the adjoint-state variables are computed as

$$\begin{pmatrix} \lambda_i^Q(t) \\ \lambda_i^P(t) \end{pmatrix} = Q_i(0)\Pi^{-1T}(t, t_i) \begin{pmatrix} Q_i^{(1)}(0, t_i) \\ Q_i^{(2)}(0, t_i) \end{pmatrix}. \tag{2.19}$$

With initial conditions $\lambda_i^Q(0) = Q_i(0)$ and $\lambda_i^P(0) = 0$, they represent a solution of a linear system of differential equations

$$\frac{d}{dt} \begin{pmatrix} \lambda_Q \\ \lambda_P \end{pmatrix} = -S^T \begin{pmatrix} \lambda_Q \\ \lambda_P \end{pmatrix}. \tag{2.20}$$

This system is adjoint to the dynamic ray tracing system 2.2. In focusing, state variable is a reverse time propagated quantity, from receivers to the subsurface, whereas the adjoint "field" turns out to be a result of forward propagation. See Appendix A.3 for more details on adjoint dynamic ray tracing and a standard derivation of these equations.

Fréchet derivative 2.18 for a fixed reference velocity model is a linear functional with respect to the velocity perturbation. Perturbing a single node value in the model (see equation 2.8), we express the components of the gradient of the objective functional as the Fréchet derivative applied to the corresponding 2D basis function:

$$\frac{\partial J}{\partial v_{jk}} = \triangle J[\beta_j(z)\beta_k(x)]. \tag{2.21}$$

2.2.5 Ray focusing of diffractions in 3D

In 2D, traveltime responses of point and edge diffractions are equivalent. However in 3D, we should distinguish and treat them differently to account carefully for such objects as faults, highly curved folds, fractures, and pinch-outs. Particularly, this is crucial for velocity model building by ray focusing. Diffractions can be focused in reverse time not only with the dynamic ray focusing, but also kinematically by minimizing distances between endpoints of rays belonging to the same subsurface locations (Bauer et al., 2019). In the latter case, no curvature information is needed. For point diffractions, this method requires tagging of individual diffractions. For edge diffractions, it is necessary to group receivers in a special way that they are back projected to single points on the edge.

Normal-wave attributes are available even in case of absent source-receiver offsets, for instance, in p-cable data acquired with limited length streamers or in ground penetrating radar data. In contrast to point diffractions, a matrix representing the N-front curvature of edge diffractions essentially differs from the one representing the NIP-front. The initial conditions for upward dynamic ray tracing differ depending on the type of fictitious wave. Moreover, in case of a smoothly bent edge, the initial conditions contain unknown values of curvature and torsion of the edge as a space curve. This complicates application of the conventional wavefront tomography to the N-wave attributes of edge diffractions. Fortunately, geometrical spreading vanishes on the edge both for the NIP- and for the N-wave as the ray tube collapses. This makes the dynamic ray focusing suitable for inversion of the N-wave attributes of point and edge diffractions in 3D.

2.3 Synthetic data example

An acoustic land streamer data set of primary reflections was modeled by the Seismic Unix Gaussian beam routine for a salt body velocity model shown in Figure 2.6b. We used a 40 Hz zero-phase Ricker wavelet as a source function. Gaussian noise with $SNR = 20$ was added to the traces. A total number of 641 midpoints is considered by positioning sources and receivers with a 50 m spacing. First, we performed CRS processing to determine the wavefront attributes with a maximum offset aperture of 2 km, which implies a maximum CMP fold of 21. Figure 2.3a shows the stack section. Horizontal slowness and wavefront curvature were picked from the resulting attribute sections (Figure 2.4) with a criterion of coherence threshold. The coherence section is given in Figure 2.3b. Small rhombuses indicate pick locations serving as input for the inversion.

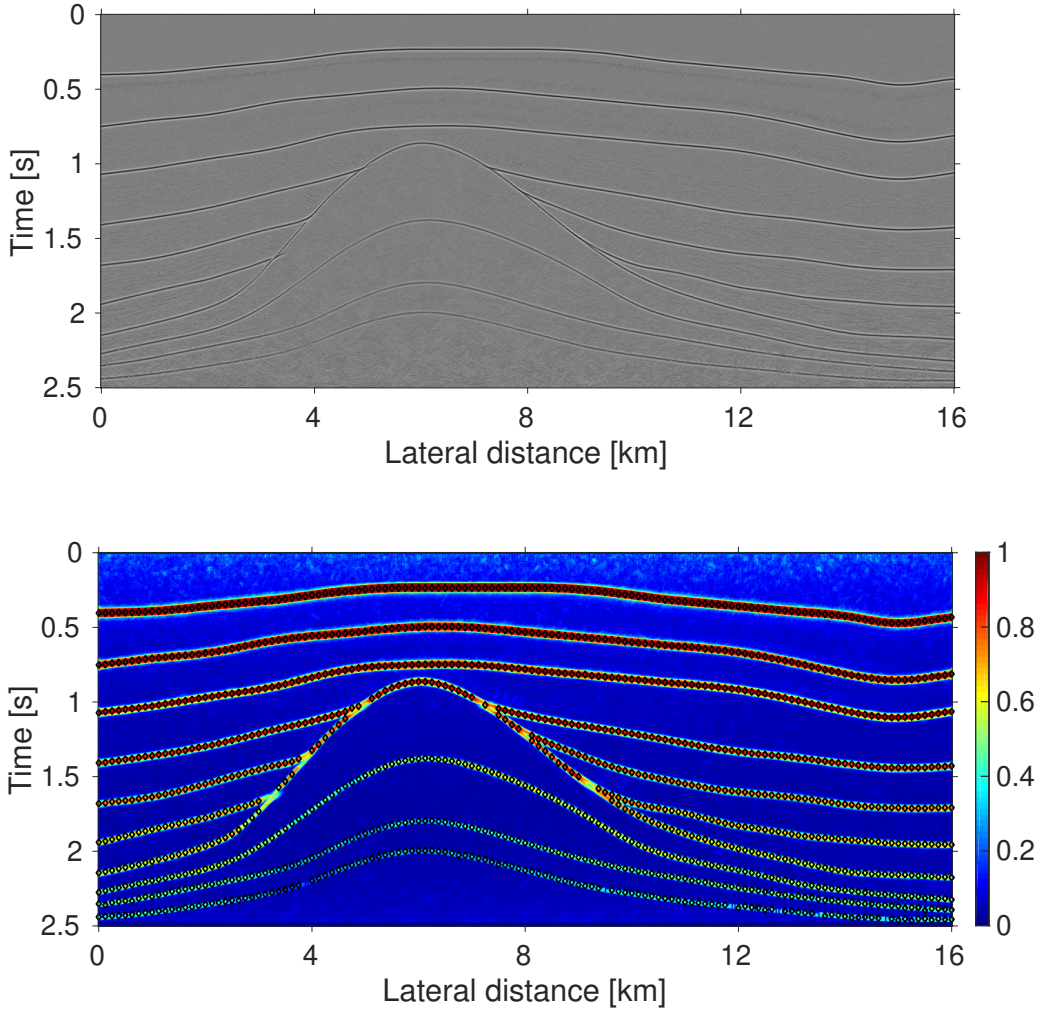

Figure 2.3: Common-reflection-surface stack of synthetic data (a) and corresponding coherence section overlaid with picks (black diamonds) used for the inversion (b).

1166 picks were utilized for dynamic ray focusing using an 21×21 grid of 4-th order

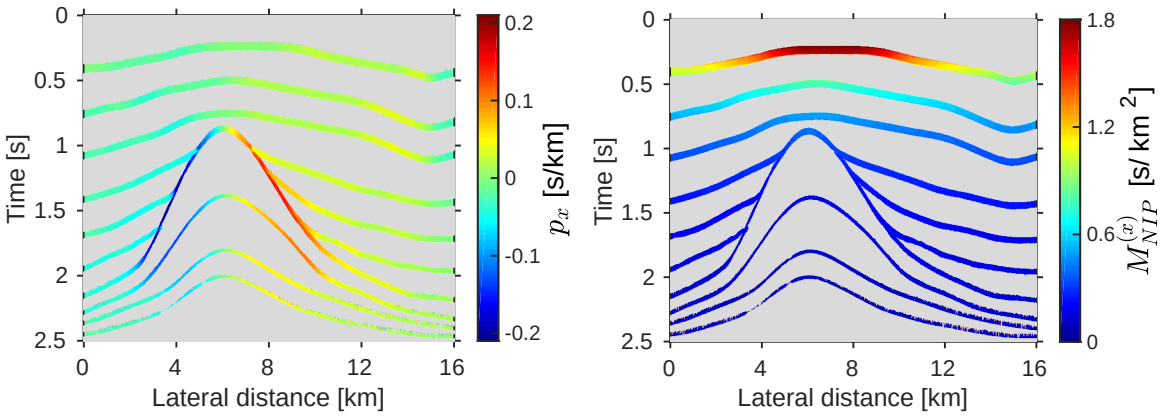

Figure 2.4: Wavefront attributes: horizontal slowness (a) and wavefront curvature (b) sections determined from the synthetic data using the CRS processing.

B-spline nodes with 800 m lateral and 175 m vertical spacing. The initial model was a constant gradient velocity growing from 2.2 km/s at the surface to 4.4 km/s for the base of salt. This velocity interval was also used to define bounds for the L-BFGS-B algorithm. We point-wise constrained the surface velocity by adding a misfit term to the objective functional and its gradient. No regularizing terms were added. This was possible due to the significant reduction of the inversion matrix in the dynamic ray focusing approach (see matrices 2.10 and 2.11). Quantitatively, the ratio between dimension of the data vector and dimension of the unknown vector was approximately 2.6 for the dynamic ray focusing and 1.3 for the conventional formulation. We stopped the inversion process after 55 iterations. Convergence can be tracked in Figure 2.5 that shows the decreasing functional and its gradient maximum norm. Figure 2.6a illustrates the final velocity model. Eventually, ray tracing in the retrieved tomographic model localized the reflector elements at the normal-incidence-point locations.

We observe high correlation of the smooth model with the synthetic one, except the last poorly illuminated layer of the salt body. The reflector elements also reliably reproduce the original structure. We superimposed them onto the original layered velocity model (see Figure 2.6b) to control the quality. Due to the B-spline smoothing of the strong impedance contrast at the top of the salt body, we can see slight deviations of the reflector locations.

2.4 Field data example

In this section, we apply the new tomographic scheme to a marine field data set. We first briefly describe the acquisition area and the complexity of its geological regime. Then we discuss the inversion process and show the final velocity model. At the end of the section, we provide depth images produced by reverse time migration, to demonstrate the performance of the proposed velocity model building.

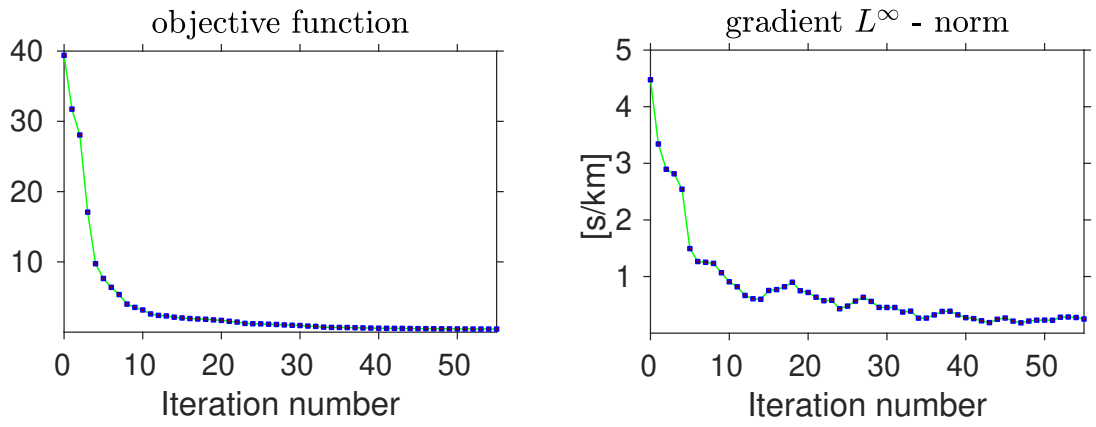

Figure 2.5: Descent of the objective functional (a) and its gradient maximum norm (b) during the dynamic ray focusing of the synthetic data.

2.4.1 Acquisition area and wavefront attributes

The marine data were acquired in the central Levant Basin, located in the Eastern Mediterranean, which is bounded to the South by the Egyptian and to the East by the Levant coast and reaches to the Cyprus Arc and the Eratosthenes Seamount in the North and West, respectively. The data cover the so-called Messinian Evaporites, which are relatively young salt formations. They precipitated during the Messinian Salinity Crisis when the interaction of plate tectonics and eustatic sea level fall led to the closure of the gateway between the Mediterranean and the Atlantic (see e.g., Netzeband et al., 2006; Cartwright and Jackson, 2008). In the Levant Basin, the evaporite sequence reaches a maximum thickness of about 2 km and shows a complex internal stratigraphy including folds and salt rollers. The presence of salt rollers complicates building of the velocity model. Particularly, picking of the residual-curvatures needed for the migration velocity analysis does not provide full-populated curvatures in the offset direction (deterioration of the signal due to migration stretch). In Figure 2.7, we provide a stacked section to illustrate the complexity of the recorded wavefield. This section was obtained by applying the n-CRS operator (Fomel and Kazinnik, 2013). We observe a lot of diffracted events, which occur along the top of salt indicating its fractured structure and masking the faults.

While the wavefront attributes are automatically extracted from prestack data for every time sample and central midpoint location, automatic event picking is a subtle procedure of crucial importance for tomography. Choosing the predetermined coherence value quite high reduces the number of events, particularly sub-salt events may not properly be presented in the input data for inversion, while the usage of lower values increases the risk to pick unreliable events with poorly determined wavefront attributes (Xie and Gajewski, 2019). Keeping this in mind and for comparison with previous results, we used the picks of Bauer et al. (2017). These authors utilized the picks for velocity model building with the conventional method.

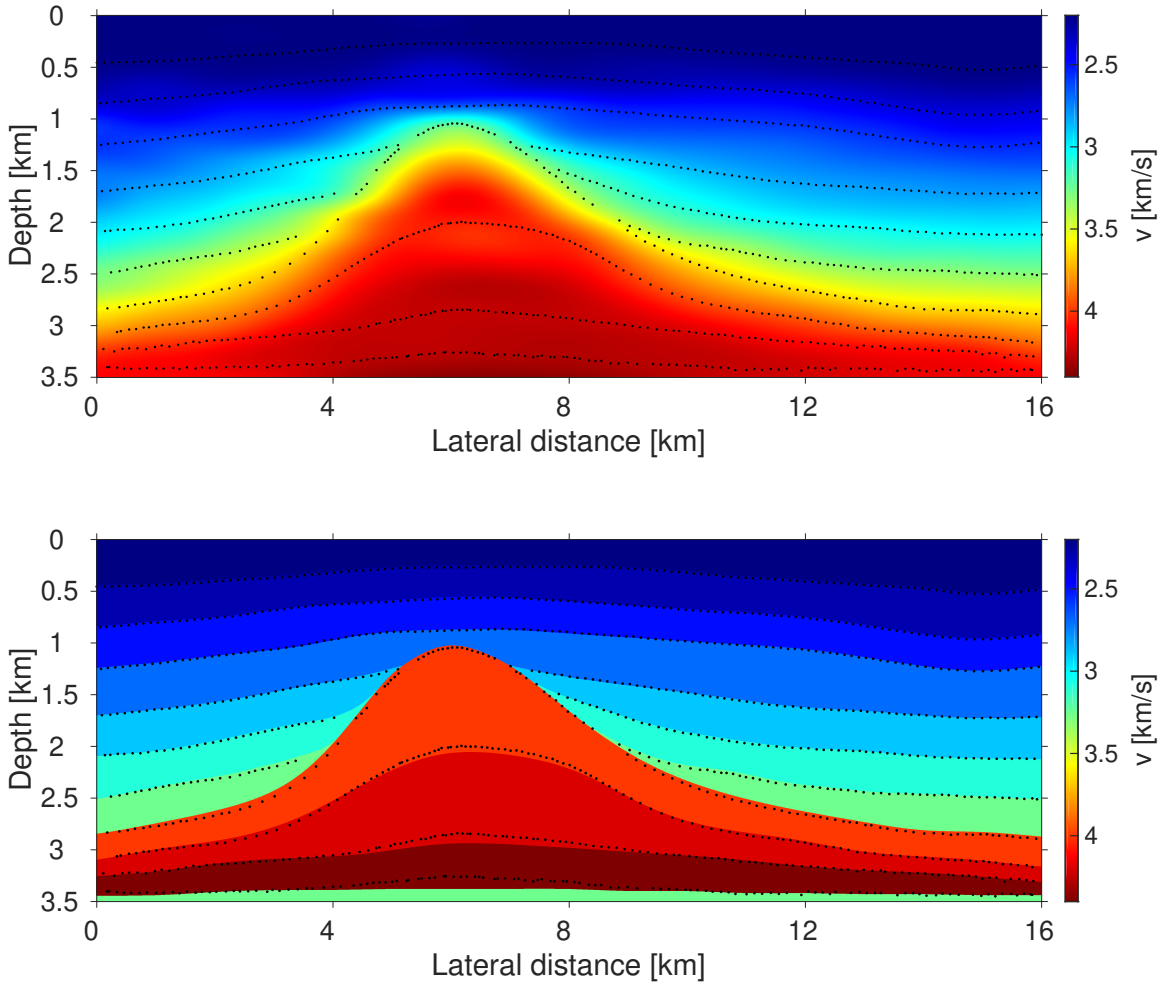

Figure 2.6: Tomographic (a) and synthetic (b) models with retrieved reflector elements (black dots).

2.4.2 Velocity model building

Based on published works on the geological setting in this part of the Levant Basin, we assume the lowest velocity in the sediments to be about 1.7 km/s and the highest velocity in the sediments under the salt to be about 3.6 km/s. This velocity information is used to create an initial velocity model with a constant gradient below the seabed (marked with a white line) as shown in Figure 2.8. The initial velocity linearly increases from 1.7 km/s at the seabed on the right side to 3.6 km/s at the lower boundary of the model. The constraints for the L-BFGS-B algorithm were the following: the node values above the seabed were fixed to the water velocity, lower and upper bounds for the node values below the seabed are determined by the a priori geological limits of 1.7 km/s for sediments and 4.3 km/s for the salt.

5525 diffraction picks in addition to 6430 reflection picks were considered by dynamic ray focusing using a 17×31 grid of 4-th order B-spline nodes with 900 m spacing in the

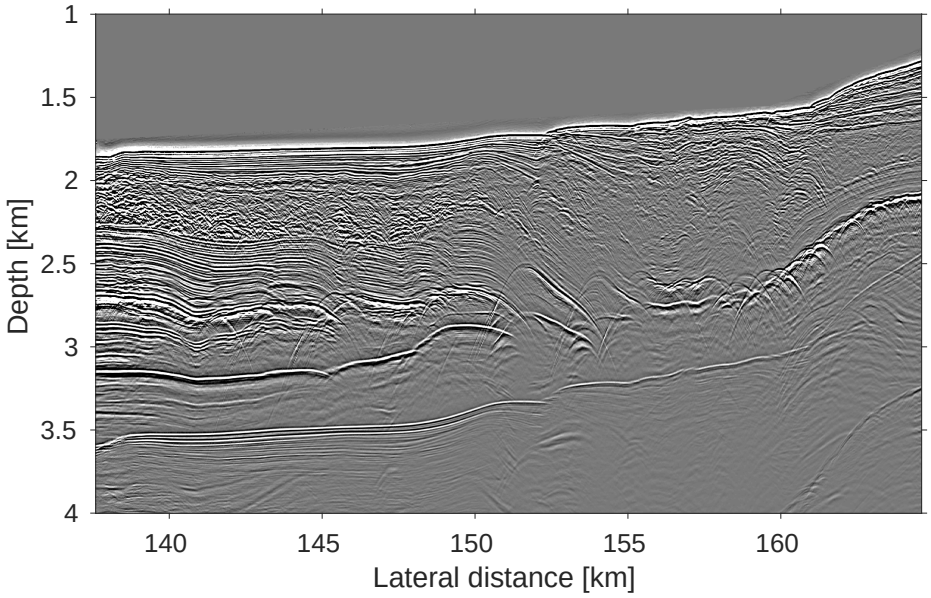

Figure 2.7: Common-reflection-surface stack of the marine field data.

horizontal direction and 218.75 m spacing in the vertical direction. This grid is marked with green dots in Figure 2.8. As in the synthetic example, we didn't use any regularization terms in the objective functional and its gradient. Again, this was possible due to the significant reduction of the inversion matrix (see matrices 2.10 and 2.11). The ratio between dimension of the data vector and dimension of the unknown vector in this example was approximately 22.7 against 1.3 of the conventional formulation. Figure 2.9 describes the convergence process, which was less smooth and slower than in the synthetic case (Figure 2.5). The result of the inversion is presented in Figure 2.10. The diffractors and normal-incidence-points were finally traced to their positions and superimposed on the retrieved tomographic model.

The high velocity evaporite unit of 1 km thickness is retrieved on the left side of the model. It is sandwiched between the reflector elements indicating the top and the bottom of the salt. The top of this body is in a good agreement with the previous studies by Bauer et al. (2017). Due to the significant velocity contrast between the sediments and the salt and also due to the complex stratigraphy it is usually a challenge to reconstruct a detailed velocity distribution by any type of tomography without using well logs. Moreover, there are very few reliable data picks beneath the salt, i.e., there is a poor illumination of the salt bottom by upgoing waves in a very complex region. This leads to velocity uncertainties, especially in the domain from 150 km to 160 km with complex salt roller structures. Nevertheless, we were able to retrieve two high velocity anomalies at 153 km and at 157 km, which clearly correspond to the salt rollers being in agreement with the depth migration image (Figure 2.11) and previous studies by Dümmong et al. (2008). From geological perspective, we know that these anomalies represent salt. Therefore, the velocity is underestimated in these highly heterogeneous regions. This occurs not only due to the lack of illumination but also due to the fact that characteristic size of the salt rollers is comparable to the node spacing (Figure 2.8). We observe an analogous phenomenon in the right part of the

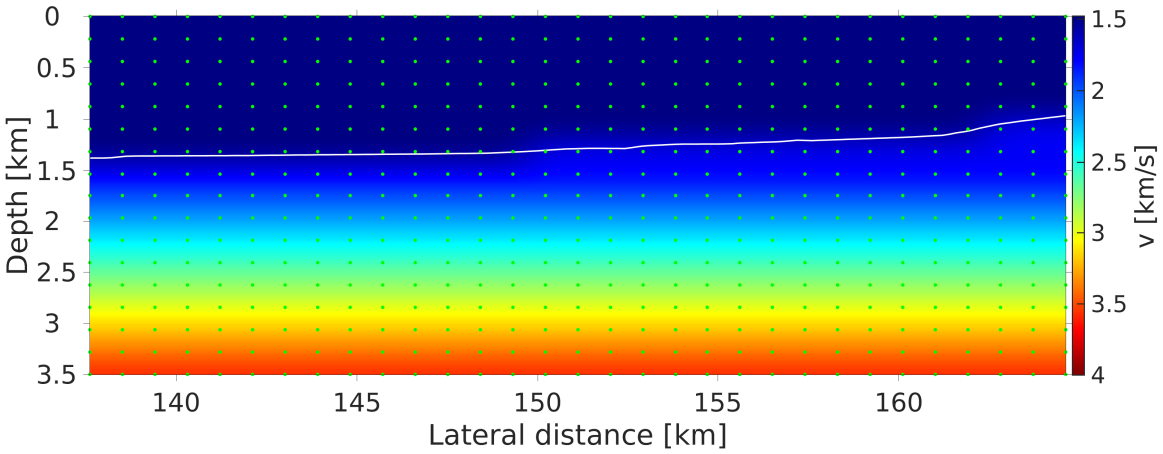

Figure 2.8: Initial model for the marine data inversion comprising a homogeneous water column and a constant gradient below the seabed (the seabed is marked with a white curve). A 17×31 4-th order B-spline node grid for the inversion (green dots) is used, with a spacing of 900 m in the horizontal and 218.75 m in the vertical direction.

section, where there is a barely visible stripe with slightly increased velocities. It goes up and right from the salt roller anomaly. It corresponds to a thin layer of strongly crushed salt comprising many diffractors (see Figure 2.7 and 2.11).

2.4.3 Depth imaging

Usually, tomographic velocity model building is followed by migration velocity analysis for refinement of the velocity model. Here we skip this process to judge the quality of the depth image from the dynamic ray focusing. Prestack reverse time migration produced the migrated section shown together with the corresponding velocity model in Figure 2.11. We observe a horst and graben along with step faulting. Disturbing shallow level strata caused by faulting can also be interpreted. Furthermore, it is validated by the presence of many diffractions in the shallow part of the seismic unmigrated section. Figure 2.12 shows a close up of the migrated section at the most complex part with salt rollers (green frame in Figure 2.11). In general, the top of salt is very well imaged. We can also claim that small thickness undulations of the evaporite unit between 156 and 158 km indeed represent faults and are not apparent velocity pull-ups/-downs. Since almost no picks below the evaporite were available, we could not justify if the base of salt is correctly imaged over the whole section. Moreover, at some places it replicates the top of salt, e.g., between 151 and 153 km.

2.5 Discussion

The presented method relies on wavefront attributes which are determined from operators which perform best if a short spread is considered. The tomography in combination with the method to determine its input, i.e., the wavefront attributes, is especially efficient for velocity model building with diffractions. The reason for this is the ray coverage. For

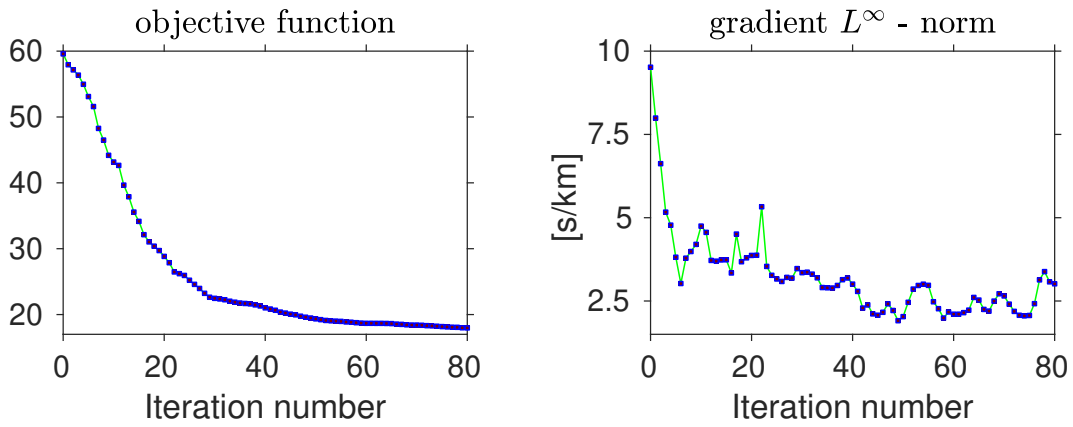

Figure 2.9: Descent of the objective functional (a) and its gradient maximum norm (b) during the dynamic ray focusing of the field data.

diffractions, illumination does not benefit from larger offsets in the case of a point diffraction and benefits less in the case of edge diffraction. Because of the decomposition principle of diffractions (Bauer et al., 2016) only zero-offset traces are sufficient to achieve the full ray coverage. Stability and reproducibility of the inversion, however, may be significantly improved by reformulating the problem for a fewer number of unknowns, as it was suggested in this work.

Another promising technology is simultaneous microseismic localization and velocity model building since the moveout of a passive seismic point source is equivalent to the moveout of a point diffractor at the location of the passive seismic source. A workflow of passive seismic data enhancement provides a set of wavefront attributes (Schwarz et al., 2016) similar to the reflection or diffraction case. Therefore, passive seismic wavefront tomography allows a simultaneous location and velocity model building with the additional challenge to determine the unknown source time (Diekmann et al., 2019). Close analogy between the passive event and the point diffraction allows adapting tools originally devised for diffractions.

Seismic anisotropy in the subsurface of the Earth is a well documented fact. If a near-surface model is available, we can extract the same input for the dynamic ray focusing from the wavefront attributes in the most general anisotropic case (Vanelle et al., 2018). Moreover, the objective functional derived in this paper, as well as the methodology to compute the gradient, can be used to conceive inversion for anisotropic models. However, kinematic and dynamic ray tracing will require an adjustment. Additionally, the perturbed matrix of dynamic ray tracing needs to be reformulated in terms of perturbations of the anisotropic parameters.

The reduction of unknowns in dynamic ray focusing was one of the major benefits of the proposed approach if compared to the conventional wavefront tomography. The considerably higher ratio of data picks to unknowns (22.7 against 1.3 for the field data example) allowed to perform the inversion without any regularization terms. An alternative approach to reduce the number of unknowns may also be addressed in a different way during

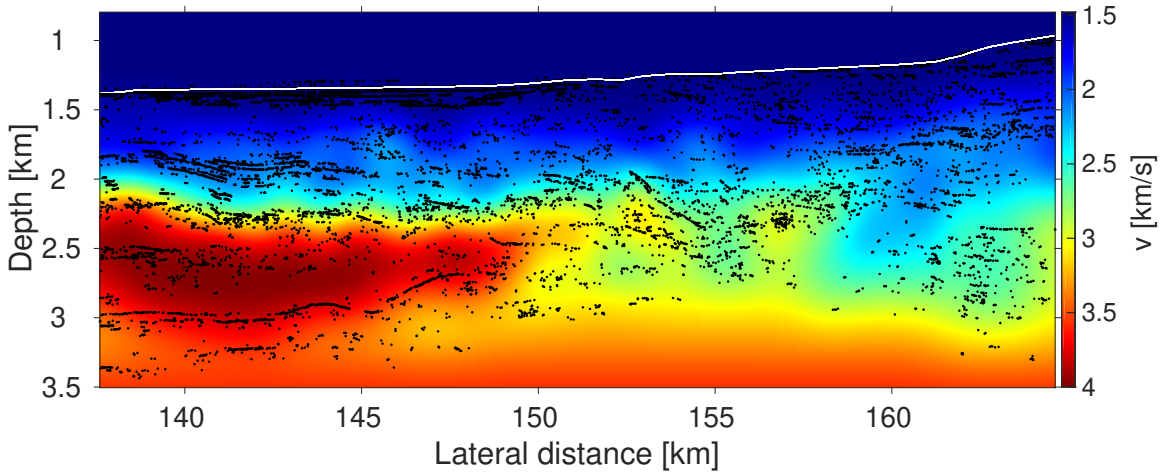

Figure 2.10: Retrieved tomographic model and localized reflector elements and diffractors (black dots) for the field data set from the Levant Basin.

forward-data fitting (Znak et al., 2017, 2018). An alternative functional formulated solely with respect to the velocity model comprises wavefront curvatures:

$$J[v] = \sum_{i=1}^{N_{data}} (M_i - M_i[x_i^d[v], z_i^d[v], \theta_i[v]; v])^2, \tag{2.22}$$

where x, t, and p_x inputs are fixed during optimization. Indeed, scattering coordinates and angles are determined with the velocity model by time-reversal ray tracing as soon as the values of x, t, and p_x are given. M turns out to be a composition of time-reversal kinematic ray tracing and upward dynamic ray tracing. A full Fréchet derivative of functional (2.22) can be obtained with the chain rule. We found this cumbersome and adhere to the one-way formulation in terms of focusing, but it may have differing features of the inverse problem.

For complex geologies, we need to use as much data as possible. Particularly, utilizing wavefront attributes of reflections from larger offsets might be essential for a detailed inversion. In this work, reformulation of the inverse problem with dynamic ray focusing was possible due to the unique property of the zero-offset ray. The ratio between the traveltimes of the incident and emergent branch is one in this case. In the finite-offset case, this ratio is usually not known as we extract only a sum over two branches from the data. Therefore, we can't match geometrical spreading at the ray endpoints in full analogy to the dynamic ray focusing. However, the approach of Sword (1986) or an approach using an eikonal solver may help. As demonstrated by Sambolian et al. (2019) with slope tomography, having source and receiver traveltime fields defined on a grid allows to find a velocity dependent reflecting element on the isochrone.

2.6 Conclusions

We developed a well-conditioned and stable approach for macro-velocity model building using wavefront attributes of zero-offset rays. It consists of time-reversal kinematic and dynamic ray tracing and minimizing geometrical spreading of normal-incidence-point-waves

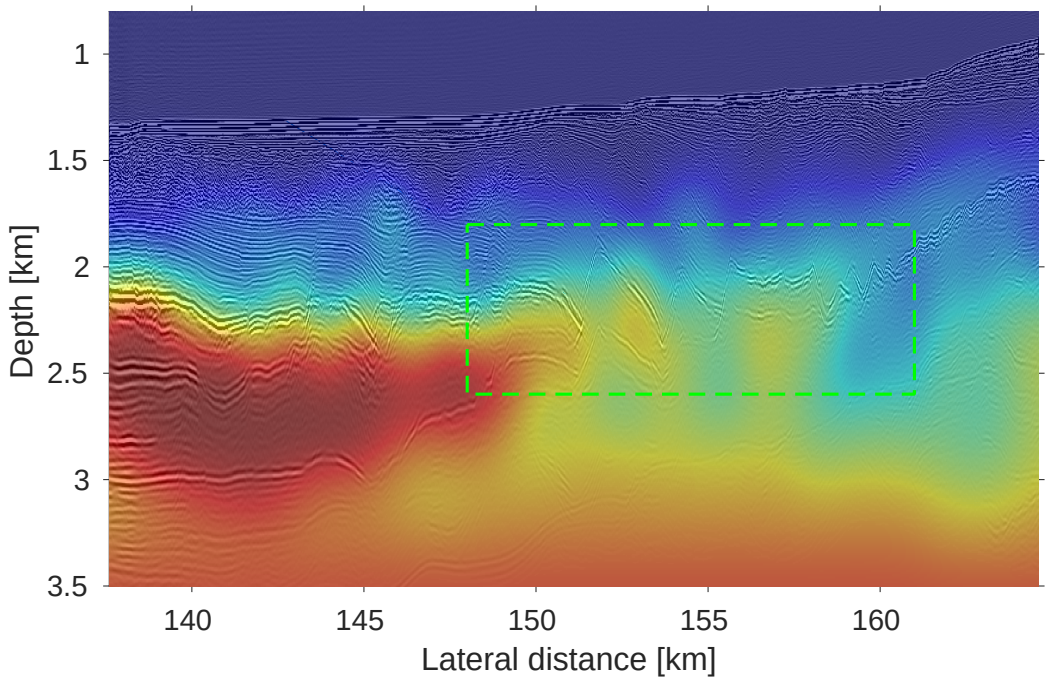

Figure 2.11: Depth migrated section superimposed on the retrieved tomographic model. The green frame highlights the most complex part with salt rollers (Figure 2.12).

and diffractions. We focus waves reversely in time simultaneously updating the scatterer positions and the velocity model. The input for the inversion are traveltime and wavefront attributes of zero-offset rays, i.e., horizontal slowness and wavefront curvature. They are retrieved from the data using multiparameter stacking techniques. These methods provide best results if applied with short spreads to achieve a local description of the wavefront without smearing lateral velocity changes.

If compared to the conventional wavefront tomography based on data fitting, the new objective functional contains a single physical quantity and depends only on the velocity model. This reformulation with its considerably smaller inversion matrix leads to favorable properties of the inverse problem such as relaxing regularization. Additionally, a reduced amount of tuning parameters in the objective functional allows to easier obtain reproducible results. This concerns, e.g., the weighting of different physical parameters since the proposed functional comprises only the focusing measure. We also provided the Fréchet derivatives and the adjoint-state formulas for computing the gradient.

We used the L-BFGS-B method as an optimization engine. The proposed tomographic inversion was first tested on the synthetic data comprising a salt body. The retrieved tomographic image highly correlates with the synthetic model, the end-points of normal-incidence-rays propagated into the final model constitute the layer boundaries. We further applied our approach to complex marine data. The inverted model was used in a common-shot depth migration. In the migrated section, we observed a clean and continuous image of top of salt and well focused steep faults. The tomographic results were also consistent with previous studies. In both synthetic and field data examples, we did not use any regularization terms, which confirmed the well-conditioned behavior of the new formulation.

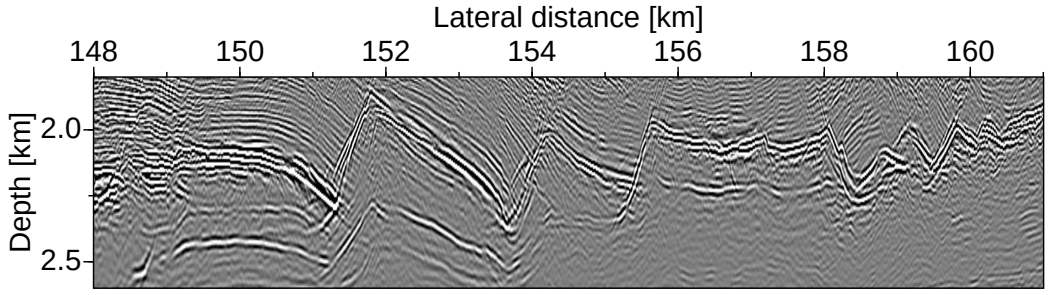

Figure 2.12: Depth migrated section: close up at the most complex part with salt rollers (Figure 2.11).

Acknowledgements

This work was partly supported by the Wave Inversion Technology (WIT) Consortium and by the Federal Ministry for Economic Affairs and Energy of Germany (project number 03SX427B). We are thankful to TGS for providing the field data. We appreciate the assistance of Alex Bauer and Jan Walda in preparing the field data picks. We also thank the Applied Seismic Group, University of Hamburg, for continuous discussions. The synthetic data were modeled by Seismic Unix.

3 Ray perturbation theory in wavefront-orthonormal coordinates: generally anisotropic 3D elastic solids

Abstract

We focus on the first-order ray perturbation theory formulated in the wavefront-orthonormal coordinates for 3D generally anisotropic inhomogeneous elastic media. We consider two possible options – perturbation by the ray tracing initial conditions and perturbation by the anisotropic model. We use a technique that doesn't require expansion of the ray-centered Hamiltonian. It is based on projecting the differential equations formulated in Cartesian coordinates to the wavefront-orthonormal basis and on relating the projections to the wavefront-orthonormal coordinates. Thus, we consider two ways for describing the perturbations – using wavefront-orthonormal projections of the equal-time perturbations and using perturbations in the wavefront-orthonormal coordinates. For both points of view, we derive first-order linear systems of differential equations with dimensionality reduced in comparison to the Cartesian formulation. 4×4 wave propagator formalism can be utilized instead of the 6×6 one. The systems formulated using the wavefront-orthonormal coordinates exhibit a simplified formulation, compared to the systems for the wavefront-orthonormal projections, due to contraction of the source term. We test the equations solving them numerically in an inhomogeneous VTI model.

3.1 Introduction

Seismic inversion, which in most cases represents a process of local optimization in a functional space, is based on one or another perturbation theory since they commonly provide a way of computing the Fréchet derivatives (e. g., Tarantola, 1987; Plessix, 2006). Depending on the order, the Fréchet derivative operator allows for computing gradient or Hessian of the discretized objective function with respect to the unknown model parameters.

Perturbation theory plays important role in seismic modelling significantly extending scope of the analytical methods. It helps to develop the numerical modelling methods as well by formulating them for complex environments as perturbations of well established methods in corresponding relatively simple media (e. g., Nowack and Pšenčík, 1991; Mensch and Farra, 1999; Soukina et al., 2003; Waheed et al., 2015).

The first systematic study of the ray method for inhomogeneous generally anisotropic lossless elastic solids was carried out by Babich (1961, 1994). The Hamiltonian system of first-order differential equations for the characteristics of the anisotropic eikonal equation, we refer to it as the kinematic ray tracing system, found a huge number of applications in exploration and global seismology.

Červený (1972) derived the 6×6 system of first-order linear differential equations for the dynamic ray tracing in Cartesian coordinates. This system allowed for effective computing of the geometical spreading, which determines the wave amplitude and the phase shift. Therefore, it lead to seismic modelling in generally anisotropic 3D elastic media (Gajewski and Pšenčik, 1990).

The dynamic ray tracing in ray-centered coordinates was suggested by Popov and Pšenčík (1978) for isotropic media. It allows computing of the geometrical spreading with a reduced number of equations (4×4 wave propagator formalism instead of the 6×6 one in 3D). The first extension of this idea to the anisotropic case in non-orthogonal ray-centered coordinates was given by Hanyga (1982). An alternative formulation that naturally uses a local non-degenerate orthogonal coordinate system related to the wavefront (wavefront-orthonormal coordinates) was developed by Kashtan and Petrashen (1983) and by Bakker (1996). They introduced the natural wavefront-orthonormal basis (Petrashen and Kashtan, 1984), which has to be computed in 3D with an additional 3×3 system of linear first-order differential equations. A comprehensive review and comparison of different ray-centered coordinate systems for the dynamic ray tracing is given in the paper by Červený (2007). The author draws a conclusion that the corresponding systems of differential equations are equivalent, but formulation of the dynamic ray tracing in the wavefront-orthonormal coordinates is slightly simpler. The wavefront-orthonormal coordinates do not require distinguishing between the covariant and contravariant basis vectors and computing the dual basis.

The 6×6 Cartesian and 4×4 wavefront-orthonormal approaches to the dynamic ray tracing are equivalent alternatives. The 6×6 Cartesian formulation doesn't require additional basis computing, while 4×4 formulation has a reduced number of equations and directly expresses the wavefront curvature matrix (Červený, 2001). The corresponding propagators are related and can be transformed into each other using the wavefront-orthonormal basis at the initial and end points of the ray (Červený, 2007; Cervenỳ and Jan Moser, 2007).

Farra and Madariaga (1987) applied the perturbation theory methods to the kinematic ray tracing in isotropic media. Similarly to the paraxial ray tracing of Popov and Pšenčík (1978), they employed expansion of the Hamiltonian formulated in the ray-centered coordinates and derived the reduced 4×4 inhomogeneous system for the case of perturbation by the velocity model.

Previous work on the anisotropic ray perturbation theory, to our knowledge, has focused on the global Cartesian 6×6 formulation. The first-order perturbation of the kinematic ray tracing in anisotropic media was formulated by Jech and Pšenčík (1989) and by Farra (1989). It is significantly simplified in the case of weak anisotropy since the necessary polarization vector derivatives can be explicitly formulated in this case (Pšenčík and Farra, 2005).

In this work, we fill the gap and derive an anisotropic analogue of equations by Farra and Madariaga (1987). We formulate the ray perturbation theory in the wavefront-orthonormal coordinates for generally anisotropic 3D elastic solids. We study both, perturbation by the ray tracing initial conditions and by the anisotropic model. Instead of expanding the wavefront-tangent ray-centered Hamiltonian, which was utilized in the original paper by Farra and Madariaga (1987), we use a technique based on projecting the equal-time perturbations to the wavefront-orthonormal basis and further relating these projections to the wavefront-orthonormal coordinates. The paper reveals a difference between two ways of describing the perturbations – the equal-time perturbation projection and perturbation in the

wavefront-orthonormal coordinates. The latter point of view simplifies the resulting differential equations. We explicitly express the differential equations in terms of the secondary Christoffel equation eigenvalues and eigenvectors. No S-wave degeneration is addressed.

The paper is divided into four technical sections. The first one recalls the kinematic and dynamic ray tracing. Next two sections correspond to different possible origins of the ray perturbation – initial conditions and elastic moduli. In these sections, the global Cartesian approach is given first. Then, it is followed by the formulation for the equal-time perturbation projections, which is reduced further to the formulation in wavefront-orthonormal coordinates. The last section illustrates the proposed method numerically in an inhomogeneous VTI model.

In the first appendix, we give formulas for the polarization derivatives with respect to Cartesian coordinates, slowness vector components, and elastic moduli, expressed through the secondary Christoffel equation eigenvalues and eigenvectors. In the second appendix, we derive initial conditions for the wavefront-orthonormal coordinates in the case when the initial ray point and two slowness vector components are fixed, which is motivated by our practice of seismic inversion.

3.2 Kinematic and dynamic ray tracing in anisotropic media

3.2.1 Kinematic ray tracing

In a 3D generally anisotropic inhomogeneous medium with smooth density $\rho(\mathbf{x})$ and smooth elastic moduli $c_{ijkl}(\mathbf{x})$, a ray $\mathbf{x} = \mathbf{x}(t)$ and the corresponding slowness vector $\mathbf{p} = \mathbf{p}(t)$ satisfy the kinematic ray tracing system (Červený, 2001; Babich and Kiselev, 2018):

$$\frac{dx_i}{dt} = a_{ijkl} g_j g_k p_l, \tag{3.1}$$

$$\frac{dp_i}{dt} = -\frac{1}{2}\frac{\partial a_{jklm}}{\partial x_i} g_k g_l p_j p_m, \qquad i = 1, 2, 3, \tag{3.2}$$

where the tensor components $a_{ijkl}(\mathbf{x}) = \frac{c_{ijkl}(\mathbf{x})}{\rho(\mathbf{x})}$ are the density normalized elastic moduli. The Einstein's rule for summation over repeated indices is used throughout the paper. For a given space point $\mathbf{x}$ and wavefront normal $\mathbf{n} = \frac{\mathbf{p}}{|\mathbf{p}|}$, components of the normalized polarization vector $g_i(\mathbf{x}, \mathbf{n})$ follows from the Christoffel eigenvalues and eigenvectors problem

$$a_{ijkl} n_j n_k g_l = v^2 g_i, \qquad i = 1, 2, 3, \tag{3.3}$$

where the squared phase velocity eigenvalue v^2 is selected in accordance to the wave mode under consideration, the qP-wave or one of the two qS-waves. Phase velocity depends on the space coordinates and the components of the wavefront normal: $v(\mathbf{x}, \mathbf{n}) = \sqrt{a_{ijkl} g_j g_k n_i n_l}$.

The right-hand side of the first three equations (3.1) represents components $u_i = \frac{\partial v}{\partial n_i} = a_{ijkl} g_j g_k p_l$ of the ray velocity vector $\mathbf{u}$, which is related to the energy flux. The right-hand side of the last three equations (3.2) may be rewritten in a way to formally coincide with the corresponding right-hand side in the isotropic case:

$$\frac{dp_i}{dt} = -\frac{1}{v}\frac{\partial v}{\partial x_i}, \qquad i = 1, 2, 3. \tag{3.4}$$

The kinematic ray tracing system (eqs 3.1-3.2) represents first-order ordinary differential equations for characteristics of the nonlinear first-order partial differential equation

$$a_{ijkl} g_j g_k p_i p_l = 1, \tag{3.5}$$

called the eikonal equation.

3.2.2 Dynamic ray tracing in Cartesian and wavefront-orthonormal coordinates

Introducing two complimentary to time ray coordinates γ_1 and γ_2, e. g., as initial spherical angles of the wavefront normal, leads to spanning the space with the ray fan and to the transformations from the ray coordinates to the Cartesian coordinates and to the slowness vector components:

$$x_i = x_i(\gamma_1, \gamma_2, t), \quad p_i = p_i(\gamma_1, \gamma_2, t), \quad i = 1, 2, 3. \tag{3.6}$$

Dynamic ray tracing in global Cartesian coordinates is formulated, then, by differentiating the kinematic ray tracing system (3.1-3.2) with respect to the auxiliary ray coordinates:

$$\frac{d}{dt}\begin{pmatrix} \frac{\partial \mathbf{x}}{\partial \gamma_\alpha} \\ \frac{\partial \mathbf{p}}{\partial \gamma_\alpha} \end{pmatrix} = S^{(6)} \begin{pmatrix} \frac{\partial \mathbf{x}}{\partial \gamma_\alpha} \\ \frac{\partial \mathbf{p}}{\partial \gamma_\alpha} \end{pmatrix}, \qquad S^{(6)} = \begin{pmatrix} \hat{\Phi} + \hat{W} B \hat{V}^T & \hat{\Psi} \;\; + \hat{W} B \hat{W}^T \\ -\hat{Y} - \hat{V} B \hat{V}^T & -\hat{\Phi}^T - \hat{V} B \hat{W}^T \end{pmatrix}, \qquad \alpha = 1, 2. \tag{3.7}$$

We introduce here 3×3 matrices to explicitly formulate the dynamic ray tracing using the secondary to $\mathbf{g}$ eigenvectors $\mathbf{g}^{(1)}$, $\mathbf{g}^{(2)}$ and the corresponding secondary eigenvalues $v^{(1)}$, $v^{(2)}$:

$$\hat{\Phi}_{ij} = \frac{\partial a_{iklm}}{\partial x_j} g_k g_l p_m, \qquad \hat{\Psi}_{ij} = \hat{\Psi}_{ji} = a_{iklj} g_k g_l, \qquad \hat{Y}_{ij} = \hat{Y}_{ji} = \frac{1}{2} \frac{\partial^2 a_{klmn}}{\partial x_i \partial x_j} g_l g_m p_k p_n,$$

$$\hat{W}_{ij} = (a_{ijkl} + a_{ikjl}) g_k p_l, \qquad \hat{V}_{ij} = \frac{\partial a_{jklm}}{\partial x_i} p_k p_l g_m, \qquad B_{ij} = B_{ji} = v^2 \sum_{\alpha=1}^{2} \frac{g_i^{(\alpha)} g_j^{(\alpha)}}{v^2 - (v^{(\alpha)})^2},$$
$$i, j = 1, 2, 3. \tag{3.8}$$

This is done by evaluating derivatives of the polarization vector with respect to the Cartesian coordinates and to the slowness vector components (see Appendix D.1):

$$\frac{\partial g_i}{\partial x_j} = \left(B \hat{V}^T\right)_{ij}, \qquad \frac{\partial g_i}{\partial p_j} = \left(B \hat{W}^T\right)_{ij}, \qquad i, j = 1, 2, 3. \tag{3.9}$$

Throughout the paper, we assume no S-wave degeneration, which means all the eigenvalues are isolated. For both sets of derivatives, for $\frac{\partial \mathbf{x}}{\partial \gamma_1}, \frac{\partial \mathbf{p}}{\partial \gamma_1}$ and for $\frac{\partial \mathbf{x}}{\partial \gamma_2}, \frac{\partial \mathbf{p}}{\partial \gamma_2}$, the same system (3.7) holds. It is linear in contrast to the kinematic ray tracing system (3.1-3.2) and can be solved with the 6×6 propagator formalism (e. g., Červený, 2001).

The wavefront-orthonormal coordinates q_1, q_2, n are defined in a local Cartesian system spanned by the wavefront-orthonormal basis. The wavefront-orthonormal basis $\mathbf{e}_1, \mathbf{e}_2, \mathbf{e}_n$ comprises the normal to the wavefront, $\mathbf{e}_n = \mathbf{n} = v\mathbf{p}$, and two mutually orthogonal, tangent

to the wavefront, unit vectors defined with the following differential equations (Kashtan and Petrashen, 1983; Bakker, 1996):

$$\frac{d\mathbf{e}_\alpha}{dt} = (\nabla_{\mathbf{x}} v, \mathbf{e}_\alpha)\mathbf{e}_n = v_\alpha \mathbf{e}_n, \qquad \alpha = 1, 2. \tag{3.10}$$

Cartesian components of the basis vectors will be denoted correspondingly with to indices, e. g., $(\mathbf{e}_1)_1 = e_{11}$. We use subscript notations for the fixed normal derivatives of the phase velocity and of the normalized moduli with respect to the wavefront-orthonormal coordinates:

$$v_\alpha = \frac{\partial v}{\partial q_\alpha} = (\nabla_{\mathbf{x}} v, \mathbf{e}_\alpha) = \frac{1}{2} v a_{\alpha,ijkl} g_j g_k p_i p_l, \qquad \alpha = 1, 2, \tag{3.11}$$

$$v_n = \frac{\partial v}{\partial n} = (\nabla_{\mathbf{x}} v, \mathbf{e}_n) = \frac{1}{2} v a_{n,ijkl} g_j g_k p_i p_l, \tag{3.12}$$

$$a_{\alpha,ijkl} = \frac{\partial a_{ijkl}}{\partial q_\alpha} = (\nabla_{\mathbf{x}} a_{ijkl}, \mathbf{e}_\alpha), \qquad \alpha = 1, 2, \tag{3.13}$$

$$a_{n,ijkl} = \frac{\partial a_{ijkl}}{\partial n} = (\nabla_{\mathbf{x}} a_{ijkl}, \mathbf{e}_n), \qquad i, j, k, l = 1, 2, 3. \tag{3.14}$$

For the time derivative of the entire basis, an antisymmetric relation exists:

$$\frac{d}{dt}\begin{pmatrix}\mathbf{e}_1\\ \mathbf{e}_2\\ \mathbf{e}_n\end{pmatrix} = \begin{pmatrix}0 & 0 & v_1\\ 0 & 0 & v_2\\ -v_1 & -v_2 & 0\end{pmatrix}\begin{pmatrix}\mathbf{e}_1\\ \mathbf{e}_2\\ \mathbf{e}_n\end{pmatrix}. \tag{3.15}$$

There is no need to trace the normal basis vector. It is determined during the ray tracing. The expression for its time derivative, however, is necessary for understanding the following sections.

Introducing 2×2 matrices of the dynamic quantity projections onto the wavefront-orthonormal basis,

$$Q_{\alpha\beta} = \left(\mathbf{e}_\alpha, \frac{\partial \mathbf{x}}{\partial \gamma_\beta}\right), \qquad P_{\alpha\beta} = \left(\mathbf{e}_\alpha, \frac{\partial \mathbf{p}}{\partial \gamma_\beta}\right), \qquad \alpha, \beta = 1, 2, \tag{3.16}$$

allows for a reduced dimension formulation of the dynamic ray tracing with the 4×4 propagator formalism (e. g., Červený, 2001):

$$\frac{d}{dt}\begin{pmatrix}Q\\ P\end{pmatrix} = S^{(4)}\begin{pmatrix}Q\\ P\end{pmatrix}. \tag{3.17}$$

2×2 blocks of the 4×4 dynamic ray tracing matrix $S^{(4)}$

$$\left(S_{11}^{(4)}\right)_{\alpha\beta} = \Phi_{\alpha\beta} + W_{\alpha i} B_{ij} V_{j\beta}^T - \frac{u_\alpha^q v_\beta}{v}, \quad \left(S_{12}^{(4)}\right)_{\alpha\beta} = \Psi_{\alpha\beta} + W_{\alpha i} B_{ij} W_{j\beta}^T - u_\alpha^q u_\beta^q,$$

$$\left(S_{21}^{(4)}\right)_{\alpha\beta} = -Y_{\alpha\beta} - V_{\alpha i} B_{ij} V_{j\beta}^T + \frac{v_\alpha v_\beta}{v^2}, \quad \left(S_{22}^{(4)}\right)_{\alpha\beta} = -\Phi_{\alpha\beta}^T - V_{\alpha i} B_{ij} W_{j\beta}^T + \frac{v_\alpha u_\beta^q}{v},$$

$$\alpha, \beta = 1, 2, \tag{3.18}$$

comprise the reduced matrices

$$\begin{aligned}
\Phi_{\alpha\beta} &= (\mathbf{e}_\alpha, \hat{\Phi}\mathbf{e}_\beta) = a_{\beta,ijkl} g_j g_k e_{\alpha i} p_l, \\
\Psi_{\alpha\beta} &= \Psi_{\beta\alpha} = (\mathbf{e}_\alpha, \hat{\Psi}\mathbf{e}_\beta) = a_{ijkl} g_j g_k e_{\alpha i} e_{\beta l}, \\
Y_{\alpha\beta} &= Y_{\beta\alpha} = (\mathbf{e}_\alpha, \hat{Y}\mathbf{e}_\beta) = \frac{1}{2}\frac{\partial^2 a_{ijkl}}{\partial x_m \partial x_n} g_j g_k p_i p_l e_{\alpha m} e_{\beta n}, \qquad \alpha, \beta = 1, 2, \\
W_{\alpha i} &= (\mathbf{e}_\alpha)_j \hat{W}_{ji} = (a_{jikl} + a_{jkil}) g_k p_l e_{\alpha j}, \\
V_{\alpha i} &= (\mathbf{e}_\alpha)_j \hat{V}_{ji} = a_{\alpha,ijkl} p_j p_k g_l, \qquad \alpha = 1, 2, \qquad i = 1, 2, 3,
\end{aligned} \tag{3.19}$$

and the projected ray velocity vector $u^q_\alpha = (\mathbf{u}, \mathbf{e}_\alpha)$, $\alpha = 1, 2$. Eq. (3.17) is derived by differentiating projections (3.16), substituting eqs. (3.7), and accounting for the time derivatives of the basis vectors (3.10). Additionally, an expression for the remaining projection of the slowness vector derivative is used:

$$\left(\mathbf{e}_n, \frac{\partial \mathbf{p}}{\partial \gamma_\alpha}\right) = -\frac{v_\beta}{v^2} Q_{\beta\alpha} - \frac{u^q_\beta}{v} P_{\beta\alpha}, \qquad \alpha = 1, 2. \tag{3.20}$$

In the isotropic limit, the last term in this expression becomes zero due to vanishing of the wavefront-orthonormal projections of the ray velocity vector. The projection (3.20) is fully determined with the matrix Q in this case.

Dynamic ray tracing, i. e., solving equations (3.7) or (3.17), allows computing the Jacobian of the mapping from the ray coordinates to the Cartesian coordinates, $J = \frac{\partial(x_1, x_2, x_3)}{\partial(\gamma_1, \gamma_2, t)} = \left(\frac{\partial \mathbf{x}}{\partial t}, \left[\frac{\partial \mathbf{x}}{\partial \gamma_1}, \frac{\partial \mathbf{x}}{\partial \gamma_2}\right]\right) = v \det Q$, and, therefore, amplitude and phase shift of the zero-order ray series approximation by the factor of $\frac{1}{\sqrt{\rho J}}$.

3.3 Perturbation by the initial conditions

In this section, the anisotropic model is kept fixed. Perturbations of the kinematic quantities are caused by a variation in the initial conditions for the ray tracing.

3.3.1 Global Cartesian coordinates

We consider equal-time kinematic perturbations $\triangle\mathbf{x}(t) = \mathbf{x}^{(1)}(t) - \mathbf{x}^{(0)}(t)$ and $\triangle\mathbf{p}(t) = \mathbf{p}^{(1)}(t) - \mathbf{p}^{(0)}(t)$. Equal-time perturbation implies a difference computed for the same time along the reference and along the perturbed ray. In order to distinguish with perturbations of the dynamic ray tracing quantities from eq. (3.7) or (3.17), we use the term "kinematic perturbations" for the perturbations of ray and slowness vector. A perturbed ray, $\mathbf{x}^{(1)}(t)$, and the slowness vector, $\mathbf{p}^{(1)}(t)$, are fully determined by conditions at the initial time t_0:

$$\mathbf{x}^{(1)}(t_0) = \mathbf{x}^{(0)}(t_0) + \triangle\mathbf{x}(t_0), \qquad \mathbf{p}^{(1)}(t_0) = \mathbf{p}^{(0)}(t_0) + \triangle\mathbf{p}(t_0). \tag{3.21}$$

We assume stability, when small initial perturbations $\triangle\mathbf{x}(t_0)$ and $\triangle\mathbf{p}(t_0)$ cause small perturbations $\triangle\mathbf{x}(t)$ and $\triangle\mathbf{p}(t)$ for $t \neq t_0$. If it is clear from the context and we don't aim to emphasize the distinction, we will omit the superscripts $^{(0)}$ denoting the unperturbed quantities. Perturbation of the initial ray point is related to perturbation of the initial slowness

vector. Moreover, a relation exists for the kinematic perturbations, $\triangle\mathbf{x}(t)$ and $\triangle\mathbf{p}(t)$, at any traveltime (Farra, 1989):

$$(\mathbf{u}, \triangle\mathbf{p}) = \left(-\frac{\nabla_{\mathbf{x}} v}{v}, \triangle\mathbf{x}\right). \tag{3.22}$$

This is a consequence of the first-order perturbation of the eikonal equation (3.5).

The first-order expansion of the ray tracing system (3.1-3.2) considered for the perturbed ray yields a homogeneous linear system with respect to the ray and slowness vector perturbations:

$$\frac{d}{dt}\begin{pmatrix}\triangle\mathbf{x}\\ \triangle\mathbf{p}\end{pmatrix} = S^{(6)}\begin{pmatrix}\triangle\mathbf{x}\\ \triangle\mathbf{p}\end{pmatrix} \tag{3.23}$$

It comprises the dynamic ray tracing matrix in Cartesian coordinates, $S^{(6)}$ (see eq. 3.7).

3.3.2 Projections of the equal-time perturbations

Due to eq. (3.22), five scalars $\triangle x_1^q, \triangle x_2^q, \triangle p_1^q, \triangle p_2^q$, and $\triangle n$ are sufficient for describing the kinematic perturbations. In fact, we will derive a system with respect to the four independent quantities $\triangle x_1^q, \triangle x_2^q, \triangle p_1^q, \triangle p_2^q$ only. In the case of perturbation by the anisotropic model, the fifth one, $\triangle n$, will be formulated separately with a simple integration. We introduce them as projections of the equal-time kinematic perturbations to the unperturbed wavefront-orthonormal basis:

$$\triangle\mathbf{x} = \triangle x_\alpha^q\, \mathbf{e}_\alpha + \triangle n\, \mathbf{e}_n, \tag{3.24}$$

$$\triangle\mathbf{p} = \triangle p_\alpha^q\, \mathbf{e}_\alpha - \frac{1}{v^2}(v_\alpha \triangle x_\alpha^q + v\, u_\alpha^q \triangle p_\alpha^q + v_n \triangle n)\, \mathbf{e}_n. \tag{3.25}$$

The projection $(\triangle\mathbf{p}, \mathbf{e}_n)$ depends on the other projections, similarly to the dynamic ray tracing projection (3.20). It also comprises a $\triangle p$-term, which vanishes in the isotropic case.

Differential equations for $\triangle x_1^q, \triangle x_2^q, \triangle p_1^q, \triangle p_2^q$, and $\triangle n$ follow from eqs. (3.23), representations (3.24, 3.25), and expressions for the time derivatives of the basis vectors (3.15). Namely, five equations for the projections are

$$\begin{aligned}
\frac{d}{dt}\triangle x_\alpha^q &= \left(S_{11}^{(4)}\right)_{\alpha\beta} \triangle x_\beta^q + \left(S_{12}^{(4)}\right)_{\alpha\beta} \triangle p_\beta^q + \triangle n \left(\left(\hat{\Phi} + \hat{W} B \hat{V}^T\right)_{ij} e_{\alpha i} e_{nj} - \frac{v_n}{v} u_\alpha^q + v_\alpha\right),\\
\frac{d}{dt}\triangle p_\alpha^q &= \left(S_{21}^{(4)}\right)_{\alpha\beta} \triangle x_\beta^q + \left(S_{22}^{(4)}\right)_{\alpha\beta} \triangle p_\beta^q + \triangle n \left(\left(\hat{Y} + \hat{V} B \hat{V}^T\right)_{ij} e_{\alpha i} e_{nj} + \frac{v_n}{v} v_\alpha\right),\ \alpha = 1, 2,\\
\frac{d}{dt}\triangle n &= v_n \triangle n.
\end{aligned} \tag{3.26}$$

The last equation is homogeneous and independent. Differentiating $v^2 = (p_i p_i)^{-1}$ shows that $\frac{dv}{dt} = v v_n$. Therefore, $\triangle n(t) = \frac{\triangle n(t_0)}{v(t_0)} v(t)$ satisfies the independent equation, and the initial condition as well. Note in the first order, a time lag

$$\triangle t = \frac{\triangle n(t)}{v(t)} = \frac{\triangle n(t_0)}{v(t_0)} \tag{3.27}$$

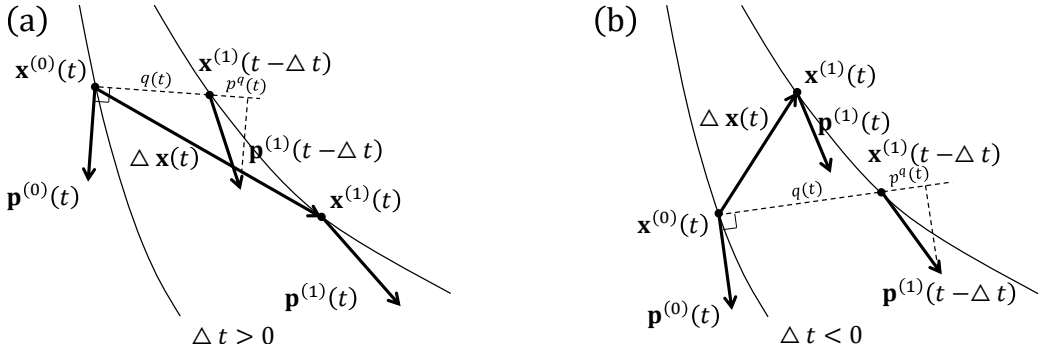

Figure 3.1: The wavefront-orthonormal ray-centered perturbations q, p^q and the equal-time perturbation $\triangle\mathbf{x}$ (2D illustration). The point on the perturbed ray, $\mathbf{x}^{(1)}(t)$, outruns the ray point defined with the ray-centered approach, $\mathbf{x}^{(1)}(t-\triangle t)$, when $\triangle t > 0$ (a), and vice versa when $\triangle t < 0$ (b).

stays constant for the perturbation by the initial conditions. Meaning of this time lag will be explained in the next subsection. Placing this solution $\triangle n(t)$ to the source term of system (3.26) closes it with respect to the projections $\triangle x_1^q, \triangle x_2^q$ and $\triangle p_1^q, \triangle p_2^q$:

$$\begin{aligned}
\frac{d}{dt}\triangle x_\alpha^q &= \left(S_{11}^{(4)}\right)_{\alpha\beta}\triangle x_\beta^q + \left(S_{12}^{(4)}\right)_{\alpha\beta}\triangle p_\beta^q + \triangle t\left(v\left(\hat{\Phi}+\hat{W}B\hat{V}^T\right)_{ij}e_{\alpha i}e_{nj} - v_n u_\alpha^q + v v_\alpha\right),\\
\frac{d}{dt}\triangle p_\alpha^q &= \left(S_{21}^{(4)}\right)_{\alpha\beta}\triangle x_\beta^q + \left(S_{22}^{(4)}\right)_{\alpha\beta}\triangle p_\beta^q + \triangle t\left(v\left(\hat{Y}+\hat{V}B\hat{V}^T\right)_{ij}e_{\alpha i}e_{nj} + v_n v_\alpha\right),\ \alpha = 1,2.
\end{aligned} \tag{3.28}$$

The projections of equal-time kinematic perturbations satisfy the inhomogeneous dynamic ray tracing system in wavefront-orthonormal coordinates.

3.3.3 Perturbations in wavefront-orthonormal coordinates

Up to now, we have considered the kinematic perturbations $\triangle\mathbf{x}(t)$ and $\triangle\mathbf{p}(t)$ describing them as projections $\triangle x_1^q(t), \triangle x_2^q(t)$ and $\triangle p_1^q(t), \triangle p_2^q(t)$ onto the unperturbed wavefront-orthonormal basis. By doing this, we imply that the perturbed ray and slowness vector, $\mathbf{x}^{(1)}(t)$ and $\mathbf{p}^{(1)}(t)$, correspond to the same traveltime t computed along the perturbed ray as for the reference one. Thus, we have considered the equal-time perturbations and their projections. However, another point of view exists. Originally introduced by Babich and Buldyrev (1972), the concept of ray-centered coordinates was used in isotropic media by Popov and Pšenčík (1978) for the paraxial and dynamic ray tracing. Further, it was applied by Farra and Madariaga (1987) for the ray perturbation by velocity model. In the isotropic case, the ray-centered coordinates are naturally defined in a plane orthogonal to the reference ray. In the case of anisotropy, however, there is a freedom in choosing such coordinates since orthogonality to a ray doesn't mean tangency to the wavefront. For a detailed discussion on various ray-centered coordinate systems, we refer a reader to the paper by Klimeš (2006).

Wavefront-orthonormal coordinates are ray-centered coordinates in wavefront-tangent plane centered at the reference ray and describing the perturbed ray (see Fig. 3.1). In

accordance to the wavefront-orthonormal basis on the reference ray, at any time t measured along this reference ray, two local coordinates of the perturbed ray $q_1(t), q_2(t)$ exist in the plane tangent to the unperturbed wavefront. The wavefront-orthonormal perturbations $p_1^q(t), p_2^q(t)$ are wavefront-orthonormal projections of the perturbed slowness vector. This perturbed slowness vector, wherein, is considered at the point on the perturbed ray corresponding to the ray-centered coordinates $q_1(t), q_2(t)$. This is the point where the wavefront-tangent plane intersects the perturbed ray (see Fig. 3.1).

We emphasize that the ray-centered coordinates approach doesn't describe the equal-time perturbations. The point of intersection of the wavefront-tangent plane by the perturbed ray corresponds to the traveltime computed along the perturbed ray, which is generally different from the traveltime t computed along the reference ray. If the vector of perturbation $\triangle\mathbf{x}(t)$ doesn't belong to the plane tangent to the unperturbed wavefront, the ray-centered values $q_1(t), q_2(t)$ correspond to a point on the perturbed ray at slightly shifted traveltime, $\mathbf{x}^{(1)}(t-\triangle t)$. We will show further that up to the first-order this time lag is exactly the time lag introduced in the previous subsection. Similarly, the ray-centered values $p_1^q(t), p_2^q(t)$ correspond to the time shifted slowness vector of the perturbed ray, $\mathbf{p}^{(1)}(t-\triangle t)$. The following relations hold:

$$\mathbf{x}^{(0)}(t) + q_\alpha(t)\,\mathbf{e}_\alpha(t) = \mathbf{x}^{(1)}(t-\triangle t), \qquad p_\alpha(t) = \left(\mathbf{p}^{(1)}(t-\triangle t), \mathbf{e}_\alpha(t)\right), \qquad \alpha = 1,2. \tag{3.29}$$

When $\triangle t > 0$ ($\triangle t < 0$), the equal-time point, $\mathbf{x}^{(1)}(t)$, outruns (is delayed with respect to) the point defined by the ray-centered approach, $\mathbf{x}^{(1)}(t-\triangle t)$ (see Fig. 3.1).

Let us expand the first identity in eq. 3.29 assuming the time lag $\triangle t$ to be small:

$$\triangle\mathbf{x}(t) = q_\alpha(t)\,\mathbf{e}_\alpha(t) + \frac{d\mathbf{x}}{dt}^{(1)}(t)\triangle t = q_\alpha(t)\,\mathbf{e}_\alpha(t) + \mathbf{u}^{(1)}(t)\triangle t. \tag{3.30}$$

Neglecting the higher-order terms, we get:

$$\triangle\mathbf{x}(t) = q_\alpha(t)\,\mathbf{e}_\alpha(t) + \mathbf{u}^{(0)}(t)\triangle t. \tag{3.31}$$

Projecting this equation to the direction of wavefront normal confirms that the time lag is determined up to the first-order with the normal projection $\triangle n$: $\triangle t = \frac{\triangle n}{v}$. As previously mentioned, it is constant when no model perturbation is present. Next, we relate the equal-time perturbation projections $\triangle x_1^q, \triangle x_2^q$ and the wavefront-orthonormal perturbations q_1, q_2 by projecting eq. (3.31) to the wavefront-orthonormal basis:

$$\triangle x_\alpha^q = q_\alpha + \triangle t\, u_\alpha^q \qquad \alpha = 1,2. \tag{3.32}$$

Analogously, we expand the second identity in eq. 3.29, neglect the higher-order terms, and relate the quantities describing perturbation of the slowness vector:

$$p_\alpha^q(t) = \left(\mathbf{p}^{(1)}(t-\triangle t), \mathbf{e}_\alpha(t)\right) = \left(\mathbf{p}^{(1)}(t) - \frac{d\mathbf{p}}{dt}^{(1)}(t)\triangle t, \mathbf{e}_\alpha(t)\right) =$$

$$(\triangle\mathbf{p}(t), \mathbf{e}_\alpha(t)) + \triangle t\left(\frac{\nabla_{\mathbf{x}} v}{v}, \mathbf{e}_\alpha(t)\right), \qquad \alpha = 1,2, \tag{3.33}$$

$$\triangle p_\alpha^q = p_\alpha^q + \triangle t\left(-\frac{v_\alpha}{v}\right), \qquad \alpha = 1,2. \tag{3.34}$$

We observe a discrepancy between the equal-time perturbation projections and the wavefront-orthonormal perturbations when ray perturbation is caused by initial conditions with $\triangle n(t_0) \neq 0$. As will be shown later, this discrepancy takes place also for the ray perturbation caused by anisotropic model. In the isotropic limit, relation (3.32) turns to identity $\triangle x^q_\alpha = q_\alpha$.

Let us now look at the wavefront-orthonormal perturbations from a different perspective. Due to linearity and homogeneity of the system (3.23), a general problem with initial conditions

$$\triangle \mathbf{x}(t_0) = \triangle x^q_\alpha(t_0)\, \mathbf{e}_\alpha(t_0) + \triangle n(t_0)\, \mathbf{e}_n(t_0), \tag{3.35}$$
$$\triangle \mathbf{p}(t_0) = \triangle p^q_\alpha(t_0)\, \mathbf{e}_\alpha(t_0) - \frac{1}{v^2(t_0)} \left(v_\alpha(t_0) \triangle x^q_\alpha(t_0) + v(t_0) u^q_\alpha(t_0) \triangle p^q_\alpha(t_0) + v_n(t_0) \triangle n(t_0)\right) \mathbf{e}_n(t_0)$$

is splitted into two specific problems. The ray-tangent problem (Červený, 2001) with initial conditions

$$\begin{aligned} \triangle \mathbf{x}^I(t_0) =& \triangle t\, u_\alpha(t_0) \mathbf{e}_\alpha(t_0) + \triangle n(t_0)\, \mathbf{e}_n(t_0) = \triangle t\, \mathbf{u}(t_0), \\ \triangle \mathbf{p}^I(t_0) =& \triangle t \left(-\frac{\nabla_{\mathbf{x}} v}{v}(t_0), \mathbf{e}_\alpha(t_0)\right) \mathbf{e}_\alpha(t_0) - \frac{v_n}{v^2}(t_0) \triangle n(t_0)\, \mathbf{e}_n(t_0) = \triangle t \left(-\frac{\nabla_{\mathbf{x}} v}{v}\right)(t_0), \end{aligned} \tag{3.36}$$

and the initial point of the ray perturbed along the reference ray and the slowness vector perturbation taken accordingly to follow the reference ray, doesn't require additional computing. It is easy to see that the right-hand side of the kinematic ray tracing system (3.1, 3.2) satisfies the dynamic ray tracing system (3.7) itself. Therefore,

$$\begin{pmatrix} \triangle \mathbf{x}^I \\ \triangle \mathbf{p}^I \end{pmatrix}(t) = \triangle t \begin{pmatrix} \mathbf{u} \\ -\frac{\nabla_{\mathbf{x}} v}{v} \end{pmatrix}(t) \tag{3.37}$$

The time lag $\triangle t = \frac{\triangle n(t)}{v(t)}$ is a constant coefficient between the infinitesimal ray-tangent perturbation and the ray velocity vector. Note, this is only valid for the perturbation by initial conditions. A remaining part of solution of the general problem:

$$\begin{aligned} \triangle \mathbf{x}^{II}(t) &= (\triangle x^q_\alpha - \triangle t\, u^q_\alpha)\, \mathbf{e}_\alpha, \\ \triangle \mathbf{p}^{II}(t) &= \left(\triangle p^q_\alpha - \triangle t \left(-\frac{v_\alpha}{v}\right)\right) \mathbf{e}_\alpha + \left(-\frac{v_\alpha}{v^2} \triangle x^q_\alpha - \frac{u^q_\alpha}{v} \triangle p^q_\alpha\right) \mathbf{e}_n. \end{aligned} \tag{3.38}$$

$\triangle \mathbf{x}$ for this remaining part stays always in the wavefront-tangent plane and can be computed by the homogeneous 4×4 dynamic ray tracing (since $\triangle n(t) = \triangle n(t_0) = 0$, see eq. 3.26). The shifted values of projections $\triangle x^q_1, \triangle x^q_2$ and $\triangle p^q_1, \triangle p^q_2$ arising in eq. (3.38) are exactly the perturbations in wavefront-orthonormal coordinates (see eqs 3.32 and 3.34). Therefore, they satisfy the homogeneous 4×4 dynamic ray tracing system even for $\triangle n(t_0) \neq 0$:

$$\frac{d}{dt} \begin{pmatrix} q_1 \\ q_2 \\ p^q_1 \\ p^q_2 \end{pmatrix} = S^{(4)} \begin{pmatrix} q_1 \\ q_2 \\ p^q_1 \\ p^q_2 \end{pmatrix}. \tag{3.39}$$

This agrees with the isotropic case (Farra and Madariaga, 1987, eq. 8). With the help of relations (3.32, 3.34) it can be alternatively explained as follows. The projections $\triangle x^q_1, \triangle x^q_2$

and $\triangle p_1^q, \triangle p_2^q$ satisfy the inhomogeneous system (3.28). Therefore, for the wavefront-orthonormal perturbations q_1, q_2 and p_1^q, p_2^q to satisfy the corresponding homogeneous system, it is necessary and sufficient that the residual vector

$$\triangle t \begin{pmatrix} u_1^q \\ u_2^q \\ -v_1/v \\ -v_2/v \end{pmatrix} \tag{3.40}$$

satisfies the inhomogeneous system (3.28) as well. Components of the residual vector are, however, projections of the right-hand side of the kinematic ray tracing system (3.1-3.2), which is a solution of the 6×6 dynamic ray tracing. Therefore, the residual vector has to satisfy the inhomogeneous system for projections (3.28). Note, for the ray-tangent perturbations $q_1 = q_2 = p_1^q = p_2^q = 0$.

To obtain the Cartesian equal-time perturbations directly from the wavefront-orthonormal ray-centered perturbations, the following relations can be used:

$$\begin{aligned} \triangle \mathbf{x} &= q_\alpha \mathbf{e}_\alpha + \triangle t \ \mathbf{u}, \\ \triangle \mathbf{p} &= p_\alpha^q \mathbf{e}_\alpha - \frac{1}{v^2}(v_\alpha q_\alpha + v u_\alpha^q p_\alpha^q) + \triangle t \left(-\frac{\nabla v}{v} \right). \end{aligned} \tag{3.41}$$

3.4 Perturbation by the anisotropic model

We now proceed to consider the perturbations caused by a small change in the anisotropic model.

3.4.1 Global Cartesian coordinates

First, we formulate computing of the equal-time perturbations $\triangle \mathbf{x}(t) = \mathbf{x}^{(1)}(t) - \mathbf{x}^{(0)}(t)$ and $\triangle \mathbf{p}(t) = \mathbf{p}^{(1)}(t) - \mathbf{p}^{(0)}(t)$. A reference ray $\mathbf{x}^{(0)}(t)$ and the reference slowness vector $\mathbf{p}^{(0)}(t)$ satisfy the kinematic ray tracing system (3.1-3.2) in the reference anisotropic model with density normalized elastic moduli $a_{ijkl}^{(0)}(\mathbf{x})$ and initial conditions $\mathbf{x}^{(0)}(t_0)$, $\mathbf{p}^{(0)}(t_0)$. A perturbed ray $\mathbf{x}^{(1)}(t)$ and the perturbed slowness vector $\mathbf{p}^{(1)}(t)$ satisfy the kinematic ray tracing system (3.1-3.2) as well but with slightly changed parameter values, $a_{ijkl}^{(1)}(\mathbf{x}) = a_{ijkl}^{(0)}(\mathbf{x}) + \triangle a_{ijkl}(\mathbf{x})$. Kinematic perturbations $\triangle \mathbf{x}, \triangle \mathbf{p}$ are assumed to be small as long as the perturbation of the model, $\triangle a_{ijkl}(\mathbf{x})$, is also small.

A linearized system for the kinematic perturbations in Cartesian coordinates is determined by the dynamic ray-tracing matrix $S^{(6)}$ and a source term with the model perturbation (Jech and Pšenčík, 1989; Farra, 1989):

$$\begin{aligned} \frac{d}{dt}\triangle x_i &= \left(S_{11}^{(6)}\right)_{ij} \triangle x_j + \left(S_{12}^{(6)}\right)_{ij} \triangle p_j + \triangle a_{ijkl} g_j g_k p_l + \left(\hat{W} B\right)_{ij} \triangle a_{jklm} p_k p_l g_m, \quad i = 1,2,3 \\ \frac{d}{dt}\triangle p_i &= \left(S_{21}^{(6)}\right)_{ij} \triangle x_j + \left(S_{22}^{(6)}\right)_{ij} \triangle p_j - \frac{1}{2}\frac{\partial \triangle a_{jklm}}{\partial x_i} g_k g_l p_j p_m - \left(\hat{V} B\right)_{ij} \triangle a_{jklm} p_k p_l g_m. \end{aligned} \tag{3.42}$$

Here we use notations for the four 3×3 blocks of the $S^{(6)}$ matrix. Note that the source term comprises two parts. The first one is due to linear occurrence of the elastic moduli in the right-hand side of the kinematic ray tracing system (3.1-3.2). The second term is a result of accurate expansion of the polarization vectors. In fact, polarizations are determined with elastic moduli and direction of the wavefront normal. In the kinematic ray tracing system considered for the perturbed ray, perturbed polarization $\mathbf{g}^{(1)}$ is included correspondingly as a function of the moduli in a form $a^{(0)}_{ijkl}(\mathbf{x}^{(0)}+\triangle\mathbf{x})+\triangle a_{ijkl}(\mathbf{x}^{(0)}+\triangle\mathbf{x})$, which leads to extra terms containing the polarization derivatives with respect to the normalized elastic moduli (see Appendix D.1):

$$\frac{\partial g_i}{\partial a_{jklm}} = B_{ij}p_k p_l g_m, \qquad i,j,k,l,m = 1,2,3. \tag{3.43}$$

To fully formulate the perturbation problem, initial conditions for the kinematic perturbations has to be specified. Since the eikonal equation (3.5) is satisfied both for the unperturbed and for the perturbed quantities, perturbation of the slowness vector is related to the perturbation of ray and to the perturbation of elastic moduli (Farra, 1989):

$$(\mathbf{u},\triangle\mathbf{p}) = \left(-\frac{\nabla_{\mathbf{x}}v}{v},\triangle\mathbf{x}\right) - \frac{\triangle v}{v}, \tag{3.44}$$

where $\triangle v$ is a notation for the fixed normal perturbation of the phase velocity:

$$\triangle v = \frac{1}{2}v\triangle a_{ijkl}g_j g_k p_i p_l. \tag{3.45}$$

Eq. (3.44) differs from eq. (3.22) by this additional term containing the model perturbation. For an additional discussion on initial conditions reasonable for the kinematic perturbations, we refer to Appendix B.2.

The inhomogeneous system (3.42) can be solved with the 6×6 wave propagator $\Pi^{(6)}$ and the system source vector $\mathbf{s}^{(6)}$ as follows (e. g., Gilbert and Backus, 1966):

$$\begin{pmatrix}\triangle\mathbf{x}\\ \triangle\mathbf{p}\end{pmatrix}(t) = \Pi^{(6)}(t,t_0)\begin{pmatrix}\triangle\mathbf{x}\\ \triangle\mathbf{p}\end{pmatrix}(t_0) + \Pi^{(6)}(t,t_0)\int\limits_{t_0}^{t}\left(\Pi^{(6)}(\tilde{t},t_0)\right)^{-1}\mathbf{s}^{(6)}(\tilde{t})d\tilde{t}. \tag{3.46}$$

Simplicticity of the wave propagator (e. g., Červený, 2001) may be additionally employed to compute the inverse using blocks:

$$\Pi^{-1} = \begin{pmatrix}\Pi_{22}^T & -\Pi_{12}^T\\ -\Pi_{21}^T & \Pi_{11}^T\end{pmatrix}. \tag{3.47}$$

3.4.2 Projections of the equal-time perturbations

Let us study projections of the kinematic perturbations onto the reference wavefront-orthonormal basis in this case. Due to eq. (3.44), five scalars $\triangle x_1^q$, $\triangle x_2^q$, $\triangle p_1^q$, $\triangle p_2^q$, and $\triangle n$ are sufficient for describing evolution of the perturbations:

$$\triangle\mathbf{x} = \triangle x_\alpha^q\,\mathbf{e}_\alpha + \triangle n\,\mathbf{e}_n, \tag{3.48}$$

$$\triangle\mathbf{p} = \triangle p_\alpha^q\,\mathbf{e}_\alpha - \frac{1}{v^2}(v_\alpha\triangle x_\alpha^q + v\,u_\alpha^q\triangle p_\alpha^q + v_n\triangle n + \triangle v)\,\mathbf{e}_n. \tag{3.49}$$

The projection $(\triangle\mathbf{p}, \mathbf{e}_n)$ follows from the eikonal equation perturbation (3.44). In contrast to the case of perturbation by initial conditions (see eq. 3.25), it comprises an extra term with $\triangle v$.

Differentiating the projections $\triangle x_1^q, \triangle x_2^q, \triangle p_1^q, \triangle p_2^q$, substituting eqs (3.42), basis decomposition (3.48, 3.49), and derivatives (3.15), we obtain again a system with the dynamic ray tracing matrix $S^{(4)}$ and a source term with $\triangle n$:

$$\begin{aligned}
\frac{d}{dt}\triangle x_\alpha^q &= \left(S_{11}^{(4)}\right)_{\alpha\beta}\triangle x_\beta^q + \left(S_{12}^{(4)}\right)_{\alpha\beta}\triangle p_\beta^q + \triangle n\left(\left(\hat{\Phi} + \hat{W}B\hat{V}^T\right)_{ij} e_{\alpha i}e_{nj} - \frac{v_n}{v}u_\alpha^q + v_\alpha\right) \\
&\quad + \triangle a_{ijkl}g_j g_k e_{\alpha i}p_l + (WB)_{\alpha i}\triangle a_{ijkl}p_j p_k g_l - \frac{u_\alpha^q}{v}\triangle v, \\
\frac{d}{dt}\triangle p_\alpha^q &= \left(S_{21}^{(4)}\right)_{\alpha\beta}\triangle x_\beta^q + \left(S_{22}^{(4)}\right)_{\alpha\beta}\triangle p_\beta^q + \triangle n\left(\left(\hat{Y} + \hat{V}B\hat{V}^T\right)_{ij} e_{\alpha i}e_{nj} + \frac{v_n}{v}v_\alpha\right) \\
&\quad - \frac{1}{2}\triangle a_{\alpha,ijkl}g_k g_l p_i p_l - (VB)_{\alpha i}\triangle a_{ijkl}p_j p_k g_l + \frac{v_\alpha}{v^2}\triangle v, \qquad \alpha = 1,2,
\end{aligned} \tag{3.50}$$

where $\triangle a_{\alpha,ijkl} = (\nabla\triangle a_{ijkl}, \mathbf{e}_\alpha)$. However, the source term now additionally comprises a vector with the elastic module perturbations (see eqs 3.26).

Computing time derivative of the projection $\triangle n$ yields an inhomogeneous independent equation for $\triangle n$:

$$\frac{d\triangle n}{dt} = v_n\triangle n + \triangle v. \tag{3.51}$$

We solve it with the method of variation of constants applied to the solution of the homogeneous problem (eqs 3.26):

$$\triangle n(t) = v(t)\left(\frac{\triangle n(t_0)}{v(t_0)} + \int_{t_0}^{t}\frac{\triangle v}{v}d\tilde{t}\right). \tag{3.52}$$

This expression can be placed to the source term of the system (3.50) closing it with respect to the unknown projections $\triangle x_1^q, \triangle x_2^q$ and $\triangle p_1^q, \triangle p_2^q$:

$$\begin{aligned}
\frac{d}{dt}\triangle x_\alpha^q &= \left(S_{11}^{(4)}\right)_{\alpha\beta}\triangle x_\beta^q + \left(S_{12}^{(4)}\right)_{\alpha\beta}\triangle p_\beta^q + \triangle t\left(v\left(\hat{\Phi} + \hat{W}B\hat{V}^T\right)_{ij} e_{\alpha i}e_{nj} - v_n u_\alpha^q + vv_\alpha\right) \\
&\quad + \triangle a_{ijkl}g_j g_k e_{\alpha i}p_l + (WB)_{\alpha i}\triangle a_{ijkl}p_j p_k g_l - \frac{u_\alpha^q}{v}\triangle v, \\
\frac{d}{dt}\triangle p_\alpha^q &= \left(S_{21}^{(4)}\right)_{\alpha\beta}\triangle x_\beta^q + \left(S_{22}^{(4)}\right)_{\alpha\beta}\triangle p_\beta^q + \triangle t\left(v\left(\hat{Y} + \hat{V}B\hat{V}^T\right)_{ij} e_{\alpha i}e_{nj} + v_n v_\alpha\right) \\
&\quad - \frac{1}{2}\triangle a_{\alpha,ijkl}g_k g_l p_i p_l - (VB)_{\alpha i}\triangle a_{ijkl}p_j p_k g_l + \frac{v_\alpha}{v^2}\triangle v, \qquad \alpha = 1,2,
\end{aligned} \tag{3.53}$$

where

$$\triangle t(t) = \frac{\triangle n(t)}{v(t)} = \frac{\triangle n(t_0)}{v(t_0)} + \int_{t_0}^{t}\frac{\triangle v}{v}d\tilde{t}. \tag{3.54}$$

Note, this time lag now consists of two terms, due to the perturbation of initial ray point and due to the model perturbation. The latter one is opposite to the first-order correction

of the traveltime along the unperturbed ray (e. g., Jech and Pšenčík, 1989)

$$\triangle\tau = -\int_{t_0}^{t} \frac{\triangle v}{v} d\tilde{t}. \tag{3.55}$$

3.4.3 Perturbations in wavefront-orthonormal coordinates

Verifying the derivations from Section 3.3.3, we confirm the same relations between the equal-time perturbation projections and the wavefront-orthonormal perturbations for the case of perturbation by anisotropic model:

$$\triangle x^q_\alpha = q_\alpha + \triangle t\, u^q_\alpha, \qquad \triangle p^q_\alpha = p^q_\alpha + \triangle t \left(-\frac{v_\alpha}{v}\right), \qquad \alpha = 1, 2. \tag{3.56}$$

However, the time lag $\triangle t$ is not a constant anymore (see eq. 3.54):

$$\frac{d}{dt}\triangle t = \frac{\triangle v}{v}. \tag{3.57}$$

Unlike the case of perturbations caused by the initial conditions, the discrepancy between the equal-time perturbation projections and the wavefront-orthonormal perturbations is present for $t \neq t_0$ even when the reference and the perturbed ray emerge from the same location.

Using eq. (3.57) and the fact that the projected right-hand side vector, eq. (3.40) without the factor $\triangle t$, satisfies the inhomogeneous system for projections (3.28) with $\triangle t = 1$, we find an expression for the derivative of the residual vector:

$$\begin{aligned}
\frac{d}{dt}\triangle t u^q_\alpha \quad &= \quad \frac{u^q_\alpha}{v}\triangle v + \left(S^{(4)}_{11}\right)_{\alpha\beta} \triangle t u^q_\beta + \left(S^{(4)}_{12}\right)_{\alpha\beta} \triangle t \left(-\frac{v_\beta}{v}\right) \\
&\qquad + \triangle t \left(v \left(\hat{\Phi} + \hat{W} B \hat{V}^T\right)_{ij} e_{\alpha i} e_{nj} - v_n u^q_\alpha + v v_\alpha\right), \\
\frac{d}{dt}\triangle t \left(-\frac{v_\alpha}{v}\right) &= -\frac{v_\alpha}{v^2}\triangle v + \left(S^{(4)}_{21}\right)_{\alpha\beta} \triangle t u^q_\beta + \left(S^{(4)}_{22}\right)_{\alpha\beta} \triangle t \left(-\frac{v_\beta}{v}\right) \\
&\qquad + \triangle t \left(v \left(\hat{Y} + \hat{V} B \hat{V}^T\right)_{ij} e_{\alpha i} e_{nj} + v_n v_\alpha\right), \qquad \alpha = 1, 2.
\end{aligned} \tag{3.58}$$

Together with relations (3.56), it helps to transform the system for the wavefront-orthonormal projections (3.53) to a reduced system for the ray-centered perturbations:

$$\begin{aligned}
\frac{dq_\alpha}{dt} &= \left(S^{(4)}_{11}\right)_{\alpha\beta} q_\beta + \left(S^{(4)}_{12}\right)_{\alpha\beta} p^q_\beta + \triangle a_{ijkl} g_j g_k e_{\alpha i} p_l \quad + (WB)_{\alpha i} \triangle a_{ijkl} p_j p_k g_l - 2\frac{u^q_\alpha}{v}\triangle v, \\
\frac{dp^q_\alpha}{dt} &= \left(S^{(4)}_{21}\right)_{\alpha\beta} q_\beta + \left(S^{(4)}_{22}\right)_{\alpha\beta} p^q_\beta - \frac{1}{2}\triangle a_{\alpha,ijkl} g_k g_l p_i p_l - (VB)_{\alpha i} \triangle a_{ijkl} p_j p_k g_l \; + 2\frac{v_\alpha}{v^2}\triangle v, \\
&\qquad\qquad\qquad\qquad\qquad\qquad\qquad\qquad\qquad\qquad\qquad\qquad \alpha = 1, 2.
\end{aligned} \tag{3.59}$$

This is an anisotropic analogue of equations formulated by Farra and Madariaga (1987, eq. 11) for the kinematic ray-centered perturbations in isotropic media.

It can be solved with the 4×4 wave propagator $\Pi^{(4)}$ and the source vector of the system $\mathbf{s}^{(4)}$ as follows (e. g., Gilbert and Backus, 1966):

$$\begin{pmatrix} q_1 \\ q_2 \\ p_1^q \\ p_2^q \end{pmatrix}(t) = \Pi^{(4)}(t,t_0) \begin{pmatrix} q_1 \\ q_2 \\ p_1^q \\ p_2^q \end{pmatrix}(t_0) + \Pi^{(4)}(t,t_0) \int\limits_{t_0}^{t} \left(\Pi^{(4)}(\tilde{t},t_0)\right)^{-1} \mathbf{s}^{(4)}(\tilde{t}) d\tilde{t}. \tag{3.60}$$

Simplicticity of the wave propagator may be employed to compute the inverse (see eq. 3.47).

To obtain the Cartesian equal-time perturbations directly from the wavefront-orthonormal ray-centered quantities, the following relations can be used:

$$\begin{aligned} \triangle\mathbf{x} &= q_\alpha \mathbf{e}_\alpha + \triangle t \ \mathbf{u}, \\ \triangle\mathbf{p} &= p_\alpha^q \mathbf{e}_\alpha - \frac{1}{v^2}(v_\alpha q_\alpha + v u_\alpha^q p_\alpha^q + \triangle v) + \triangle t \left(-\frac{\nabla v}{v}\right). \end{aligned} \tag{3.61}$$

These transformation has an additional term with $\triangle v$ (see 3.41).

3.5 Numerical examples

To evaluate the theory, we solve the equations numerically in a 2D inhomogeneous VTI medium for the qP-wave. Thomsen's anisotropic parameters v_{P0}, v_{S0}, ε, and δ (Thomsen, 1986) linearly increase with depth in the background model (Figs 3.2, 3.4, 3.6, 3.8): $v_{P0} = 2.2 \div 2.6$ km/s, $v_{S0} = 1.0 \div 1.4$ km/s, $\varepsilon = 0.2 \div 0.3$, $\delta = -0.1 \div -0.2$. The extreme values are given at the zero depth and at the 620 m depth correspondingly. First, we trace a ray in the background model from the zero depth to the subsurface (unperturbed ray marked with dash-dotted lines in Figs 3.2, 3.4, 3.6, 3.8). Its initial $x = 25$ m and $p_x = 0.2143$ s/km.

We independently consider perturbations of the Thomsen's parameters by adding localized anomalies to the background model in the vicinity of the unperturbed ray (Figs 3.2, 3.4, 3.6, 3.8). The anomalies are bump functions proportional to $\exp\left(\frac{(\mathbf{x}-\mathbf{x}_0)^2}{(\mathbf{x}-\mathbf{x}_0)^2-R^2}\right)$ with a radius of $R = 50$ m and centered at a point with coordinates $x_0 = 175$ m, $z_0 = 175$ m. Corresponding coefficients in front of the exponential function are $\triangle v_{P0} = 0.03$ km/s, $\triangle v_{S0} = 0.6$ km/s, $\triangle\varepsilon = 0.05$, $\triangle\delta = -0.02$. For all four cases of perturbation, we trace rays with the same initial conditions as for the unperturbed ray (solid lines in Figs 3.2, 3.4, 3.6, 3.8). The elastic module perturbations are chosen relatively small to adequately be described by the first-order ray perturbation theory. On the other hand, the qP-ray is barely sensitive to the v_{S0} parameter leading to a higher value of the velocity anomaly $\triangle v_{S0}$.

Subtracting unperturbed rays and slowness vectors from the perturbed ones yields "exact" perturbations, which are further compared with those perturbations computed by the ray perturbation approaches in Cartesian and wavefront-orthonormal coordinates (Figs 3.3, 3.5, 3.7, 3.9). We compute the kinematic perturbations using both the direct Cartesian coordinates approach, eq. (3.46) with the zero initial conditions, and the reduced wavefront-orthonormal approach, eq. (3.60) with the zero initial conditions, followed by the transformation (3.61). Figs 3.3a, 3.5a, 3.7a, 3.9a show the resulting components of ray perturbation. Figs 3.3b, 3.5b, 3.7b, 3.9b show the components of slowness vector perturbation. In all examples, we observe a good consistency between the exact and the linearized

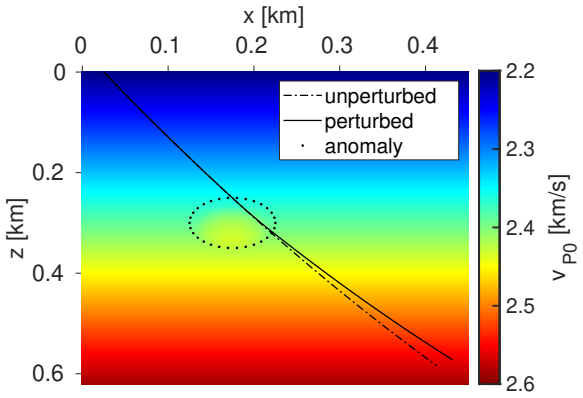

Figure 3.2: Vertical compressional velocity v_{P0} of the perturbed model together with the perturbed and unperturbed rays. The high-velocity anomaly highlighted with black dots was added to the constant gradient background.

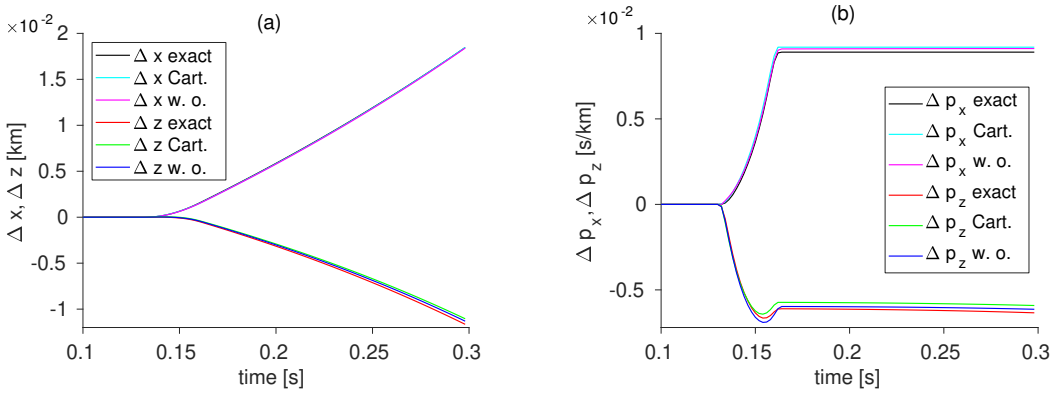

Figure 3.3: Comparison of the kinematic perturbations computed with the "exact", the Cartesian, and the wavefront-orthonormal approaches in the case of v_{P0}-anomaly: the ray perturbation components (a) and the slowness vector perturbation components (b).

perturbations. The Cartesian and wavefront-orthonormal approaches yield similar results, which differ from the exact perturbations as much as the first-order theory allows for. The Cartesian and wavefront-orthonormal perturbations are close to each other. Sometimes the wavefront-orthonormal approach exhibit a better fit, as shown in Figs 3.3a, 3.3b. Sometimes the Cartesian solution is closer to the exact perturbations (Figs 3.3a, 3.3b). This confirms the validity of the newly formulated anisotropic ray perturbation theory in wavefront-orthonormal coordinates.

3.6 Discussion

In the present study, we have investigated the kinematic ray tracing perturbations in the wavefront-orthonormal coordinates. We derived an anisotropic analogue of the equations

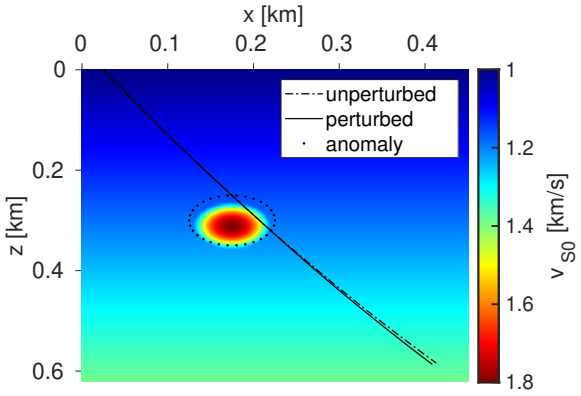

Figure 3.4: Vertical shear velocity v_{S0} of the perturbed model together with the perturbed and unperturbed rays. The high-velocity anomaly highlighted with black dots was added to the constant gradient background.

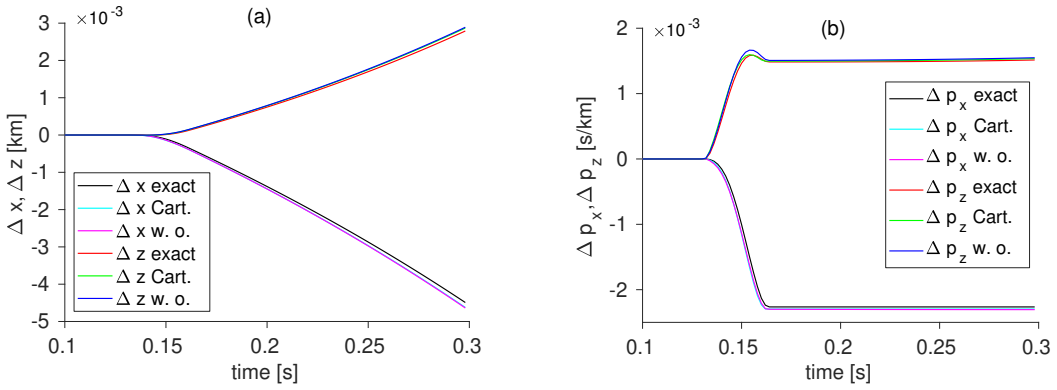

Figure 3.5: Comparison of the kinematic perturbations computed with the "exact", the Cartesian, and the wavefront-orthonormal approaches in the case of v_{S0}-anomaly: the ray perturbation components (a) and the slowness vector perturbation components (b).

by Farra and Madariaga (1987). Originally, the authors used expansion of the isotropic ray-centered Hamiltonian. However, we worked directly with ordinary differential equations avoiding an interesting question about formulation of the wavefront-orthonormal ray-centered Lagrangian and Hamiltonian in the anisotropic case.

As well as the dynamic ray tracing quantities, ray and slowness vector perturbations can be alternatively computed either in Cartesian or wavefront-orthonormal coordinates depending on the available code.

The perturbation theory method can be also applied to the dynamic ray tracing. In the first place, the dynamic ray tracing results in wave amplitudes. Secondly, the dynamic ray tracing allows for a local construction of the wavefront by computing the wavefront curvatures (e. g., Červený, 2001). In particular, we are motivated by a need for computing the Fréchet derivative of the wavefront curvature for the velocity model building (Duveneck, 2004; Dell et al., 2014; Bauer et al., 2017; Diekmann et al., 2019; Znak et al., 2019). The

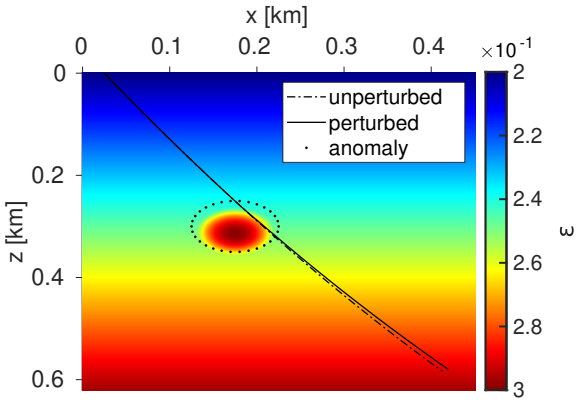

Figure 3.6: Thomsen's parameter ε of the perturbed model together with the perturbed and unperturbed rays. The anomaly of ε highlighted with black dots was added to the constant gradient background.

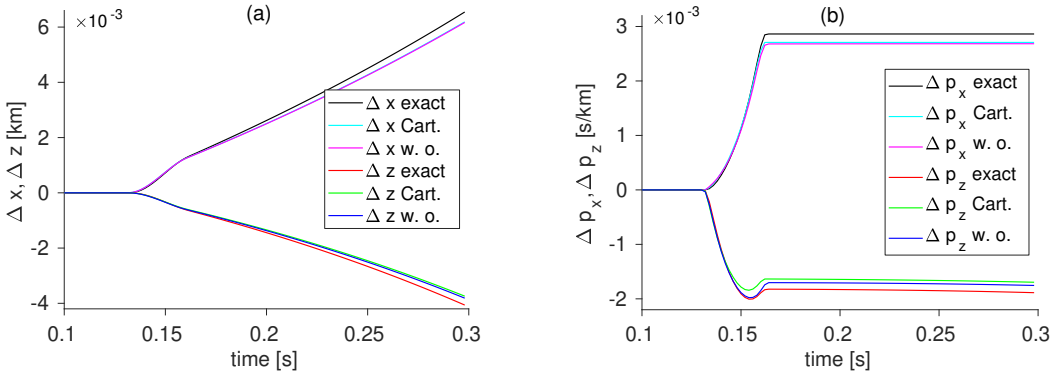

Figure 3.7: Comparison of the kinematic perturbations computed with the "exact", the Cartesian, and the wavefront-orthonormal approaches in the case of ε-anomaly: the ray perturbation components (a) and the slowness vector perturbation components (b).

wavefront attributes, such as traveltime, horizontal components of slowness vector and wavefront curvatures, can be extracted from noisy seismic data by the Common-Reflection-Surface stack (Jäger et al., 2001). In anisotropic media, it is also possible using an accurate interpretation of the hyperbolic traveltime parameters (Vanelle et al., 2018).

Jech and Pšenčík (1989) suggested to utilize the 6×6 system for the perturbations of the dynamic ray tracing. Farra (1989) also presented such a system in terms of the perturbation of the Cartesian Hamiltonian. Pšenčík and Farra (2005) derived it explicitly for the case of weak anisotropy.

Since the wavefront curvature matrix is directly expressed using the wavefront-orthonormal dynamic ray tracing matrices as $M = PQ^{-1}$ (e. g., Červený, 2001), its perturbation can be also described naturally with perturbations of the wavefront-orthonormal dynamic ray tracing matrices. If we adhere the same strategy for perturbation of the 4×4 dynamic ray tracing in wavefront-orthonormal coordinates, working directly with the differential

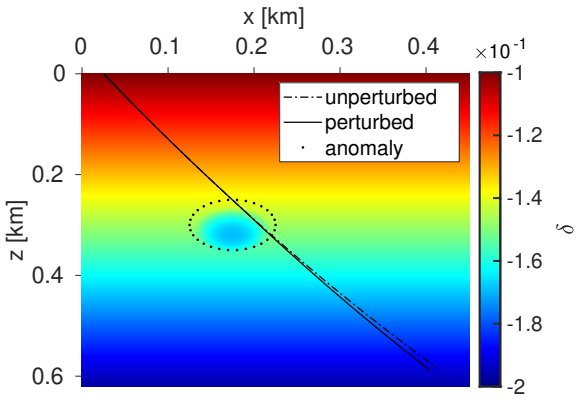

Figure 3.8: Thomsen's parameter δ of the perturbed model together with the perturbed and unperturbed rays. The anomaly of δ highlighted with black dots was added to the constant gradient background.

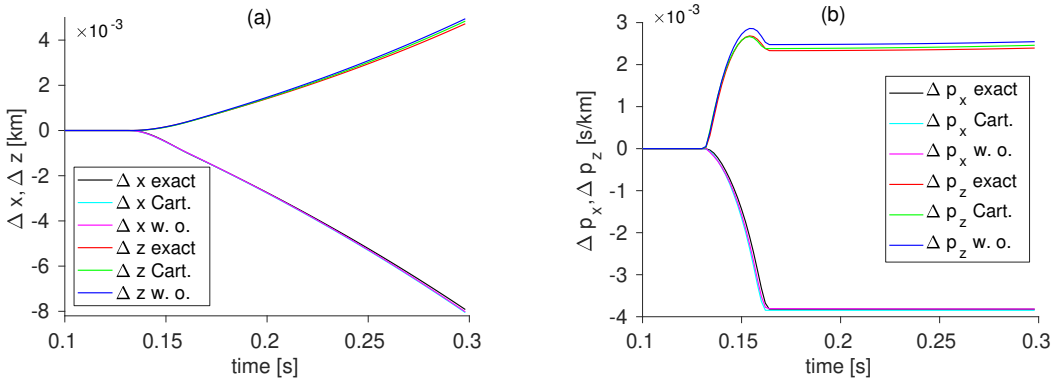

Figure 3.9: Comparison of the kinematic perturbations computed with the "exact", the Cartesian, and the wavefront-orthonormal approaches in the case of δ-anomaly: the ray perturbation components (a) and the slowness vector perturbation components (b).

equations without expansion of the ray-centered Hamiltonian, we would face an interesting problem of the wavefront-orthonormal basis perturbation. Not only the ray and slowness vector derivatives differ on the perturbed ray, but it also concerns the basis vectors used for projecting.

3.7 Conclusions

We have developed the first-order ray perturbation theory in the local wavefront-orthonormal coordinates. It is generally formulated for 3D inhomogeneous anisotropic solids. Two first-order linear systems of differential equations respectively allow for computing partial derivatives of ray and slowness vector with respect to the ray tracing initial conditions and the Fréchet derivatives of ray and slowness vector with respect to the density normalized elastic moduli. These systems are respectively a homogeneous and an inhomogeneous dynamic ray tracing system in wavefront-orthonormal coordinates. They have less equations than in the Cartesian coordinates formulation. In 3D, the 4×4 wave propagator can be utilized instead of the Cartesian 6×6 wave propagator. However, the wavefront-orthonormal basis needs to be additionally computed. In 2D, the basis is determined automatically after kinematic ray tracing as the wavefront normal and the unique tangent vector. The 2×2 propagator formalism can be utilized instead of the Cartesian 4×4 one in this case. We have considered two ways for describing ray perturbations – the equal-time perturbation projections and the wavefront-orthonormal coordinates. They are transformed into each other using a time lag, which generally needs extra integration in the first-order correction of traveltime. Our studies of relations between them have revealed simplification of the ray perturbation equations for the wavefront-orthonormal coordinates approach. Numerical tests have confirmed validity of the proposed method.

Acknowledgments

We are grateful to Dr. Ivan Pšenčík for a detailed review of the manuscript and convincing us to switch to the case of general 3D anisotropy from the elliptical case. This work was carried out in the frame of the project on diffraction inversion funded by the Federal Ministry for Economic Affairs and Energy of Germany (03SX427B). The authors also thank the Wave Inversion Technology (WIT) Consortium for the support.

4 Identification and focusing of edge diffractions with wavefront attributes

Abstract

The wavefront attributes locally characterize propagation of the body waves, thus are routinely extracted from seismic data using various traveltime approximations. In the 3D zero-offset case, they encompass the first- and second-order traveltime derivatives of the so-called NIP- and N-waves. We propose utilizing them to identify and isolate different types of 3D wave propagation: point diffractions, edge diffractions, and specular reflections. Therefore, we formulate a missing wavefront curvature based criterion for diffraction from an arbitrarily oriented and possibly curved edge in 3D heterogeneous and anisotropic media. Additionally, we propose a method, also based on the wavefront attributes, for sorting traces into specific groups in order to get ray focusing of the edge diffraction during back propagation. The traveltime response of 3D edge diffraction behaves as a 2D diffraction, but locally and in a specific direction, which changes from point to point. This fact allows us to construct a vector field of such directions on the acquisition surface by solving a system of homogeneous algebraic equations with a residual matrix. The residual matrix is simply a difference between the NIP- and the N-wavefront curvature matrices. Accordingly, the edge diffraction criterion can be formulated as a solvability condition for this homogeneous system. It utilizes vanishing of the residual matrix determinant. Inspecting the columns of the residual matrix, which are zeros for point diffraction and non-zeros for edge diffraction allows for complete classification. Building integral curves of the investigated directional field allows for appropriate receiver grouping. The rays propagated downward from such a curve focus at a particular point on the edge. Using traveltime simulations and ray tracing, we confirm the proposed edge identification criterion and the method of edge diffraction focusing in a heterogeneous isotropic and a homogeneous anisotropic VTI model.

4.1 Introduction

Wavefront attributes are routinely retrieved during multiparameter and multidimensional stacking of seismic data. In the 3D case, they are two horizontal components of the zero-offset slowness and six second-order derivatives of the NIP- and N-wave traveltimes. Usually, a fictitious wave induced by a source placed at the normal-incidence-point on the reflector is called NIP-wave (Hubral, 1983). "N-wave" is a term used to denote another fictitious wave that is triggered by the exploding reflector element. Throughout this paper, we also use the term wavefront curvature matrices to denote matrices of the second-order traveltime derivatives (see e.g., in Vanelle et al., 2018). The wavefront attributes describe the propagation of the seismic body waves and are used in various processing sequences. Duveneck (2004); Dell et al. (2014); Bauer et al. (2017); Znak et al. (2019) utilize the

wavefront attributes in the velocity model building. Baykulov and Gajewski (2009); Hoecht et al. (2009) use the wavefront attributes to interpolate the prestack seismic data and improve signal-to-noise ratio. Since the wavefront attributes locally describe the kinematics of the wave propagation, they can also be used to identify the type of the propagating wave. Dell and Gajewski (2011); Asgedom et al. (2013) exploit the wavefront attributes to, e.g., identify and isolate seismic diffractions from seismic reflections. Throughout the paper we distinguish between point and edge diffractions. The prominent examples of a diffractor, which produces the edge diffraction response, are such geological structures as faults, highly curved folds, cracks, and pinch-outs. A small-scale sphere (velocity inclusion) or a tip produce the point diffractions.

The criterion for identifying point diffraction in 3D media by fronts of the NIP- and N-wave considers that both matrices of wavefront curvatures fully coincide. The same criterion holds for 2D diffraction where matrices of wavefront curvatures reduce to scalar curvatures. Dell and Gajewski (2011); Rad et al. (2018) applied this equality condition to identify and separate diffractions from reflections using a binary reflection filter. Berkovitch et al. (2009); Asgedom et al. (2013) used the coherent summation along diffraction traveltimes to enhance diffracted events, which implies reflected events incoherently sum up when performing the amplitude summation along the stacking operator, which is parametrized in terms of the single wavefront curvature. Schwarz (2019) proposed an adaptive filter which exploits the coherent data summation and subtraction based on the wavefront attributes. All the methods, either based on coherent summation and subtraction or on binary filtering, allow for an unambiguous discriminating diffracted waves, separating them from the reflected ones and, as a consequence, a dedicated diffraction processing (see e.g., in Alonaizi et al., 2013; Bauer et al., 2017; Dell et al., 2018; Keydar and Landa, 2019; Yin and Nakata, 2019). Moreover, both a point and an edge diffractor produce a kinematically equivalent response in the 2D case (see e.g., in Dell et al., 2018). This means the waterfront curvatures are equal independently of the type of the diffracting object and the same separation criterion can be used to isolate edge diffraction. In the 3D case, however, response from the edge diffractor differs from response from the point diffractor. The 2D criterion holds only for particular edge types and acquisition symmetry, for instance when the edge is horizontal and straight and the isotropic medium is invariant in the direction along this edge. Moreover, the acquisition line should be orthogonal to the edge as shown in Figure 4.1 a) and b).

In this paper, we show how to find the 2D lines in a 3D survey where the 2D criterion fulfills. We generalize our approach to an arbitrarily oriented and curved edge in heterogeneous media, including anisotropy. We propose a separation and identification of the diffraction response in the data domain. The separation methods in the image (migrated) domain have been described in the literature as well, (see eg., Moser and Howard, 2008; Klokov and Fomel, 2012). S. Dell and Hoelker (2019), for instance, showed that the edge diffraction response in the Kirchhoff migration operator is mainly distributed along a certain azimuth direction, so-called stationary curve. This property allows one to separate edge diffractions in the image (migrated) domain. Moreover, the stationary curve, which gives the most contribution to the Kirchhoff integral, is the focusing curve discussed in details further in this paper. The image-domain methods yield the focused amplitudes of the isolated diffractions which are very suitable for a structural interpretation but not suitable for a subsequent processing based on diffractions, e.g., focusing tomography (Znak et al., 2019).

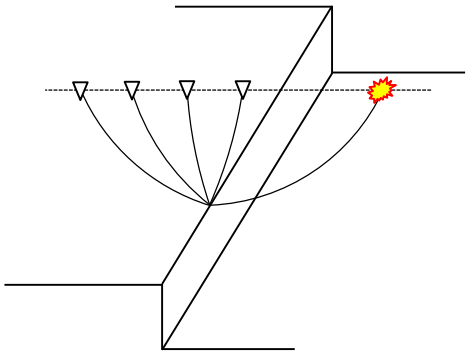

Figure 4.1: A schematic example of an acquisition line in a 3D edge model, where the 2D criterion is fulfilled. The prominent examples of the 3D edge diffractors are such geological structures as faults, highly curved folds, cracks, and pinch-outs.

In this paper we focus only on the kinematic characteristics of the edge diffractions. The kinematics of the edge diffractions can be described using geometrical optics. Keller (1962) formulated the geometrical optics law for the edge diffractions first in isotropic media, which was extended by Rosenbaum (1967a,b) to anisotropic case. Bakker (1990) suggested an algorithm based on dynamic ray tracing to evaluate edge diffraction amplitudes in the vicinity of the shadow zone boundary. For a comprehensive acquaintance with the theory of the edge diffractions, including phase and amplitudes computation, and review of existing asymptotic methods, we refer the reader to (Klem-Musatov et al., 2008). We consider that an edge diffractor is a curved segment, i.e., an 1D object, thus its seismic response can kinematically be focused to a point similarly as for a point diffraction. We propose to specify independent groups of central midpoints in a way the backpropagated rays constituting one group focus on the edge at a specific point. This fulfills when the wavefront attributes are determined in a vicinity of a specific curve on the surface, which we call the focusing curve. In the mentioned-above symmetric cases, the focusing curves regress to the straight lines orthogonal to the edge. We provide an algorithm based on the NIP- and N-wave curvature matrices to build the focusing curves on the acquisition surface. We also show that a 3D edge-diffraction response kinematically behaves as a 2D diffraction, but locally and in a specific direction, which changes from point to point. We first construct a vector field of such directions by solving a system of homogeneous algebraic equations with so-called residual matrix. The residual matrix contains residuals of the wavefront curvature matrices. The focusing curves are then retrieved as integral curves of the resulting tangent vector field. We also formulate a general criterion for identification and separation of the edge diffractions in seismic data. We show that the determinant of a residual matrix of the second-order derivatives of NIP- and N-wave vanishes for the edge diffraction. We emphasize a connection of this criterion with the equations for the geometrical spreading of a zero-offset reflected wave (Eq. 14 and Eq. 25 in Hubral, 1983). The geometrical spreading becomes singular as long as the separation criterion fulfills.

The paper consists of a part describing the theoretical concept and a part with numerical tests that prove the concept. In the methodological section, we first recall the geometrical law of edge diffraction, formulate an identification criterion based on wavefront-curvatures and describe an algorithm for discriminating edge diffractions, point diffractions, and re-

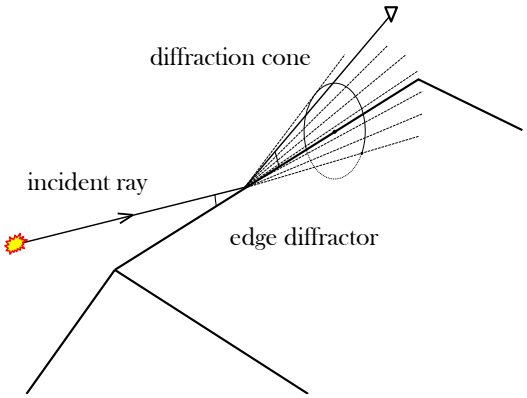

Figure 4.2: The geometrical law of edge diffraction: an illustration in isotropic case. The angle of the cone formed by the diffracted rays equals the angle between the incident ray and the edge.

flections. Additionally, we present an algorithm for receiver grouping, which allows one to kinematically focus the edge diffraction. In the example section, we show an application to synthetic models comprising an edge embedded in isotropic heterogeneous and homogeneous vertically transverse isotropic medium, respectively. We also provide technical appendices at the end of the paper with discussion on regularity of focusing curves, description of an alternative derivation of the separation criterion by the dynamic ray tracing method, and a short derivation of the equations for geometrical spreading.

4.2 Theory and method

4.2.1 Geometrical optics considerations for scattering on edge

A point diffractor scatters rays in all possible directions while the scattering at edge obeys the geometrical law of diffraction (Keller, 1962; Klem-Musatov et al., 2008). This implies, an incident ray evokes diffracted rays in a particular geometric shape, so-called Keller (diffraction) cone, which is formed around the edge (Figure 4.2). An angle of the diffraction cone is equal to the angle between the incident ray and the edge due to Fermat's principle. In the anisotropic case, geometric shapes formed by the diffracted rays may be complex. However, in each plane containing the tangent to the edge, diffracted rays may arise with a tangent slowness that equals to the tangent slowness of the incident ray (Rosenbaum, 1967a,b; Felsen, 1970).

4.2.2 Edge identification using wavefront attributes

Wavefront attributes usually encompass the first and second-order derivatives of emerging wavefront in midpoint and offset direction. They are directly related to two hypothetical waves, NIP and normal wave. NIP-wave is a wave induced by a source that is placed at the normal-incidence-point on the reflector. N-wave is triggered by an exploding reflector element. The wavefront attributes are fully sufficient to locally describe the propagation of the body waves, thus are routinely used in various traveltime approximations. In general,

we can consider common-reflection-surface (CRS) stacking as a part of paraxial traveltime approximations. This allows one to classify different CRS implementations depending on the approximation type. In the literature, one usually distinguishes between multifocusing (Landa et al., 2010), hyperbolic CRS (Jäger et al., 2001), non-hyperbolic CRS (Fomel and Kazinnik, 2013), and implicit CRS (Schwarz et al., 2014). We use a hyperbolic approximation that is formulated as followed

$$t^2 = (t_0 + 2(\mathbf{p}, \triangle\mathbf{x}_m))^2 + 2\,t_0 \left(\left(\mathbf{h}, \hat{M}_{NIP}\mathbf{h} \right) + \left(\triangle\mathbf{x}_m, \hat{M}_N \triangle\mathbf{x}_m \right) \right), \tag{4.1}$$

where $\mathbf{h} = \frac{1}{2}(\mathbf{x}_r - \mathbf{x}_s)$ is offset and $\triangle\mathbf{x}_m = \frac{1}{2}(\mathbf{x}_r + \mathbf{x}_s) - \mathbf{x}_0$ is midpoint displacement. t_0 is two-way traveltime at the central midpoint $\mathbf{x}_0$, $\mathbf{p}$ stands for the central horizontal slowness, and the 2×2 second-derivatives matrices of the NIP- and N-wave traveltime with respect to the surface Cartesian coordinates are denoted as $\hat{M}_{NIP}$ and $\hat{M}_N$. Since a matrix of second-derivatives and the wavefront curvature matrix are related, we denote them as wavefront curvature matrices. we also refer to Vanelle et al. (2018) for read up about a transformation to main curvatures from the second-order traveltime derivatives in the general 3D anisotropic case.

In the case of a point diffraction, fronts of the NIP- and N-waves fully coincide, and, therefore matrix $\hat{M}_{NIP}$ and matrix $\hat{M}_N$ are equal componentwise. Further, we will formulate a similar criterion relating $\hat{M}_{NIP}$ and $\hat{M}_N$ in the case of an edge diffraction. We first assume an isotropic medium. Due to Fermat's principle (see e.g., law of edge diffraction in Keller, 1962), a zero-offset ray is orthogonal to the edge. Since the incident and diffracted rays are the same, the diffraction cone degenerates to a plane that is orthogonal to the edge. Moreover, kinematics of edge diffraction is determined only by the edge as a space curve and is not influenced by the interfaces. When we place a point source at the normal-incidence-point on the edge (see Figure 4.3), it triggers the NIP-wave. Due to Fermat's principle and reciprocity of the diffraction point, the NIP-wave theorem Hubral (1983) is also valid for an edge and assures that a small-offset experiment provides the NIP-front curvature. When we explode an edge segment as a whole, the N-wave is induced. Since zero-offset rays are orthogonal to the edge, N-wave corresponds to the zero-offset experiment. The initial wavefront of the N-wave is locally a cylinder whereas the wavefront of the NIP-wave is spherical. The cylinder and the sphere, however, has a common circle. These two waves include the same rays, which start from the normal-incidence-point orthogonal to the edge. This common (one-parameter) family of rays includes the zero-offset ray as well. All they spotlight a curve at the acquisition surface. We call this curve a focusing curve because rays backpropagated from such a curve focus at one particular point on the edge (Figure 4.3). The central midpoints, which take place on the focusing curve, correspond to the same normal-incidence-point. In the 2.5D model comprising a horizontal straight edge in the isotropic medium, which is invariant along the edge, the focusing curves are the straight lines on the surface orthogonal to the edge. The same applies for the inclined edge in isotropic homogeneous medium. In the case of curved edge in the homogeneous medium, the focusing curves are also straight lines but are rotated depending on the central midpoint location.

Further, we consider a naturally parameterized and regular focusing curve $x = x(s)$, $y = y(s)$ crossing the central midpoint at $s = s_0$: $x(s_0) = x_0, y(s_0) = y_0$ (see Figure 4.3). In Appendix B we show that for differentiable rays, a focusing curve is regular at a point if

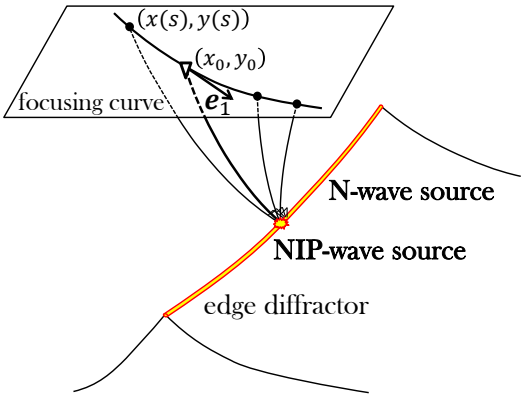

Figure 4.3: The family of rays common for the NIP- and the N-wave. The rays emerge from a normal-incidence-point ans stand orthogonal to the edge. They outline a curve at the acquisition surface. When propagated back to the the edge, the rays focus at the normal-incidence-point.

the NIP- and the N-wave have no caustics at this point. This is a natural assumption since we also assume finite experimental values for the matrix elements of $\hat{M}_{NIP}$ and $\hat{M}_N$. For the common rays, traveltimes are equal:

$$t_{NIP}(x(s), y(s)) = t_N(x(s), y(s)), \tag{4.2}$$

$$t_{NIP}(x_0, y_0) = t_N(x_0, y_0) = \frac{t_0}{2}. \tag{4.3}$$

Moreover, the slowness components are also equal:

$$\frac{\partial t_{NIP}}{\partial x}(x(s), y(s)) = \frac{\partial t_N}{\partial x}(x(s), y(s)), \tag{4.4}$$

$$\frac{\partial t_{NIP}}{\partial y}(x(s), y(s)) = \frac{\partial t_N}{\partial y}(x(s), y(s)), \tag{4.5}$$

$$\frac{\partial t_{NIP}}{\partial x}(x_0, y_0) = \frac{\partial t_N}{\partial x}(x_0, y_0) = p_x, \tag{4.6}$$

$$\frac{\partial t_{NIP}}{\partial y}(x_0, y_0) = \frac{\partial t_N}{\partial y}(x_0, y_0) = p_y. \tag{4.7}$$

Differentiating the identities (4.4, 4.5) along the focusing curve yields:

$$\frac{\partial^2 t_{NIP}}{\partial x^2}\dot{x} + \frac{\partial^2 t_{NIP}}{\partial y \partial x}\dot{y} = \frac{\partial^2 t_N}{\partial x^2}\dot{x} + \frac{\partial^2 t_N}{\partial y \partial x}\dot{y}, \tag{4.8}$$

$$\frac{\partial^2 t_{NIP}}{\partial x \partial y}\dot{x} + \frac{\partial^2 t_{NIP}}{\partial y^2}\dot{y} = \frac{\partial^2 t_N}{\partial x \partial y}\dot{x} + \frac{\partial^2 t_N}{\partial y^2}\dot{y}. \tag{4.9}$$

Now we consider a local Cartesian coordinate system satisfying $\dot{y}(s_0) = 0$ and $\dot{x}(s_0) = 1$. This is a coordinate system where the x-axis is tangent to the focusing curve at the central

midpoint location. Therefore, in this coordinate system the following holds:

$$\begin{aligned}
\frac{\partial^2 t_{NIP}}{\partial x^2}(x_0, y_0) &= \frac{\partial^2 t_N}{\partial x^2}(x_0, y_0)\,, \\
\frac{\partial^2 t_{NIP}}{\partial x \partial y}(x_0, y_0) &= \frac{\partial^2 t_N}{\partial x \partial y}(x_0, y_0)\,, \\
\frac{\partial^2 t_{NIP}}{\partial y^2}(x_0, y_0) &\neq \frac{\partial^2 t_N}{\partial y^2}(x_0, y_0).
\end{aligned} \tag{4.10}$$

The equations 4.10 imply that for any edge diffraction at each central midpoint location there exists an azimuth, for which the wavefront curvature matrices are equal componentwise with one exception: $\hat{M}^{NIP}_{xx} = \hat{M}^{N}_{xx}$, $\hat{M}^{NIP}_{xy} = \hat{M}^{N}_{xy}$, and $\hat{M}^{NIP}_{yy} \neq \hat{M}^{N}_{yy}$. In this direction the edge diffraction behaves locally as a 2D diffraction.

If we now compose a residual matrix $Res_M = \hat{M}_{NIP} - \hat{M}_N$, we see that the determinant $\det(Res_M)$ vanishes because the first columns in the matrix coincide. Since the determinant is a rotational invariant, this allows one to formulate a criterion for the edge diffraction identification for arbitrarily oriented global Cartesian coordinate system on the surface, i.e., for an arbitrary azimuth in the global surface-related Cartesian coordinates:

$$\det(\hat{M}_{NIP} - \hat{M}_N) = 0. \tag{4.11}$$

A similar derivation applies for anisotropy except a difference that the common family of rays is not orthogonal to the edge. It comprises rays with zero slowness component along the edge. The reader can consult Appendix A for an alternative derivation of the above equation (4.11), which is based on specific initial conditions for the dynamic ray tracing of the NIP- and the N-wave.

The result obtained in equation 4.11 is consistent with equations for geometrical spreading of reflections (see in Hubral, 1983). Accordingly, the zero-offset geometrical spreading can be expressed through the wavefront curvatures as:

$$\begin{aligned}
Q &= -\frac{1}{v}\frac{2}{M_{NIP} - M_N} && \text{in 2D}\,, \\
\det Q &= -\frac{1}{v^2}\frac{4}{\det(M_{NIP} - M_N)} && \text{in 3D}\,,
\end{aligned} \tag{4.12}$$

where Q or $\det Q$ stand for the geometrical spreading, and $M_{NIP} = P_{NIP}\,{Q_{NIP}}^{-1}$, $M_N = P_N\,{Q_N}^{-1}$ are corresponding dynamic ray tracing quantities (matrices) related to the wavefront curvatures (e.g., Červený, 2001). For detailed derivations of equation 4.12 the reader can consult Appendix C. To read up about relation between $M_{NIP} - M_N$ and $\hat{M}_{NIP} - \hat{M}_N$ see Appendix A.

Finally, we propose the following workflow for the identification of point, edge diffraction and reflection:

1. compute and store the residual matrix $\hat{M}_{NIP} - \hat{M}_N$ for each time sample at every central midpoint location;

2. compute $\det(\hat{M}_{NIP} - \hat{M}_N)$ for each sample;

3. isolate diffractions (point and edge) from reflections with the criterion that $\det(\hat{M}_{NIP} - \hat{M}_N)$ equals zero;

4. tag point and edge diffractions by inspecting the elements of the stored residual matrix. If the matrix element appears to be nonzero (with some threshold) for a sample, assign an edge diffraction tag to this sample, else assign a point diffraction tag to the sample.

The proposed workflow results in an edge or point diffraction binary mask, which can further be used for an event separation filter (Dell and Gajewski, 2011).

4.2.3 Focusing edge diffractions

Rays shot downward from the focusing curve, which we introduced in the previous sections, intersect at one point on the edge. This implies, focusing curves can be exploited to sort traces into groups which contain arrivals from the same location on the edge. Such groups can be used for an analysis of wavefront attributes, which are subsequently utilized in a ray focusing tomography similarly to point diffractions (see e.g., in Znak et al., 2019). We first assume that our seismic experiment (survey) is performed in a global surface-related coordinate system along a direction, which builds up an angle with Northing. The matrices of wavefront curvatures, $\hat{M}_{NIP}$ and $\hat{M}_N$, are determined in the global coordinate system. We seek for a rotation angle, which transforms the global coordinate to a local coordinate system, where the tensors of wavefront curvatures have equal columns. We abound all attempts to find a local coordinate system, where the matrices of the wavefront curvatures are equal elementwise:

$$R\,\hat{M}_{NIP}R^T \neq R\,\hat{M}_N R^T, \qquad R = \begin{pmatrix} \cos\varphi & \sin\varphi \\ -\sin\varphi & \cos\varphi \end{pmatrix}. \tag{4.13}$$

R is the rotation matrix and φ is the rotation angle. Instead, we search for a local coordinate system providing a coincidence of a column, e.g., the first one:

$$R\,\hat{M}_{NIP}R^T \begin{pmatrix} 1 \\ 0 \end{pmatrix} = R\,\hat{M}_N R^T \begin{pmatrix} 1 \\ 0 \end{pmatrix}. \tag{4.14}$$

Multiplying the transposed rotation matrix by the unit vector yields a vector equation

$$R\left(\hat{M}_{NIP} - \hat{M}_N\right)\begin{pmatrix} \cos\varphi \\ \sin\varphi \end{pmatrix} = 0 \tag{4.15}$$

or, equivalently, two scalar equations

$$\begin{aligned} \left(\cos\varphi\ \sin\varphi\right)\left(\hat{M}_{NIP} - \hat{M}_N\right)\begin{pmatrix} \cos\varphi \\ \sin\varphi \end{pmatrix} = 0, \\ \left(-\sin\varphi\ \cos\varphi\right)\left(\hat{M}_{NIP} - \hat{M}_N\right)\begin{pmatrix} \cos\varphi \\ \sin\varphi \end{pmatrix} = 0. \end{aligned} \tag{4.16}$$

The unit vectors represents the basis vectors of the rotated coordinate system. In other words, there exists a local coordinate system with horizontal basis vectors $\mathbf{e}_I$ and $\mathbf{e}_{II}$ such

that:

$$\begin{aligned}\left(\mathbf{e}_I, \left(\hat{M}_{NIP} - \hat{M}_N\right) \mathbf{e}_I\right) = 0,\\ \left(\mathbf{e}_{II}, \left(\hat{M}_{NIP} - \hat{M}_N\right) \mathbf{e}_I\right) = 0.\end{aligned} \tag{4.17}$$

If both basis projections of a vector are zeros, the vector is a null vector itself:

$$(\hat{M}_{NIP} - \hat{M}_N)\, \mathbf{e}_I = 0. \tag{4.18}$$

The above equation 4.18 represents a homogeneous linear system with respect to the components of a unit vector that is tangent to the focusing curve. The linear system has a non-trivial solution that is in correspondence with the condition of the edge diffraction (Eq. 4.11). Solving equation 4.18 for different central midpoints yields a unit vector field, which is tangent to a set of focusing curves. These curves subsequently build integral curves of the vector field.

As previously shown, if a diagonal element of the residual matrix vanishes, then the symmetrical elements on the adjacent diagonals also vanish to preserve the zero equality of the determinant. Vice versa, if the elements on the adjacent diagonals vanish, then there has to be one and only one element on the primary diagonal that also vanishes. These are two cases when the focusing curve is tangent to the basis vectors of the global Cartesian coordinates. Otherwise, all elements of the residual matrix are nonzero. To prevent numerical instabilities due to division by zero in case if elements of the residual matrix become very small number, we suggest to use the row of the residual matrix that has the largest norm when computing the tangent vector. Within this row, we suggest a division by an element with the larger modulus.

We formulated a procedure for kinematic ray focusing of edge diffraction. However, for the edge diffraction as well as for the point diffraction, geometrical spreading of both NIP-wave and N-wave vanishes when we back-propagate the waves till the one-way traveltime expires (see Appendix A for more details). This corresponds to the fact that a ray tube, when propagated back, collapses to the point source or the line source, respectively. For dynamic ray focusing of edge diffraction this implies that not only $\hat{M}_{NIP}$ but also $\hat{M}_N$ wavefront curvatures can potentially be utilized in a focusing-based tomography, i.e. velocity model building, by minimizing the backpropagated geometrical spreading Znak et al. (2019).

4.3 Numerical tests

In this section, we demonstrate the proposed approach for identification of seismic events and focusing the edge diffractions on two simple synthetic data examples. We consider a heterogeneous isotropic and a homogeneous anisotropic VTI model. We show that the determinant of the residual matrix vanishes for both isotropic and anisotropic media. We further show how to build the focusing curves for isotropic and anisotropic media and also discuss the different mechanisms of the bending the focusing curves in these media. Both models includes an edge diffractor with the lateral extension of 1 km in Y-direction.

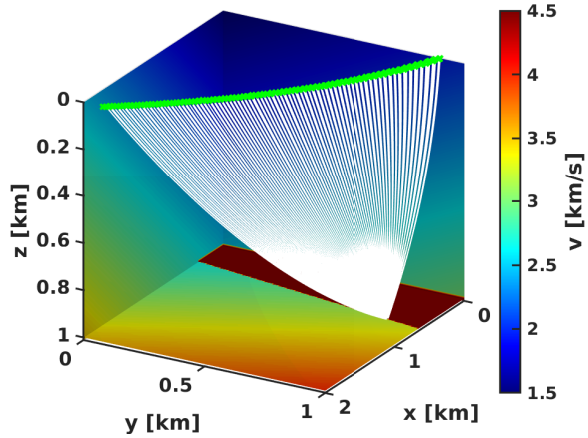

Figure 4.4: The lateral inhomogeneous isotropic velocity model. The velocity gradient is function of all three coordinates, x, y, and z. The figure also displays rays (white lines) traced down to a focusing point. The horizontal slowness and zero-offset traveltime determined in the vicinity of the focusing curve (green line) allow for the kinematic focusing at the specific point on the edge.

4.3.1 Linear diffractor in a heterogeneous isotropic medium

The heterogeneous isotropic medium represents a 3D gradient-velocity model with a straight edge that is slightly rotated in the horizontal plane (Figure 4.4). We first compute the traveltimes of edge diffractions by eikonal solver and subsequently the wavefront attributes by finite differences. The elements of the wavefront-curvature matrices are displayed as functions of the central midpoint location in Figures 4.5 and 4.6. We observe, the difference between the xx-element of the $\hat{M}_{NIP}$ matrix (Figure 4.5a) and the xx-element of the $\hat{M}_N$ matrix (Figure 4.6a) is not as prominent as for xy- and yy-elements because the model is still close to the symmetric one, i.e., the 2D criterion is fulfilled in the direction orthogonal to the edge. In the correspondence with equation (4.11), the values of the residual determinant are relatively small as shown in Figure 4.7. We explain non-zero values by numerical errors during computing two-way traveltimes and second-order derivatives and a potential loss of significance when two nearly equal small numbers are subtracted.

The matrix elements displayed in Figures 4.5 and 4.6 are used to solve the residual system of algebraic equations (4.18) for every central midpoint location. This results in the unit-length vector field on the acquisition surface as shown in Figure 4.8. The unit-length vector field is tangent to the set of the focusing curves. For illustration, we compute one of the possible focusing curves continuing it as an integral curve starting from a point at the boundary. Finally, we determine the traveltimes and the horizontal components of slowness in the vicinity of the focusing curve (Figure 4.8) and use them as initial values to trace rays downwards. The resulting rays focus precisely at the edge as demonstrated in Figure 4.4.

4.3.2 Linear diffractor in an anisotropic medium

As anisotropic media, we consider a homogeneous vertical transversely isotropic (VTI) model with Thomsen's parameters $v_{P0} = 2.2$ km/s, $v_{S0} = 0.8$ km/s, $\varepsilon = 0.2$, and $\delta = -0.2$. The geometry of the edge is illustrated in Figure 4.9. The edge is inclined comparing to

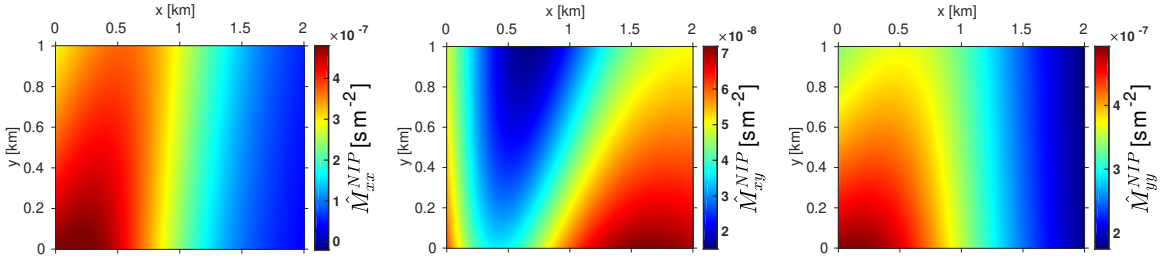

Figure 4.5: Figure displays the elements of the curvature matrix of NIP-wave wavefront as function of midpoint displacements to the central midpoint location. The velocity model is laterally inhomogeneous as shown in Figure 4.4.

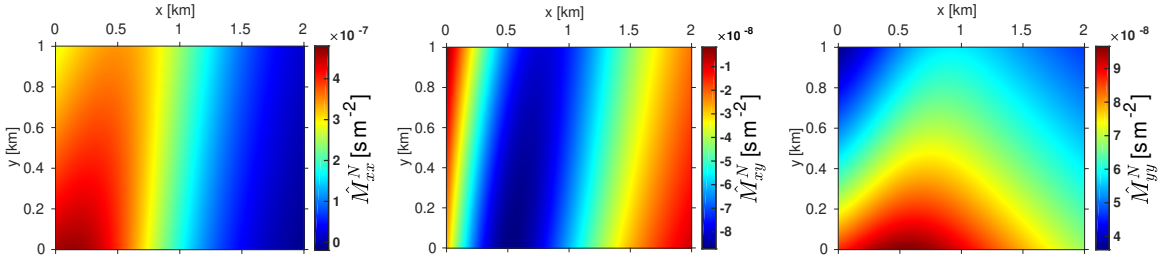

Figure 4.6: Figure displays the elements of curvature matrix of the N-wave wavefront as function of midpoint displacements to the central midpoint location. The velocity model is laterally inhomogeneous as shown in Figure 4.4.

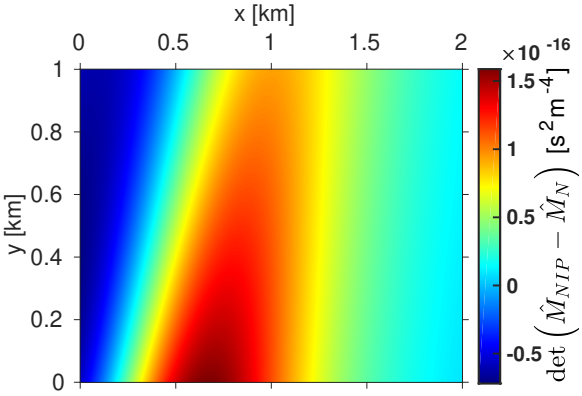

Figure 4.7: Figure shows the determinant of the residual matrix, $\hat{M}_{NIP} - \hat{M}_N$, as a function of the central midpoint location. It vanishes in the case of edge diffraction. The velocity model is laterally inhomogeneous as shown in Figure 4.4.

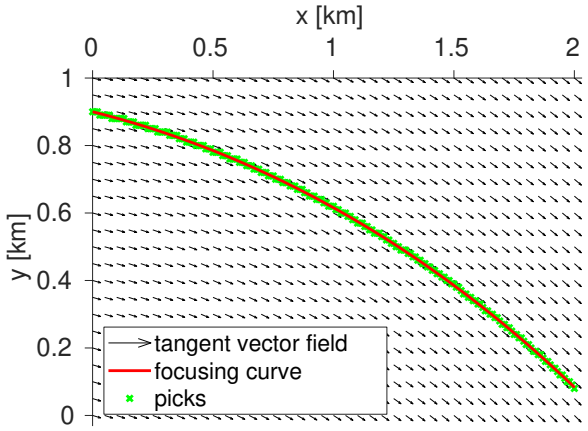

Figure 4.8: Figure displays the focusing curve and the tangent vector field. The unit vector field is tangent to the family of focusing curves and is computed by solving the homogeneous system of algebraic equations for the residual matrix $\hat{M}_{NIP} - \hat{M}_N$. The focusing curve is obtained as an integral curve of this vector field. The attributes for focusing (see Figure 4.4) are determined in the vicinity of this focusing curve.

the isotropic model. For an horizontal edge the focusing curves would appear as straight lines due to the anisotropic symmetry while for the inclined edge the focusing curves will bend as shown in Figure 4.9. The same bending effect is achieved by considering a tilted transversely isotropic medium with a horizontal edge. We compute the traveltimes by eikonal solver and calculate the wavefront attributes by the finite differences. Elements of matrices of the wavefront curvature are shown in Figures 4.10 and 4.11 as function of the midpoint displacements. We again observe that the difference between the xx-element of the $\hat{M}_{NIP}$ matrix and the xx-element of the $\hat{M}_N$ matrix for each central midpoint is smaller than for other elements. We explain it by the fact that the model is still close to the symmetric one with horizontal edge. The determinant of the residual matrix vanishes for every central midpoint as shown in Figure 4.12.

The tangent vector field (Figure 4.13 is obtained by solving the residual system of algebraic equations (4.18) with the matrix elements shown in Figures 4.10 and 4.11. For comparison, we build the focusing curves starting from the same point at the boundary as in the isotropic case (see Figures 4.8 and 4.13). In the specific anisotropic case, it appears to be less smooth. Traveltimes and the horizontal components of slowness, which we again determine in the vicinity of the focusing curve (Figure 4.13), are used to trace rays reversely in time. We again observe a perfect focusing of rays at the single point on the edge as illustrated in Figure 4.9. This confirms the stability and feasibility of the proposed trace sorting into focusing groups.

4.3.3 Edge diffraction identification in the SEG/EAGE salt model

We used SEG C3 NA Narrow Azimuth dataset to test our approach on a complex synthetic data. The SEG/EAGE Salt model is a 3-D geological model that was created as part of a multi-phase collaboration between the SEG and EAGE, with funding from the U.S. Department of Energy National Laboratories, as well as several institutions from in-

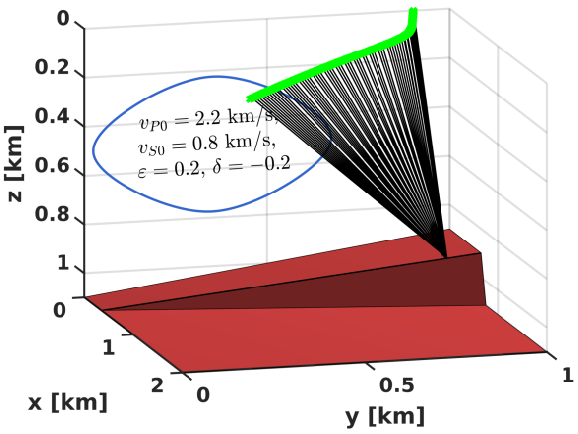

Figure 4.9: Anisotropic VTI model. Thomsen's parameters are $v_{P0} = 2.2$ km/s, $v_{S0} = 0.8$ km/s, $\varepsilon = 0.2$, and $\delta = -0.2$. The figure also displays rays (black lines) traced down to a focusing point. The horizontal slowness and zero-offset traveltime determined in the vicinity of the focusing curve (green line) allow for the kinematic focusing at the specific point on the edge.

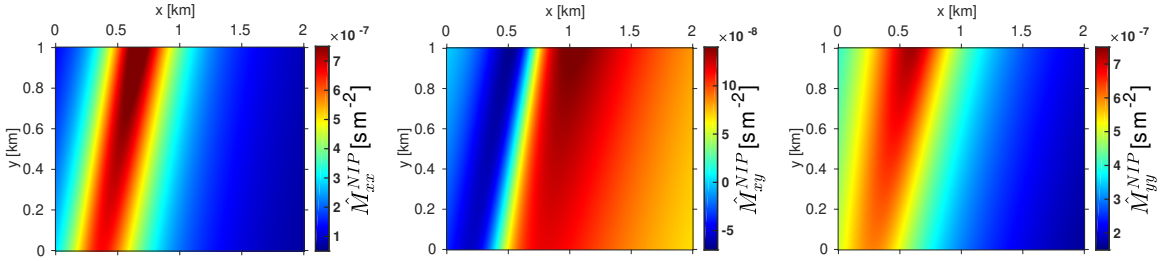

Figure 4.10: Figure displays the elements of curvature matrix of the NIP-wave wavefront as function of midpoint displacements to the central midpoint location. The velocity model is VTI model as shown in Figure 4.9.

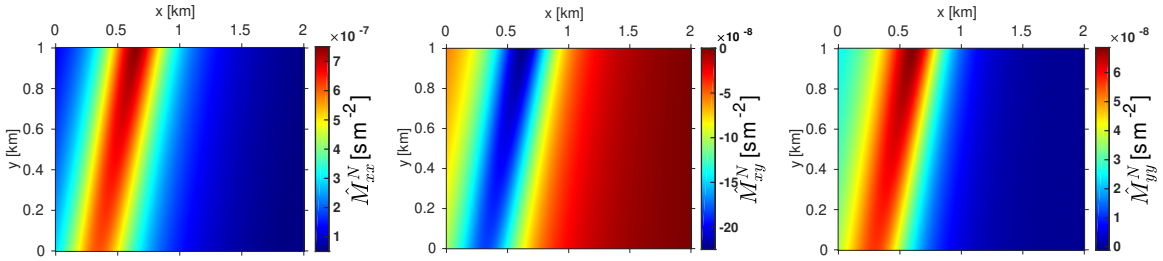

Figure 4.11: Figure displays the elements of curvature matrix of the N-wave wavefront as function of midpoint displacements to the central midpoint location. The velocity model is VTI model as shown in Figure 4.9.

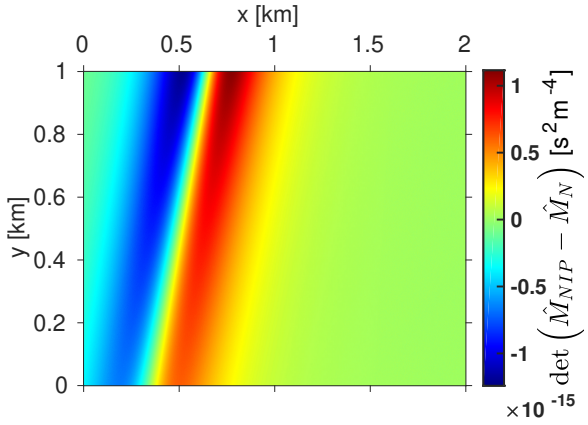

Figure 4.12: Figure shows the determinant of the residual matrix, $\hat{M}_{NIP} - \hat{M}_N$, as a function of the central midpoint location. It vanishes in the case of edge diffraction also for the VTI model (Figure 4.9).

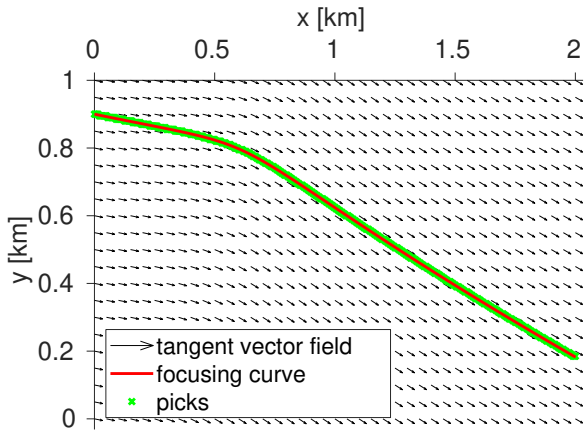

Figure 4.13: Figure displays the focusing curve and the tangent vector field for VTI model. The tangent field is computed by solving the homogeneous system of algebraic equations for the residual matrix $\hat{M}_{NIP} - \hat{M}_N$ as in the isotropic case. The focusing curve is obtained as an integral curve of this vector field. The attributes for focusing (see Figure 4.9) are determined in the vicinity of this focusing curve.

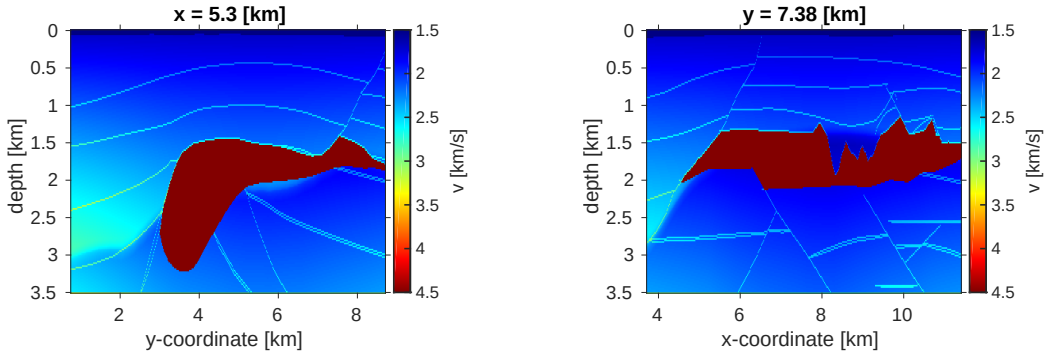

Figure 4.14: Figure displays the x- and y-profiles of the SEG/EAGE velocity model. The corresponding acquisition lines are depicted in Figure 4.15 using dash lines.

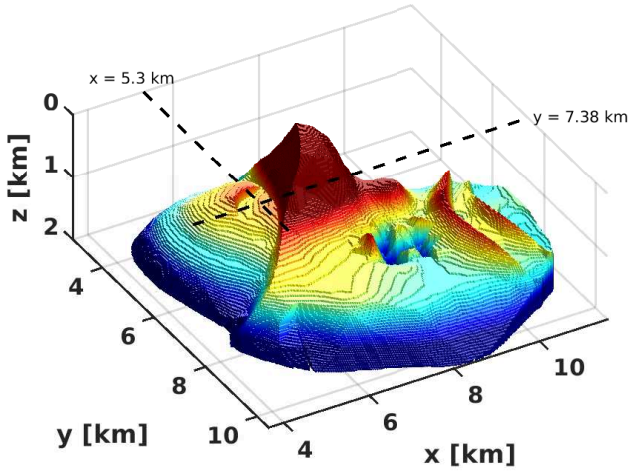

Figure 4.15: Topography of the salt body with pronounced edge diffractors. Dash lines illustrate the x- and y-profiles that we picked for the edge diffraction identification.

dustry and academia (Aminzadeh et al., 1994, 1996). Figure 4.14 show two 2D sections, further called as x- and a y-profile, used to test the diffraction identification. The dataset consists of 51 "sail" lines, separated by 320 m: 96 shots per line, 80 m shot interval 8 cables per shot, 40 m cable separation 68 receivers per cable, 20 m receiver separation Source between first receiver on cables 4 and 5. The narrow acquisition mimics a vessel moving along the y-coordinate. We also added Gaussian noise with s/n=1 and applied simultaneous 8-parameter search based on differential evolution optimization (Walda et al., 2017). In order to enhance stacked waveforms and wavefront attributes of relatively weak diffractions, we account for the conflicting dips in the CRS stacking (Walda and Gajewski, 2017). This means that the global multidimensional search domain is divided into shorter search intervals according a partition of the slowness vector components.

Both x- and y-profile are also displayed in Figure 4.15 as dashed line. We observe the profiles cut a very pronounce edge of the salt diapir, which causes a richness of diffractions in the corresponding inline and crossline sections in seismic data.

Figures 4.16 and 4.17 show the determinant of the residual matrix and the corresponding stacked sections for several ranges of the slowness vector components. The sections in Figure 4.16 displays y-profile (see Figure 4.15). Respectively, figure 4.17 illustrates the section related to x-profile. Vanishing determinant of residual matrix for some prominent edge diffractions is marked by red arrows. For consistency and a better visualisation, the same prominent edge diffractions are marked with red arrows in the stacked sections. We observe that the determinant criterion works and highlights many diffraction events. For instance, we clearly identify two diffractions in Figure 4.16, the top raw. Comparing with Figure 4.14, we conclude that they resulted from the edge of the salt diapir (the right one) and from the edge formed by the sediments at the salt bottom (the left one). The diffraction by the edge of the salt mountain is also present for other dips (Figures 4.16, the middle and bottom raw). It is also clearly tracked in y-profiles (follow the upper red arrow in Figure 4.17). The tail of the second one is also observed in 4.17, top raw. The upper strongly highlighted event in Figure 4.16, the bottom raw, is a diffraction tail from the junction zone of the salt surface with the third reflecting boundary (Figure 4.14).

The right part of the y-profile is strongly heterogeneous, not only due to presence of many peculiarities in the salt topography, but also because of strongly irregular mesh of the reflecting boundaries above the salt. Therefore, it is a zone of strong wave interference, where wavefront attribute determination and, therefore, seismic event identification is challenging. However, we observe two bright spots slightly on left from this complicated zone, above the deepening of the salt surface (Figure 4.17, the bottom row).

4.4 Discussion

In the presented approach we assume that the edge diffraction response is registered everywhere on the acquisition surface though for small-offsets. We also consider the kinematic characteristics of the edge response only. This implies we ignore such factors as phase, amplitude decay, and diffractor radiation pattern. The dynamic characteristics are crucial in the vicinity of zones of evanescence of the edge diffraction (Klem-Musatov et al., 2008) and might affect extraction of the wavefront attributes.

We have discussed a possibility to use $\hat{M}_N$ wavefront curvatures extracted from the edge diffractions for velocity model building. Similarly to minimizing the backpropagated geometrical spreading of the NIP-wave, we can minimize geometrical spreading of the N-wave. However, initial conditions for dynamic ray tracing, which are required for forward modeling of the N-wave, are different from those for the NIP-wave. In the case of a curved edge, they also contain curvature and torsion of the edge as a space curve as discussed in Appendix A. This is especially important in the case of limited-offset acquisition such as p-Cable streamer or ground penetrating radar. Missing zero source-receiver offsets complicate applying NIP-wave tomography as it requires to separate edge diffraction from point diffractions. On the contrary, the available slope and M_N curvature information can safely be utilized in the dynamic ray focusing irrespective of type of diffraction.

Dell et al. (2018) separated edge diffractions using the property of the edge diffraction response to align along a particular azimuth within the Kirchhoff migration operator. The corresponding azimuth direction gives the most contribution to the Kirchhoff integral being the line where the zero-offset traveltime is tangent to the doubled point source traveltime.

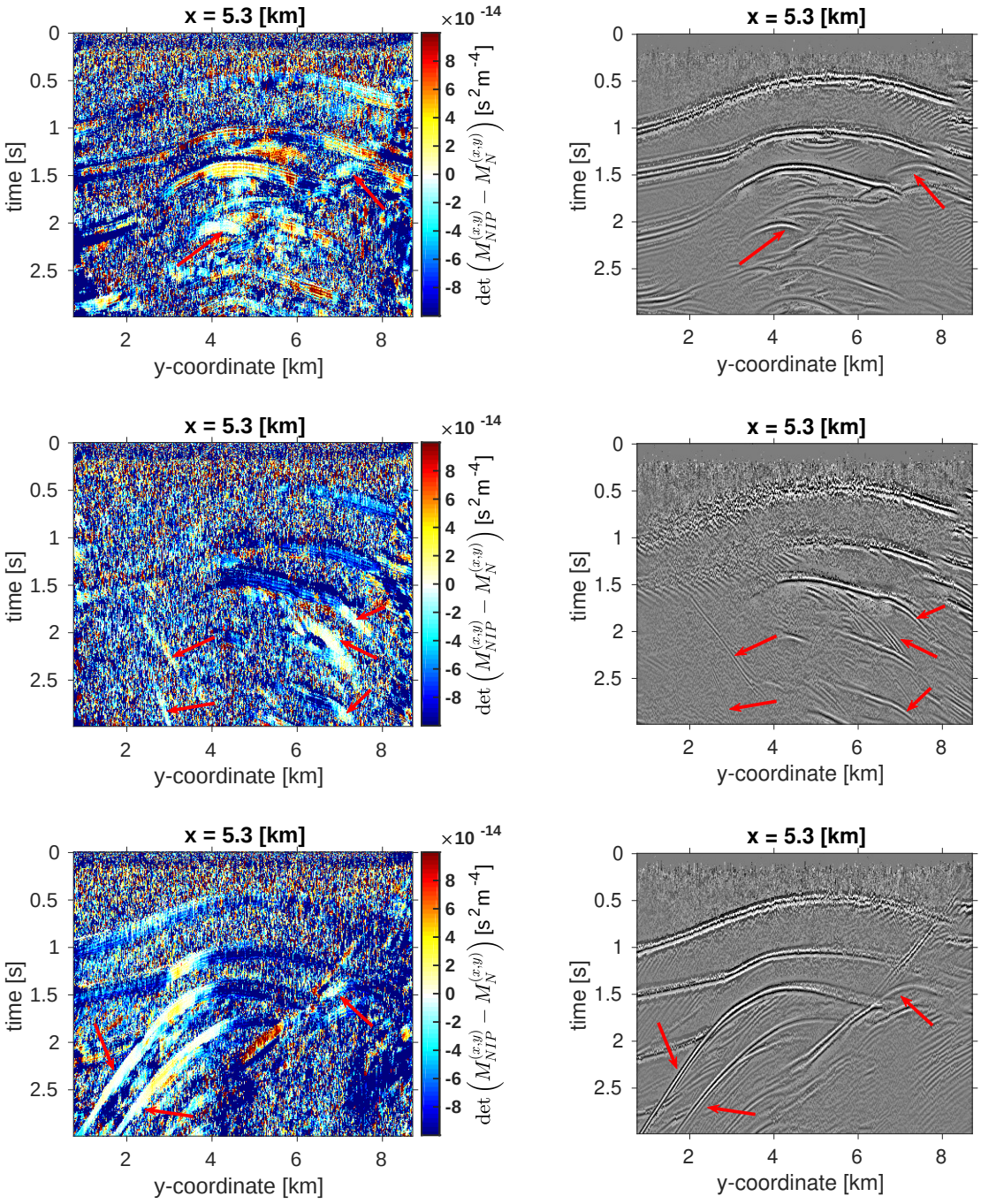

Figure 4.16: Determinant of the residual matrix and stacked section for the x-profile (Figures 4.14, 4.15) of the SEG/EAGE salt model. The slowness search intervals are: $p_x \in [-12, -3] \cdot 10^{-4}$ s/m, $p_y \in [-1, 1] \cdot 10^{-4}$ s/m for the top row, $p_x \in [-12, -3] \cdot 10^{-4}$ s/m $p_y \in [3, 12] \cdot 10^{-4}$ s/m for the middle row, and $p_x \in [-3, -1] \cdot 10^{-4}$ s/m, $p_y \in [-12, -3] \cdot 10^{-4}$ s/m for the bottom row.

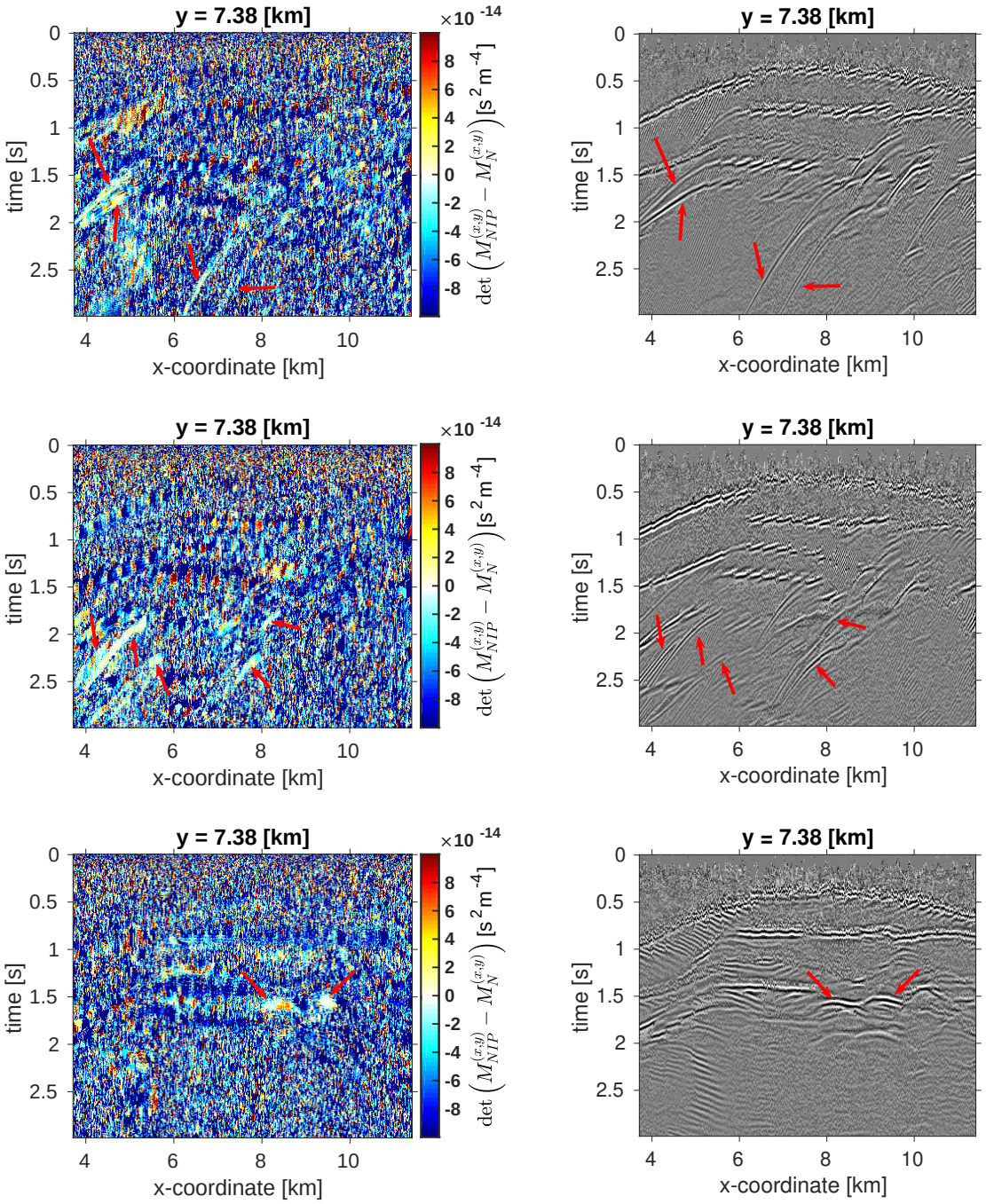

Figure 4.17: Determinant of the residual matrix and stacked section for the y-profile (Figures 4.14, 4.15) of the SEG/EAGE salt model. The slowness search intervals are: $p_x \in [-3,-1]\cdot 10^{-4}$ s/m, $p_y \in [-3,-1]\cdot 10^{-4}$ s/m for the top row, $p_x \in [1,3]\cdot 10^{-4}$ s/m, $p_y \in [3,12]\cdot 10^{-4}$ s/m for the middle row, and $p_x \in [-1,1]\cdot 10^{-4}$ s/m, $p_y \in [-12,-3]\cdot 10^{-4}$ s/m for the bottom row.

Therefore, it is precisely the focusing curve discussed in the above sections. We provided an algorithm to build the focusing curves by means of wavefront attributes. This allows for a diffraction separation based on a wavefront-attribute filter during Kirchhoff migration, i.e., directly in the image domain (time or depth).

4.5 Conclusions

We proposed a novel method for separation and identification of the diffraction response in the data domain. The method is generalized to an arbitrarily oriented and curved edge in 3D heterogeneous media, including anisotropy, and allows one to distinguish seismic events between point diffraction, edge diffraction, and reflection. We exploited the fact that for an edge diffraction there is an acquisition line in a 3D survey where 3D edge-diffraction response kinematically behaves as a 2D diffraction, but locally and in a specific direction, which changes from point to point. We constructed the tangent vector field of such directions by solving a system of homogeneous algebraic equations with so-called residual matrix. The residual matrix contains residuals of the wavefront curvature matrices of the second-order derivatives of NIP- and N-wave. The identification criterion utilizes the determinant of the residual matrix, which vanishes for diffractions, and inspecting the columns of the residual matrix, which are zeros for point diffraction and non-zeros for edge diffraction.

We also provided an algorithm based on the NIP- and N-wave curvature matrices to build the focusing curves on the acquisition surface. The rays propagated downward from a focusing curve focus at a particular point on the edge which allows one to sort traces into specific groups. We showed that NIP-wave and N-wave geometrical spreading estimated for these group vanishes exactly at the edge when we propagate the waves downwards. This implies that the 3D edge diffraction response can kinematically and dynamically be focused to a point similarly to a point diffraction.

The proposed algorithm was applied to synthetic examples comprising isotropic heterogeneous and anisotropic model. Matrices of curvatures of NIP-wave and N-wave were first estimated by a multidimensional multiparameter stacking and then used to solve the residual system of algebraic equations for every central midpoint location. The obtained unit-length vector field was used to compute the set of the focusing curves. For the anisotropic model, it appeared to be less smooth than for an isotropic model. Traveltimes and the horizontal components of slowness determined in the vicinity of the focusing curve were used to trace rays reversely in time. We observed a perfect focusing of rays at the single point on the edge for both isotropic and anisotropic model.

Acknowledgments

The authors thank sponsors of the Wave Inversion Technology (WIT) Consortium and the Federal Ministry for Economic Affairs and Energy of Germany (project number 03SX427B).

5 Polarization-consistent stacking of multicomponent seismic data

Abstract

Offshore subsurface imaging of data acquired on the seafloor has been very successful. This kind of acquisition naturally provides wide-azimuth data and does not have limitations due to the streamer length or obstructions, such as production platforms. However, the seafloor acquisition usually has a coarser receiver grid, which requires a trace interpolation algorithm to avoid acquisition footprint in migration sections. Also onshore subsurface imaging of land data strongly depends on the signal-to-noise ratio in the recorded data. Both imaging methods benefit from the knowledge of kinematics, polarization, and wave mode velocities at the acquisition line. This all motivates us to investigate a multicomponent data preconditioning approach based on wavefront attributes. They are normally obtained from the prestack data by a multidimensional and -parameter stacking technique, e.g., common-reflection-surface (CRS) method. In the conventional CRS method the attributes are extracted by an amplitude-coherency analysis of the vertical component. However, all components of elastic wavefield are often recorded during the seafloor and land surveys. To fully exploit this data redundancy, we generalize the conventional CRS method to the multicomponent case using a local polarization approach. The multicomponent CRS method exploits a semblance optimization where weighted components are summed up along the traveltime surface defined with the wavefront attributes. The component weights are determined with polarization vector. The proposed approach not only results in enhancing the data with a more physically accurate stacking, but it also enables us to automatically pick polarization and polarization derivatives in offset and midpoint directions. To interpret these quantities, we provide a proof of the NIP-wave theorem formulated for the polarizations. In addition, the attributes of the multicomponent CRS allow for the identification of P- and S-waves and a retrieval of compressional and shear velocities at the acquisition line. The presented method was successfully applied to synthetic data.

5.1 Introduction

Utilizing the complete vector field of the emerging seismic wave is necessary for a physically accurate processing of data recorded onshore or on the ocean bottom. The multicomponent data can be incorporated into a variety of processing, imaging, and inversion tools: wavefield decomposition (Amundsen and Reitan, 1995; Schalkwijk et al., 2003), surface waves suppression (Shieh and Herrmann, 1990) and inversion (Ikeda et al., 2014), various elastic migration (e.g., Kuo and Dai, 1984; Chang and McMechan, 1994; Zhe and Greenhalgh, 1997; Hokstad, 2000; Feng and Schuster, 2017; Yang et al., 2018), microseismic-event localization (Gajewski and Tessmer, 2005), or elastic full-waveform inversion (Sears et al.,

2008; Brossier et al., 2009; Prieux et al., 2013). Additionally, a multicomponent approach is natural for describing different wave modes, which is crucial for interpretation of rock properties (Tatham et al., 1991). For example, the analysis of shear-wave splitting provides information about seismic anisotropy caused by particular orientation of fractures in rocks (Crampin, 1985; Martin and Davis, 1987). Also shear-waves are less affected by propagating through gas-saturated media than pressure-waves due to a minor effect of gas on the shear modulus (Granli et al., 1999). This allows an improved reservoir monitoring in areas where gas is present. However, multicomponent methods also face common problems of the single-component ones. The seafloor acquisition usually has a coarser receiver grid and requires trace interpolation algorithms to avoid acquisition footprint in migrated sections. Onshore subsurface imaging strongly depends on the noise level of the recorded data. Therefore, multicomponent data processing also benefits from preconditioning, i.e., trace regularization and signal-to-noise ratio (S/N) enhancement.

We investigate an approach to enhance multicomponent data with wavefront attributes. They are obtained by an application of the common-reflection-surface (CRS) stack to prestack data. This method is a multidimensional extension of the conventional common-midpoint (CMP) stack. CRS involves traces from adjacent midpoint locations, i.e., it is mutually applied in the midpoint-offset domain. Stacking more coherent data this way results in an improved S/N. Depending on a paraxial traveltime approximation, we can roughly divide CRS methods into multifocusing (Landa et al., 2010), hyperbolic CRS (Jäger et al., 2001), non-hyperbolic CRS (Fomel and Kazinnik, 2013), and implicit CRS (Schwarz et al., 2014). For a reader interested in a detailed comparison of these approaches, we refer to Walda et al. (2017). Wavefront attributes parametrize the CRS traveltime approximation and have a distinct physical meaning in terms of slope and curvatures of two hypothetical wavefronts, normal wave (N-wave) and normal-incidence-point wave (NIP-wave) (Hubral and Krey, 1980). They have been widely used in the applications, among others calculation of geometrical spreading (Hubral, 1983), velocity model building (Duveneck, 2004; Bauer et al., 2017), data preconditioning (Baykulov and Gajewski, 2009), and diffraction separation (Dell and Gajewski, 2011). Zhang et al. (2001) generalized the conventional CRS method to finite offsets, which allowed for a processing of the converted waves (Bergler et al., 2002). Recently, Bloot et al. (2018) suggested a CRS approximation for weakly anisotropic VTI media with larger (non-hyperbolic) offsets and Vanelle et al. (2018) yielded an interpreting of the hyperbolic CRS parameters for general anisotropic media.

Generally, the benefit of including polarization into seismic processing has been long recognized as discussed by Perelberg and Hornbostel (1994). Various approaches to determine polarization are reported in the literature, e.g., principal component analysis (Jurkevics, 1988; de Franco and Musacchio, 2001), complex analytic signals (Rene et al., 1986; Morozov and Smithson, 1996), or time-frequency transforms (Pinnegar, 2006). Gal'perin (1984) proposed to extend polarization analysis from single stations to the continuous seismic array. We follow this concept and apply it for stacking in the midpoint-offset domain.

In this paper, we formulate the CRS method for multicomponent seismic data and discuss its applications. We simultaneously stack different wavefield components over the common-reflection-surface. The contribution of a single component is controlled with an approximation for the alternating polarization vector. Here, we refer to polarization of bulk waves in a sense of the zero-order ray theory assuming only linearly polarized events. Parameters of the approximation are automatically picked during a semblance analysis, which

is similar to extracting the wavefront attributes by the conventional CRS workflow. They are polarization angle, polarization angle derivative with respect to the midpoint coordinate, and polarization angle derivative with respect to the half-offset. To interpret these new attributes in terms of N- and NIP-waves we formulate and prove the NIP-wave theorem for polarizations: for zero offset the derivative of the reflected-wave polarization vector with respect to the half-offset coincides with the spatial derivative of the NIP-wave polarization vector.

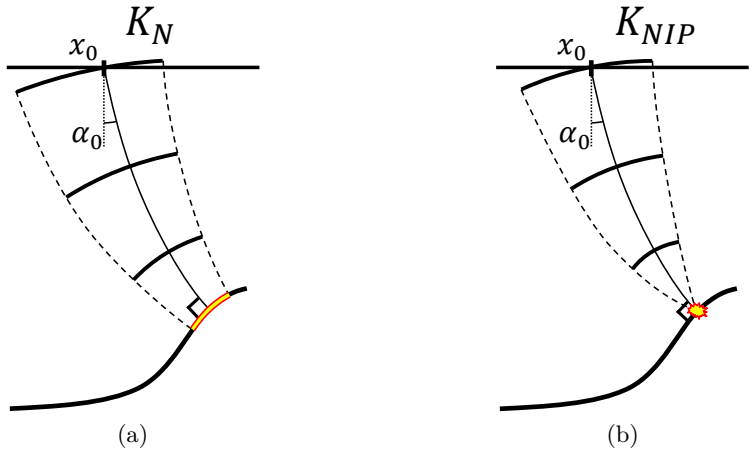

Figure 5.1: Hypothetical N- and NIP-wave. Normal wave (a) is triggered by an exploding reflector element. The corresponding rays are normal to the reflector, which gives the wave its name. NIP-wave (b) is a wave excited by a point source placed at the normal-incidence-point (NIP) on the reflector. The wavefront attributes are measured at the central midpoint with coordinate x_0.

Interpreting the wavefront attributes requires knowledge of the velocity model at the acquisition line. However, in the proposed multicomponent CRS approach there is no such requirement. The compressional- and shear-wave velocities and corresponding slowness vectors are fully determined with the wavefront and polarization attributes. Moreover, these data-driven values represent a priori information useful for constraining depth velocity model building algorithms. The surface-velocities inversion carried out by utilizing slowness and polarization attributes is actually an application of the slowness-polarization method (Dewangan and Grechka, 2003; Tsvankin and Grechka, 2011), which was originally formulated for estimating local anisotropy in a borehole by the vertical seismic profile (VSP) method.

Additionally, the polarization attributes allow to identify and subsequently separate P- and S-waves. This yields P-only and S-only stacked sections and P-only and S-only attributes. P- and S-waves filtering using slopes and polarization was suggested by Bergler et al. (2002) to separate arrivals after the converted-waves CRS stacking. They obtain the polarization angle from independently stacked single components and combine the slowness attribute with the angle subject to specified near-surface propagation velocities. Generally speaking, methods of separating wave modes have been comprehensively discussed in the literature. Dankbaar (1985) devised filtering in f-k domain by considering the P- and S-waves receiving characteristics. The method inherently accounts for the free-surface ef-

fect, but requires homogeneous velocities at the acquisition line to be known. Foster and Gaiser (1986) introduced a slant stack with rotation of multicomponent VSP data. The rotation operator, however, also needs velocities along the well. This method was improved by Greenhalgh et al. (1990). They accounted for P- and S-wave crosstalks and free-surface mode conversion. An alternative τ-p domain approach with mode conversion was introduced by Wang et al. (2002) for both free surface and seabed interfaces.

The paper is organized as follows. In the methodology section, we first briefly review the conventional CRS method. Then we introduce the concept of polarization-consistent stacking. Subsequently we discuss a notion of polarization vector on the common-reflection-surface as a function of the half-offset and the midpoint displacement, its possible approximations, and the interpretation of its derivatives. We also provide a simple attributes-based algorithm to separate P- and S-waves and build surface-velocities. In the appendix, we derive equations for the polarization vector derivatives. We end up the paper by demonstrating an application of the presented method to a 2D synthetic data example.

5.2 Common-reflection-surface method

The basic idea of the common-reflection-surface (CRS) method (Jäger et al., 2001) is to stack mutually in two dimensions, midpoint displacement, $\triangle x_m$, and half-offset, h:

$$\triangle x_m = x_m - x_0, \quad x_m = \frac{x_r + x_s}{2}, \quad h = \frac{x_r - x_s}{2}, \tag{5.1}$$

where x_r and x_s are receiver and source coordinates, and x_0 is a coordinate of a central midpoint. This extension of the common-midpoint (CMP) stacking (Mayne, 1962), where the data summation is performed only in one, half-offset, direction, allows to incorporate more coherent traces and, consequently, further enhance the seismic data.

In this section, we describe the CRS traveltime by a hyperbolic approximation. However, all paraxial traveltime approximations, which have been reported in the literature, can be formulated in terms of the same parameters (Walda et al., 2017) and utilized for the polarization-consistent stacking. Being a squared second-order Taylor expansion of reflected-wave traveltimes, the hyperbolic one has the simplest form among other widely used approaches:

$$t^2(x_0, \triangle x_m, h) = (t_0 + 2p_x \triangle x_m)^2 + 2t_0\Big(\hat{M}_N \triangle x_m^2 + \hat{M}_{NIP} h^2\Big). \tag{5.2}$$

t_0 is two-way central midpoint traveltime. Patameters of CRS approximation are called wavefront attributes. There are three of them in the 2D case. The zero-offset ray emerging at the central midpoint location has a value of horizontal slowness. This value, denoted by p_x, is the first wavefront attribute. The remaining attributes, $\hat{M}_N$ and $\hat{M}_{NIP}$, describe two fictitious wavefronts (Fig. 5.1). So $\hat{M}_N$ is related to the wavefront curvature of a normal wave triggered by an exploding reflector element (N-wave). This wave is called the normal wave (Hubral, 1983) as the corresponding rays are all normal to the reflector. The attribute $\hat{M}_{NIP}$ is related to the wavefront curvature of the wave caused by a point source at the normal-incidence-point (NIP) on the reflector (NIP-wave). The curvatures are assumed to be measured at the central midpoint location. In terms of traveltimes of the hypothetical

waves, the wavefront attributes represent derivatives with respect to the spatial coordinates:

$$p_x = \partial_x t_N = \partial_x t_{NIP}, \quad \hat{M}_N = \partial_{xx} t_N, \quad \hat{M}_{NIP} = \partial_{xx} t_{NIP}. \tag{5.3}$$

In the 3D case, the number of the wavefront attributes is grown to eight.

Since the wavefront attribures describe kinematics of the propagated waves, their extracting is crucial for many seismic processing applications, e.g., for formulating the wavefront tomography (Duveneck, 2004; Bauer et al., 2017). When the medium is isotropic and seismic velocity, v_0, is assumed to be known and homogeneous at the acquisition line, e.g., in the case of the towed streamer acquisition, the wavefront attributes are linked directly to the emergence angle, α_0, and N- and NIP-wave wavefront curvatures, K_N and K_{NIP} (Fig. 5.1):

$$p_x = \frac{\sin\alpha_0}{v_0}, \quad \hat{M}_N = \frac{\cos^2\alpha_0}{v_0} K_N, \quad \hat{M}_{NIP} = \frac{\cos^2\alpha_0}{v_0} K_{NIP}. \tag{5.4}$$

Note, the curvature attributes $\hat{M}_N$ and $\hat{M}_{NIP}$ are marked with a hat sign to distinguish them from the dynamic ray tracing quantities, M_N and M_{NIP} (Červený, 2001):

$$\hat{M}_N = \cos^2\alpha_0 M_N, \quad \hat{M}_{NIP} = \cos^2\alpha_0 M_{NIP}. \tag{5.5}$$

In the multicomponent approach which we present in this paper laterally variable values of P- and S-wave surface-velocities appear as an additional output. They allow for the subsequent determination of the emergence angle α_0. However, since eqs (5.4) and (5.5), in the case of heterogeneous velocity at the acquisition line, contain spatial derivatives of the velocity model, the curvatures K_N and K_{NIP} can be extracted only if the heterogeneity is negligible.

In practice, the wavefront attributes are determined by an analysis of semblance (Neidell and Taner, 1971; Mann, 2002). It represents a ratio of the stacked energy to the average energy in a user-defined coherence window, for i-th time sample:

$$S(i) = \frac{\sum\limits_{j=i-\frac{n}{2}}^{i+\frac{n}{2}} \left(\sum\limits_{k=1}^{m} u_{jk} \right)^2}{m \sum\limits_{j=i-\frac{n}{2}}^{i+\frac{n}{2}} \sum\limits_{k=1}^{m} u_{jk}^2}, \tag{5.6}$$

where m is a trace number, n is the length of the coherence window, and u_{jk} is the scalar wavefield (or single component) value of the jk-sample in the window. The wavefield is interpolated at traveltimes given by eq. (5.2), which makes the semblance coefficient (5.6) depending on the wavefront attributes.

The wavefront attributes maximizing the semblance are supposed as searched-for attributes. Finally, enhancement of the data is carried out by stacking:

$$St(i) = \frac{1}{m} \sum_{j=1}^{m} u_{ij}. \tag{5.7}$$

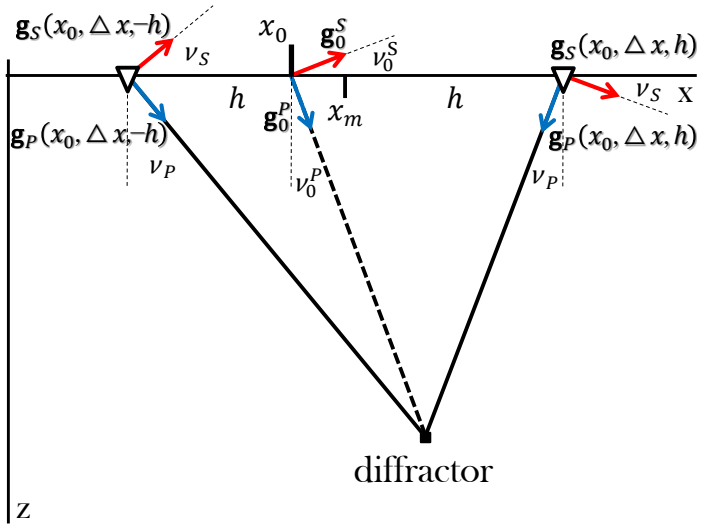

Figure 5.2: Polarization vectors $\mathbf{g}_P$ and $\mathbf{g}_S$ depending on the midpoint displacement $\triangle x_m$ and the half-offset h. ν_P and ν_S are polarization angles. The quantities with a zero in the subscript are central, i.e., they correspond to the case of zero midpoint displacement and zero offset. For P-waves it is reasonable to use the lower half-plane $z \geq 0$ constraining the polarization vector, whereas for S-waves it is naturally to constrain the polarization vector within the right half-plane $x \geq 0$.

5.3 Polarization-consistent stacking

For a certain central midpoint with coordinate x_0, we consider a polarization vector, $\mathbf{g}(x_0, \triangle x_m, h)$, as a function of the midpoint displacement $\triangle x_m$ and the half-offset h (Fig. 5.2). One could visualize it as a smooth vector field of a unit length, which is attached to the common-reflection-surface in a space spanned by $\triangle x_m$-, h-, and t-axis. Alternatively, one could imagine a polarization angle surface in the same space. We locally describe the polarization vector with three attributes: polarization angle of the zero-offset ray emerging at the central midpoint location, ν_0; polarization angle derivative with respect to the midpoint coordinate, ν_{x_m}; and polarization angle derivative with respect to the half-offset, ν_h. A detailed discussion on approximations of the polarization vector, $\hat{\mathbf{g}}(x_0, \triangle x_m, h)$, parametrized with these attributes is given in Section 5.4.

The polarization-consistent stacking is based on an optimization of the total projection of the wavefield onto the variable polarization vector. The cumulative projection reaches its maximum at the correctly determined alternating polarization. On this basis we introduce an energy function for the multicomponent CRS stack with the scalar product of multicomponent data $\mathbf{u}$ and the polarization vector approximation $\hat{\mathbf{g}}$:

$$E(p_x, \hat{M}_N, \hat{M}_{NIP}; \nu_0, \nu_{x_m}, \nu_h) = \sum_{CRS} (\mathbf{u}, \hat{\mathbf{g}})^2. \tag{5.8}$$

The sign of summation over CRS denotes a summation over traces along the traveltimes (5.2) parametrized with the wavefront attributes p_x, $\hat{M}_N$, and $\hat{M}_{NIP}$. The approximation $\hat{\mathbf{g}}(x_0, \triangle x_m, h)$ is parametrized with the polarization attributes ν_0, ν_{x_m}, and ν_h. In that way, the energy function (5.8) becomes a function of six variables, multicomponent CRS

attributes. The wavefront attributes together with the polarization attributes can be determined for different central midpoints and time samples by maximization of this energy function.

However, by an analogy to the single component stacking, we seek a normalized measure for the amplitude-coherency analysis. Therefore, we generalize the conventional semblance (5.6) and extend the analysis to the multicomponent data:

$$S(i) = \frac{\sum\limits_{j=i-\frac{n}{2}}^{i+\frac{n}{2}} \left(\sum\limits_{k=1}^{m} (\mathbf{u}_{jk}, \hat{\mathbf{g}}_j) \right)^2}{m \sum\limits_{j=i-\frac{n}{2}}^{i+\frac{n}{2}} \sum\limits_{k=1}^{m} \mathbf{u}_{jk}^2}, \tag{5.9}$$

where $\mathbf{u}_{jk}$ is the vector wavefield value, and $\hat{\mathbf{g}}_k$ is a value of the polarization vector for the trace with number k. The multicomponent semblance represents a ratio of the stacked energy of the projected wavefield to the average energy in a user-defined window.

After the determination of the multicomponent CRS attributes, we perform a polarization-consistent stack:

$$St(i) = \frac{1}{m} \sum_{j=1}^{m} (\mathbf{u}_{ij}, \hat{\mathbf{g}}_j). \tag{5.10}$$

By the weighting of multicomponent data we account for the variations of the wave polarization along the stacking operator. The enhanced vertical and horizontal component sections are subsequently obtained by a projection of the polarization-consistent stack section by means of the section with polarization angle ν_0. Note that, as soon as the multicomponent CRS attributes are available, a prestack enhancement of multicomponent data can be performed in a similar way as proposed in Baykulov and Gajewski (2009).

In the 2D case, the polarization-consistent CRS stacking demands values of the six attributes. Generally speaking, determination of the attributes requires an optimization in the six-dimensional unknowns space. This could be still computationally expensive. To reduce the dimensionality and incorporate the conventional three-parameter CRS, we suggest splitting of the six-dimensional optimization into a sequence of three-parameter searches which is summarized in the following step-by-step scheme:

1. conduct wavefront attribute search independently for both single components;

2. merge the resulting sections by a coherence-based selection of the single-component wavefront attributes;

3. perform polarization attribute search, i.e., use jointly the single components to maximize the semblance (5.9) for the fixed wavefront attributes previously determined in the step 2;

4. do the polarization-consistent stack, eq. (5.10), using the determined wavefront and polarization attributes.

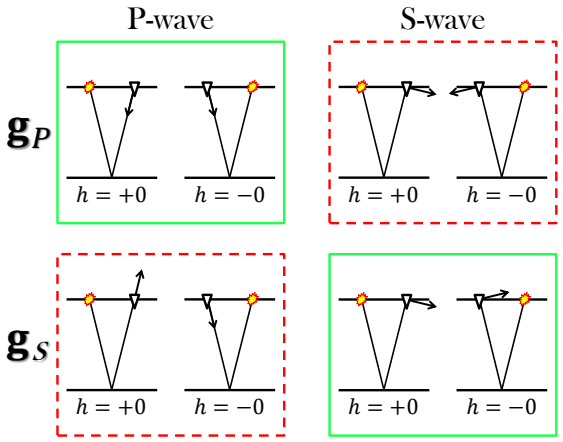

Figure 5.3: Polarization vector discontinuities due to the half-space representations. Applying the P-representation, suitable for P-waves, leads to the discontinuity of the S-wave polarization vector (top-right figure). Applying the S-representation, suitable for S-waves, leads to the discontinuity of the P-wave polarization vector (bottom-left figure).

5.4 Polarization vector on common-reflection-surface

A vector characterizing wave polarization is defined up to the sign. This implies that a vector opposite to an estimated one is also relevant. Therefore, a complete set of polarizations is equivalent to the full set of lines passing through a point. In mathematics, such an object in 2D is called real projective line. The ambiguity can lead to a non-unique determination of the polarization vector. One of the ways to tackle this issue is constraining of polarization vector directions. However, as will be shown, such constraining properly works for a single mode (P- or S-) processing and faces problems in a simultaneous P- and S-waves imaging. Later on, we will formulate an alternative approach to cope the non-uniqueness of the polarization vector which is suitable for the simultaneous processing as well.

We limit the set of polarization vectors by choosing those vectors which are directed only to a certain half-plane. For P-waves, a natural condition for constraining is that the polarization vector lies in the lower half-plane $z \geq 0$, while for S-waves we constrain the polarization vector with the right half-plane $x \geq 0$, as shown in Fig. 5.2. Accordingly, by considering polarization angles ν_P and ν_S we introduce the natural P- and S-representations in the component form:

$$\mathbf{g}_P = \begin{pmatrix} -\sin\nu_P \\ \cos\nu_P \end{pmatrix}, \quad \mathbf{g}_S = \begin{pmatrix} \cos\nu_S \\ \sin\nu_S \end{pmatrix}, \quad -90^\circ < \nu_{P,S} \leq 90^\circ. \tag{5.11}$$

The simplest first-order approximation, parametrized with three attributes, follows from the linear expansion of the polarization angle:

$$\begin{aligned} \hat{\mathbf{g}}_P(x_0, \triangle x_m, h) &= \begin{pmatrix} -\sin(\nu_0 + \nu_{x_m}\triangle x_m + \nu_h h) \\ \cos(\nu_0 + \nu_{x_m}\triangle x_m + \nu_h h) \end{pmatrix}, \\ \hat{\mathbf{g}}_S(x_0, \triangle x_m, h) &= \begin{pmatrix} \cos(\nu_0 + \nu_{x_m}\triangle x_m + \nu_h h) \\ \sin(\nu_0 + \nu_{x_m}\triangle x_m + \nu_h h) \end{pmatrix}. \end{aligned} \tag{5.12}$$

We introduce new scalar attributes: polarization angle ν_0 of the zero-offset ray emerging at the central midpoint location, polarization angle derivative with respect to the midpoint coordinate, ν_{x_m}, and polarization angle derivative with respect to the half-offset, ν_h. Further refinement of the approximations (5.12) by expanding the polarization angle up to the higher order may be used for more accurate applications to larger offsets and non-hyperbolic events. It turns out that the first-order polarization coefficients ν_{x_m} and ν_h can be expressed in terms of the second-order expansion of the traveltimes (see Appendix D.1). This implies to a certain extent that we stay within the same order for both polarizations and traveltimes.

Linearizing the polarization vectors in eq. (5.12) leads to another approximation as followed:

$$\hat{\mathbf{g}}_{P,S}(x_0, \triangle x_m, h) = \frac{\mathbf{g}_0^{P,S} + (\nu_{x_m} \triangle x_m + \nu_h h) R^+ \mathbf{g}_0^{P,S}}{\sqrt{1 + (\nu_{x_m} \triangle x_m + \nu_h h)^2}}, \tag{5.13}$$

where

$$\mathbf{g}_0^P = \begin{pmatrix} -\sin \nu_0^P \\ \cos \nu_0^P \end{pmatrix}, \quad \mathbf{g}_0^S = \begin{pmatrix} \cos \nu_0^S \\ \sin \nu_0^S \end{pmatrix} \tag{5.14}$$

are central polarization vectors, and R^+ is a 90° clockwise rotation matrix. The approximation given by eq. (5.13) is normalized in order to prevent an undesired growth of semblance (5.9) when ν_{x_m} and ν_h increase. The attributes ν_0, ν_{x_m}, and ν_h are responsible for a local behaviour of both polarization vector approximations (5.12) and (5.13):

$$\begin{aligned} \hat{\mathbf{g}}_{P,S}(x_0, 0, 0) &= \mathbf{g}_0^{P,S}, \\ \partial_{\triangle x_m} \hat{\mathbf{g}}_{P,S}(x_0, 0, 0) &= \nu_{x_m} R^+ \mathbf{g}_0^{P,S}, \\ \partial_h \hat{\mathbf{g}}_{P,S}(x_0, 0, 0) &= \nu_h R^+ \mathbf{g}_0^{P,S}. \end{aligned} \tag{5.15}$$

Consequently, the attributes extracted from the data locally describe the actual polarization.

From now on, we will assume an isotropic medium. The introduced P- and S-representations (5.11) behave differently with regard to the wave modes under consideration. Namely, a representation is suitable only for processing of waves of the same kind. This is due to the fact that the approximations (5.12) and (5.13) are derived under the assumption of smoothness of the polarization vector as a function of the midpoint displacement and the half-offset. However, it may be violated. The polarization vector defined by the P-representation may undergo a jump when applied to S-waves. The same applies for the polarization vector of P-waves described by the S-representation. This kind of behaviour takes place where the horizontal slowness of a registered wave vanishes. For instance, in a CMP experiment with a horizontal reflector in a laterally homogeneous medium the issue appears at zero offsets, as shown in Fig. 5.3. Common-reflection-surface can be divided into two parts by a curve at which the horizontal slowness vanishes. If this curve crosses an aperture rectangle, centered at the origin of the $\triangle x_m$-h plane, application of the approximations (5.12) and (5.13) to extrinsic events may lead to erroneous results. Evidently, the discontinuity will take place when the horizontal slowness of the central ray, p_x, is small. For small midpoint displacements and offsets the curve becomes a straight line:

$$\partial_{x_r} t = \hat{M}_N \triangle x_m + \hat{M}_{NIP} h + p_x = 0. \tag{5.16}$$

The horizontal slowness of the central ray p_x is responsible for the distance between this line and the origin of the $\triangle x_m$-h plane. Therefore, we don't expect the discontinuity to be an issue for steeper arrivals, like diffraction events away from their apices.

In order to image both of the wave modes at the same time, we apply a strategy to tackle the discussed-above problem of unique representation discontinuity. We use a representation which is not unique but smooth. For the sake of simplicity, we will consider only the P-representation. This means, an approximation $\hat{\mathbf{g}}_P$ from eqs. (5.12) or (5.13) is involved. We allow the polarization angle attribute ν_0 to vary from $-180°$ to $180°$. The result is that the semblance, eq. (5.9), has two distinct maximums which correspond to opposite directions of the central polarization vector. In any case, the optimization method converges to one of these solutions resulting in three attribute values, ν_0, ν_{x_m}, and ν_h. Afterwards, we simply turn the values back to the description by the unique P-representation. Namely, we increase the ν_0 value by adding $180°$ if in the found solution $\nu_0 \leq -90°$, or we decrease the ν_0 value by subtracting $180°$ if $\nu_0 > 90°$. The value $\nu_0 = -90°$ corresponds to the vertical incidence of S-waves, and we alter it as well. The derivatives ν_{x_m} and ν_h are kept unaltered. Unlike the derivatives of the vectors, they are invariant with respect to a change of representation since vectors aligned in opposite directions have equal angle increments. This fact also leads to continuity of ν_{x_m} and ν_h along an event in contrast to the polarization angle attribute ν_0. In this way, we process both P- and S-waves obtaining the attributes in terms of one of the representations (5.11). One can easily switch between the representations in the determined attribute sections when needed.

In Appendix D.1 we show that the derivatives of reflected-wave polarizations with respect to the midpoint coordinate and the half-offset can be interpreted in terms of the hypothetical N- and NIP-waves, respectively:

$$
\begin{aligned}
\partial_{\triangle x_m}\mathbf{g}_P(x_0,0,0) = \partial_x \mathbf{g}_N^P &= -\left(v_P \begin{pmatrix} \partial_{xx} \\ \partial_{xz} \end{pmatrix} t_N^P + \partial_x v_P \mathbf{p}_P \right), \\
\partial_h \mathbf{g}_P(x_0,0,0) = \partial_x \mathbf{g}_{NIP}^P &= -\left(v_P \begin{pmatrix} \partial_{xx} \\ \partial_{xz} \end{pmatrix} t_{NIP}^P + \partial_x v_P \mathbf{p}_P \right), \\
\partial_{\triangle x_m}\mathbf{g}_S(x_0,0,0) = \partial_x \mathbf{g}_N^S &= R^+ \left(v_S \begin{pmatrix} \partial_{xx} \\ \partial_{xz} \end{pmatrix} t_N^S + \partial_x v_S \mathbf{p}_S \right), \\
\partial_h \mathbf{g}_S(x_0,0,0) = \partial_x \mathbf{g}_{NIP}^S &= R^+ \left(v_S \begin{pmatrix} \partial_{xx} \\ \partial_{xz} \end{pmatrix} t_{NIP}^S + \partial_x v_S \mathbf{p}_S \right),
\end{aligned}
\tag{5.17}
$$

where $\mathbf{g}_N^P$, $\mathbf{g}_{NIP}^P$ are polarizations of compressional N- and NIP-waves, and $\mathbf{g}_N^S$, $\mathbf{g}_{NIP}^S$ are polarizations of shear N- and NIP-waves. These formulas are given in the natural representations: in the P-representation for P-waves and in the S-representation for S-waves. They are valid only for monotypic waves, and the modes conversion at the free surface is neglected.

In the case of point diffractor, traveltimes of the fictitious waves coincide, i.e., $t_N = t_{NIP}$ (e.g., Dell and Gajewski, 2011). For the CRS attributes this means that the N- and NIP-wave curvature attributes are equal: $\hat{M}_N = \hat{M}_{NIP}$. However, for the polarization attributes it also implies identity in the midpoint and the offset directions: $\partial_{x_m}\mathbf{g} = \partial_h \mathbf{g}$ and $\nu_{x_m} = \nu_h$.

When the velocities at the acquisition line are assumed to be homogeneous, the polariza-

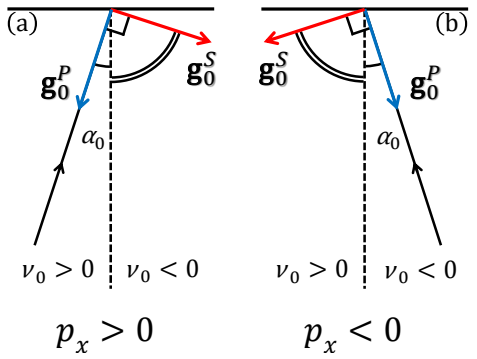

Figure 5.4: The P- and S-waves separation principle based on the sign of horizontal slowness and polarization angle. It is valid for both, positive (a) and negative (b) emergence angles. The criterion is summarized as followed: for P-waves applies $\nu_0 p_x > 0$, for S-waves applies $\nu_0 p_x < 0$.

tion angle derivatives are fully described by the curvatures of the hypothetical wavefronts and the emergence angle:

$$
\begin{aligned}
\partial_{\triangle x_m}\mathbf{g}_P(x_0,0,0) &= -\begin{pmatrix}\cos^2\alpha_0^P\\ \sin\alpha_0^P\cos\alpha_0^P\end{pmatrix}K_N^P, \quad \nu_{x_m}^P = \cos\alpha_0^P K_N^P;\\
\partial_h\mathbf{g}_P(x_0,0,0) &= -\begin{pmatrix}\cos^2\alpha_0^P\\ \sin\alpha_0^P\cos\alpha_0^P\end{pmatrix}K_{NIP}^P, \quad \nu_h^P = \cos\alpha_0^P K_{NIP}^P;\\
\partial_{\triangle x_m}\mathbf{g}_S(x_0,0,0) &= \begin{pmatrix}-\sin\alpha_0^S\cos\alpha_0^S\\ \cos^2\alpha_0^S\end{pmatrix}K_N^S, \quad \nu_{x_m}^S = \cos\alpha_0^S K_N^S;\\
\partial_h\mathbf{g}_S(x_0,0,0) &= \begin{pmatrix}-\sin\alpha_0^S\cos\alpha_0^S\\ \cos^2\alpha_0^S\end{pmatrix}K_{NIP}^S, \quad \nu_h^S = \cos\alpha_0^S K_{NIP}^S.
\end{aligned}
\tag{5.18}
$$

This follows from eqs (5.17) and the relation between second-order traveltime derivatives with respect to global Cartesian and local Cartesian ray-centered coordinates (e.g., Červený, 2001). Note, the formulas for the angle derivatives in eqs (5.18) are independent of the P- or S- representation, unlike the formulas for the vector derivatives, which correspond to the representations chosen for eqs (5.17).

5.5 Attributes-based P- and S-waves separation and surface-velocities model building

Bergler et al. (2002) proposed a method to separate P- and S-wave arrivals stacked to zero-offset, as well as the wavefront attributes, by means of matching emergence and polarization angles. They introduced this approach in a context of a five-parameter converted-waves CRS. Nevertheless, it is also valid for processing of monotypic events by the conventional three-parameter CRS. The emergence angle can either be directly picked during the CRS stacking or subsequently transformed from the slope attribute. In both cases a surface-velocity model is necessary. The polarization angle is obtained from independently stacked

components of the vector wavefield. Then, the wave modes are sorted in accordance to a difference between the polarization and emergence angles. However, an a priori surface-velocity model may not always be available in practice. In contrast, we present a completely data-driven technique and do not make any assumptions about the surface velocities. We unambiguously identify the arrivals and subsequently retrieve the compressional- and shear-wave velocities at the acquisition line. To do this, we apply another separation criterion to the slowness and polarization angle attributes and build the surface-velocities model by the slowness-polarization method (Dewangan and Grechka, 2003; Tsvankin and Grechka, 2011). Moreover, the polarization angle attribute is obtained with the polarization-consistent stack in our approach naturally accounting for the variation of polarization in the prestack data. Note, this is not the case when the components are stacked independently as proposed in the paper by Bergler et al. (2002). The slowness-polarization method in isotropic media degenerates to an explicit estimating with no regression involved. However, the estimates become unstable in the case of nearly normal emergence. Therefore, we provide a complementary alternative through the second-order quantities, the polarization angle derivatives and the wavefront curvature attributes.

We will formulate the separation criterion in terms of the P-representation. As described in Section 5.4, the P-representation implies the polarization vector to be directed downwards and the polarization angle to be measured from the vertical axis. The separation criterion is illustrated in Fig. 5.4. If the horizontal slowness is greater than zero, i.e., $p_x > 0$, the following relations hold:

$$\nu_0 > 0 \;\text{ for P-waves, and }\; \nu_0 < 0 \;\text{ for S-waves.} \tag{5.19}$$

If the horizontal slowness is less than zero, i.e., $p_x < 0$, the opposite relations hold:

$$\nu_0 < 0 \;\text{ for P-waves, and }\; \nu_0 > 0 \;\text{ for S-waves.} \tag{5.20}$$

The criterion for identifying arrivals reads as follows:

$$\nu_0 p_x > 0 \;\Rightarrow\; P, \quad \nu_0 p_x < 0 \;\Rightarrow\; S. \tag{5.21}$$

In the case of normal emergence, when p_x is sufficiently small, we examine whether the absolute value of ν_0 is also small. Despite the fact that in the zero-order ray theory a case of small but non-zero horizontal slowness and zero polarization angle is not allowed, it is reasonable on practice to account for this possibility by making the P-wave condition non-strict. Classification is performed for all time samples and central midpoints, which allows to form a P- and S-wave filter. The filter is subsequently applied to the attribute and stack sections.

The above-described arrivals identification is an essential part of the surface-velocities and the slowness vector building. For P-waves, the polarization angle ν_0 is equal to the emergence angle α_0. Therefore, the compressional-wave velocity is computed as $v_P = \sin\nu_0/p_x$. The vertical slowness component reads then as $p_z^P = -(v_P^{-2} - {p_x}^2)^{\frac{1}{2}}$. For the S-wave arrivals, however, this is erroneous as we first need to determine the emergence angle: $\alpha_0 = \nu_0 \pm 90°$. Here, "+" stands for negative and "−" for positive polarization angle ν_0. With the corrected value of the emergence angle we are able to build the shear-wave velocity, again as $v_S = \sin\alpha_0/p_x$, and the vertical slowness component as $p_z^S = -(v_S^{-2} - {p_x}^2)^{\frac{1}{2}}$. The

CRS attributes differ from the exact theoretical values. They are sensitive to the level of noise and the stacking apertures. Therefore, a workaround is needed to prevent a potential instability in the determination of the velocities which occur in the case of almost normal emergency of the central rays (e.g., a diffraction apex or reflection in a laterally homogeneous medium). The alternative is incorporating the first-order polarization and the second-order traveltime attributes. From eqs (5.15) and (5.17) we conclude that the following identities take place when the horizontal slowness vanishes:

$$v_P = \frac{\nu^P_{x_m}}{\hat{M}^P_N} = \frac{\nu^P_h}{\hat{M}^P_{NIP}}, \quad v_S = \frac{\nu^S_{x_m}}{\hat{M}^S_N} = \frac{\nu^S_h}{\hat{M}^S_{NIP}}. \tag{5.22}$$

Note, if at a central midpoint location the velocity model gradient does not have a horizontal component (no lateral variations) the formulas

$$v_P = \frac{\nu^P_{x_m} \cos \nu^P_0}{\hat{M}^P_N} = \frac{\nu^P_h \cos \nu^P_0}{\hat{M}^P_{NIP}}, \qquad v_S = \frac{\nu^S_{x_m} \sin \left|\nu^S_0\right|}{\hat{M}^S_N} = \frac{\nu^S_h \sin \left|\nu^S_0\right|}{\hat{M}^S_{NIP}}. \tag{5.23}$$

remain valid regardless of the horizontal slowness value. In the expression for the S-wave velocity the polarization angle attribute ν^S_0 is given in the P-representation as this representation was chosen for processing both wave modes from the beginning. A pair ν_h and $\hat{M}_{NIP}$ in eqs (5.23) is strongly recommended for the velocity estimation with reflections since the attributes ν_{x_m} and $\hat{M}_N$ are less reliable in this case due to the higher uncertainty of fitting traveltimes with smaller curvatures. Estimating with the second-order quantities, oppositely to the first-order slowness-polarization method, becomes unstable in the case of vanishing curvature attributes (e.g., flanks of diffraction). In this sense, the first- and the second-order attributes and the correspondent estimates are complementary to each other.

We have discussed the slowness-polarization approach to estimate the local velocities. Velocity is evaluated here independently for every central midpoint location, which requires only one arrival per each wave mode. Theoretically, this is sufficient in the case of isotropic media. However, to decrease uncertainties in the retrieved models caused by possible errors in the attribute values, one can incorporate more central midpoints and more arrivals as well. For instance, if the velocity model is assumed homogeneous all along the acquisition line, polarization vectors and slopes from all the central midpoints can be utilized. In the case of anisotropy, incorporation of arrivals emerging at one central midpoint from different directions will improve illumination. This can be done by applying the slowness-polarization method in terms of Christoffel equation fitting as it was formulated by Dewangan and Grechka (2003) for VSP walkaway data.

In the case of inhomogeneity presented at the acquisition line, eqs (5.4) and (5.5) have additional terms containing spatial derivatives of the velocity model (when precisely derived with a relation between traveltime derivatives with respect to the global Cartesian and the local Cartesian ray-centered coordinates (e.g., Červený, 2001)). Unfortunately, we are not able to extract a value of the vertical velocity gradient from the wavefront attributes and the zero-order ray method polarizations, consequently, not able to account for these terms. Therefore, the extraction of the wavefront curvatures K_N and K_{NIP}, as well as the dynamic ray tracing quantities M_N and M_{NIP}, from the $\hat{M}_N$ and $\hat{M}_{NIP}$ attribute sections without a priori knowledge of the vertical gradient value may be inaccurate for strongly heterogeneous near-surface.

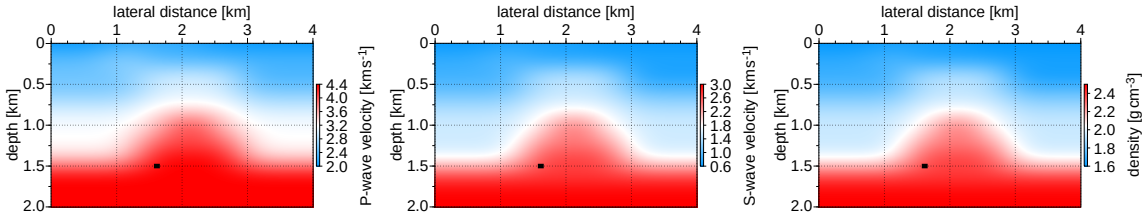

Figure 5.5: Elastic model used to generate the synthetic data. Position of the point diffractor is depicted with a black dot.

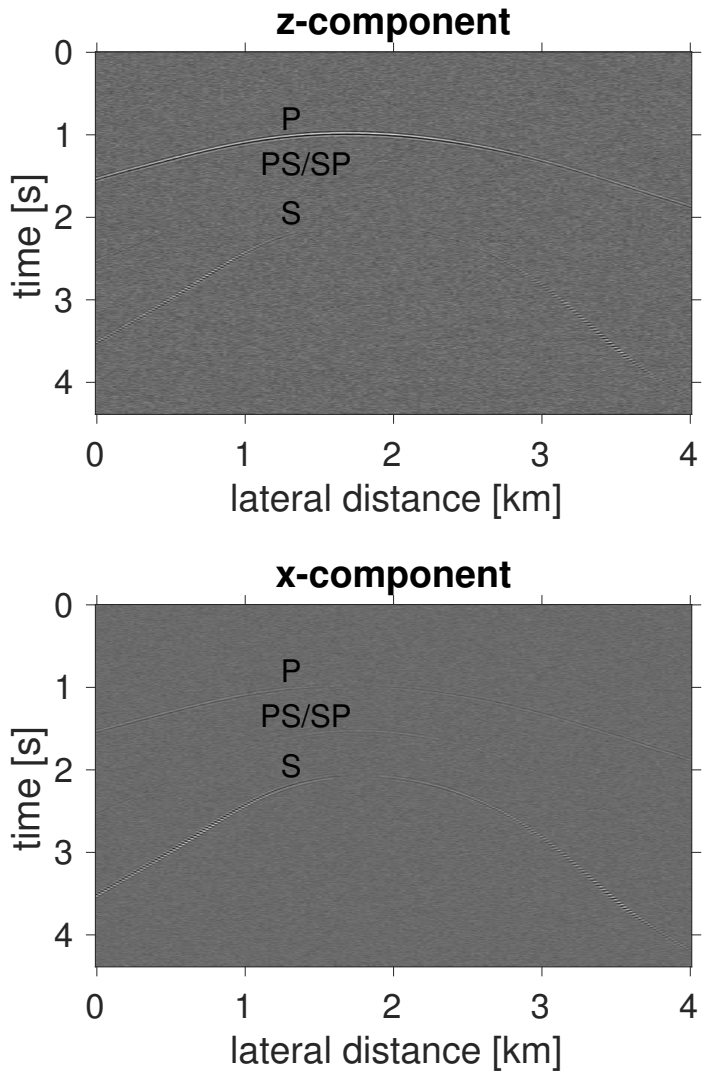

Figure 5.6: Zero-offset sections after adding the noise. The diffraction response was modeled by the elastic rapid expansion method and a subsequent direct waves attenuation. Gaussian noise with the S/N of 20 was added to the traces.

5.6 Synthetic example

We use a smooth model comprising a salt body covered by sediments and a point diffractor for testing the presented method. Elastic parameters of the background and position of the diffractor are depicted in Fig. 5.5. First, the P- and S-wave velocity models are built with a set of 4-th order B-spines placed on an 11×11 grid of nodes. Moreover, moderate near-surface variations are introduced in order to test feasibility of the surface-velocities retrieval (Fig. 5.13). The velocity of S-waves is scaled to get a physically reasonable density model. The low velocity point diffractor has the following elastic parameters values: $v_P = 3\ \mathrm{km\,s^{-1}}$, $v_S = 2.4\ \mathrm{km\,s^{-1}}$, $\rho = 2\ \mathrm{g\,cm^{-3}}$. We employ the vertical force source and a Ricker wavelet with prevailing frequency of 25 Hz. The 2D elastic modeling is based on the Fourier method with high-accuracy time integration by rapid expansion (Kosloff and Baysal, 1982; Kosloff et al., 1989). Data are simulated on the top of the model with source and receiver spacing of 20 m. Direct waves are muted, so that the data contain primarily diffracted wavefield. We add some Gaussian noise to the multicomponent traces so that the S/N of the diffraction only dataset becomes equal to 20. Resulting zero-offset sections of both elastic displacement components are presented in Fig. 5.6. We observe distinctively separated in time monotypic P-wave and S-wave diffractions. The P-wave is prominent in the vertical component section, while the S-wave dominates in the section with the horizontal one. Note, the amplitude of the monotypic S-wave diffraction vanishes at the apex due to the source radiation pattern and the phase of the horizontal component undergoes a reversal. An intermediate arrival represents a superposition of converted PS- and SP-wave, which have coincident zero-offset traveltimes.

Following the workflow suggested in Section 5.3, we start determining the wavefront attributes independently for the vertical and for the horizontal component. During the wavefront and polarization attributes search we restrict the maximum offset to 700 m and the displacement aperture to 150 m. Global optimization is performed by the method of differential evolution (e.g., Walda and Gajewski, 2017). We also allow both positive and negative offsets imitating a seafloor or an onshore acquisition. The single component wavefront attribute searches are in turn carried out in the pragmatic way (Jäger et al., 2001): first $\hat{M}_{NIP}$ is determined with the CMP stack, then the small aperture slant-stack is applied to the zero-offset stack section resulting in the p attribute, both p and $\hat{M}_{NIP}$ attributes are slightly adjusted and the attribute $\hat{M}_N$ is determined simultaneously by the three-dimensional optimization. The result for the vertical component is shown in Fig. 5.7. Analogous sections for the horizontal component are shown in Fig. 5.8. We clearly observe higher coherence of the monotypic waves (Figs 5.7a and 5.8a). The converted-waves arrival is, however, poorly described not only due to an inaccuracy of the CRS approximation but also because the PS- and SP-wave have different moveout and both are present in the dataset. The corresponding attribute values are erroneous. Note also a lack of the stack energy near the traveltime apex of the S-wave in the semblance section for the vertical component and, similarly, a P-wave energy lack in the semblance section for the horizontal component. This polarization effect leads to undetermined wavefront attributes.

At the second step, we combine the single-component attribute sections into the joint sections, which heals the attribute gaps. Indeed, the attribute quality is improved and the semblance upraises (Fig. 5.9).

The third step is the multicomponent CRS semblance analysis using the wavefront at-

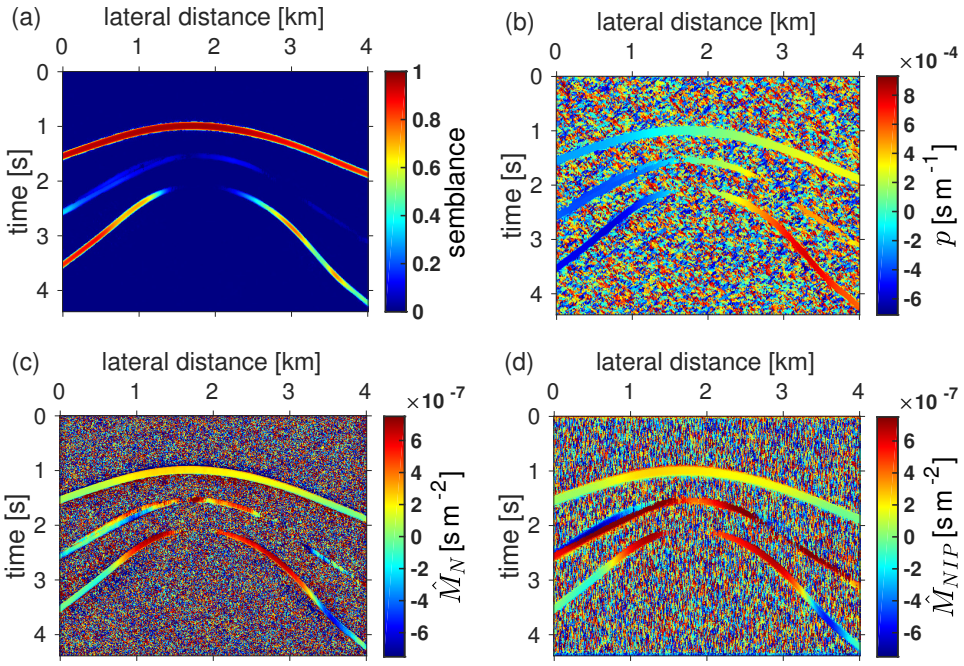

Figure 5.7: Vertical component sections: (a) semblance; (b) slowness; (c) N-wave curvature attribute; (d) NIP-wave curvature attribute.

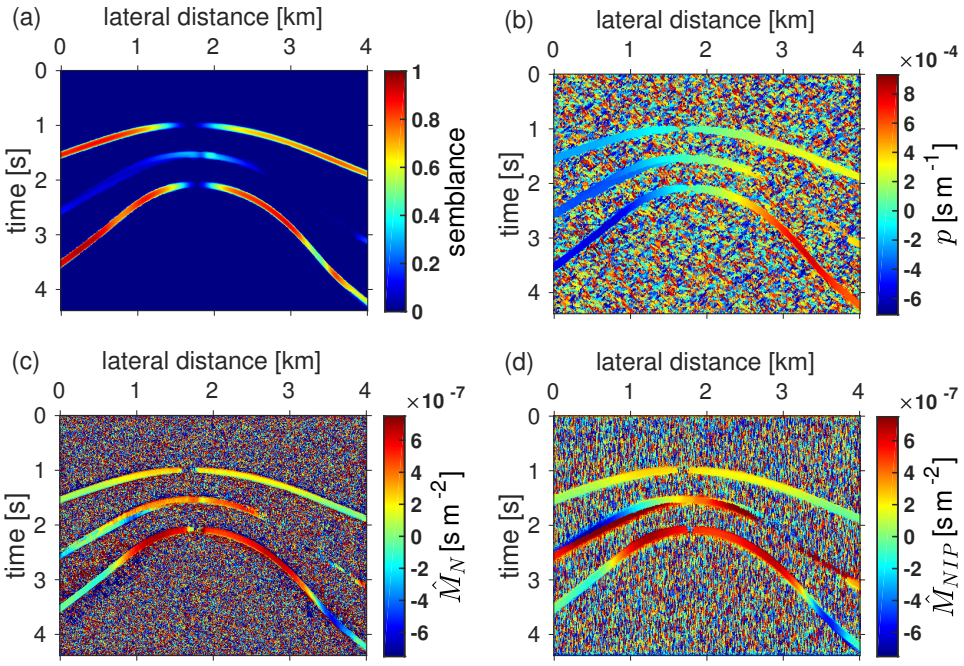

Figure 5.8: Horizontal component sections: (a) semblance; (b) slowness; (c) N-wave curvature attribute; (d) NIP-wave curvature attribute.

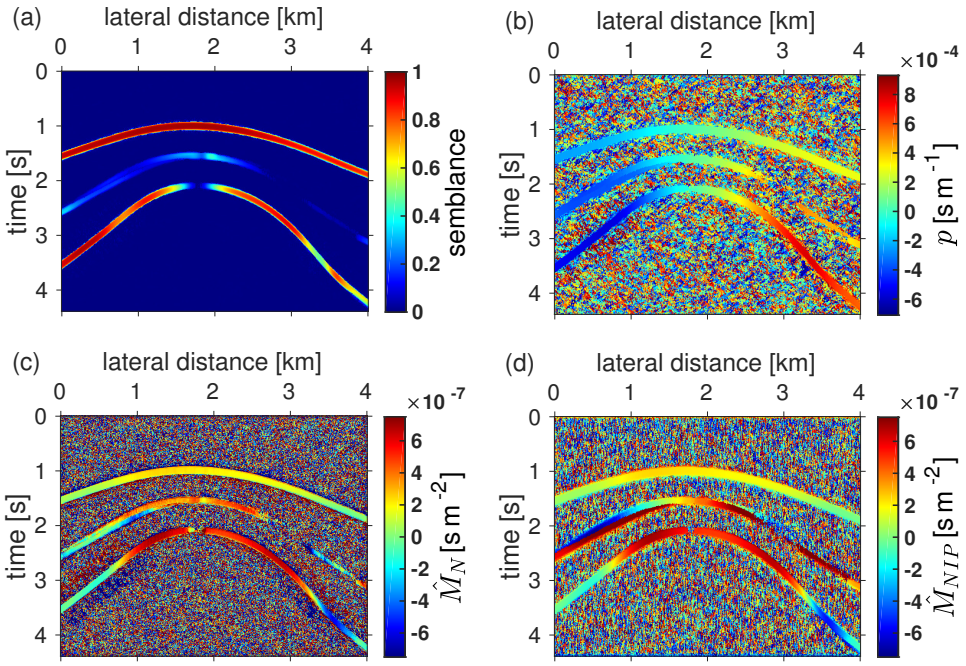

Figure 5.9: Joint sections: (a) semblance; (b) slowness; (c) N-wave curvature attribute; (d) NIP-wave curvature attribute.

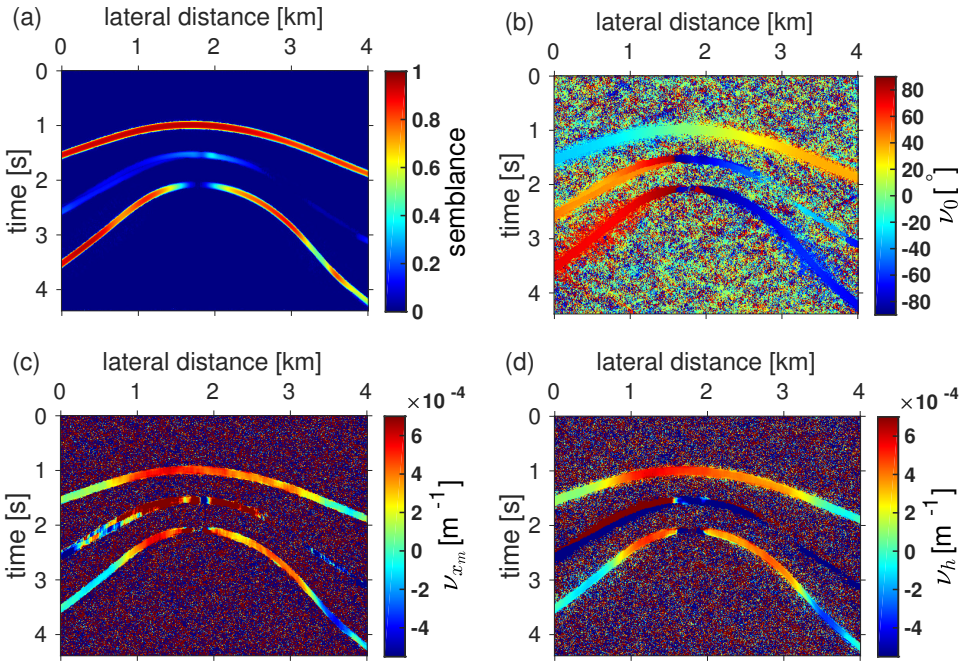

Figure 5.10: Multicomponent sections: (a) semblance; (b) polarization angle; (c) polarization angle derivative with respect to the midpoint displacement; (d) polarization angle derivative with respect to the half-offset.

tributes from the joint sections. They remain fixed during the optimization. The local polarization is built by retrieving the polarization attributes (Figs 5.10b-d). We see, the polarization angle attribute as well as the polarization angle derivatives are determined everywhere except the phase reversal zone at the S-wave apex. We adhere the P-representation with polarization vector directed downwards and polarization angle measured with respect to the vertical axis (see Section 5.4). Accordingly, we get smaller angles at the P-wave apex and a jump from $-90°$ to $90°$ at the apex of the S-wave traveltime (Fig. 5.10b) In contrast, as explained in Section 5.4, the values of both polarization angle derivatives are continuous along the events (Figs 5.10c and d). Stacking in the zone of S-wave phase reversal fails causing unreliable attribute values. As the proposed method is applied to diffraction data, the polarization angle derivatives picked for monotypic arrivals coincide (Figs 5.10c and d), i.e., $\nu_{x_m} = \nu_h$, similarly to the sections in Figs 5.9(c) and (d) with coincident wavefront curvature attributes, $\hat{M}_N = \hat{M}_{NIP}$. We have found out that both polarization vector approximations, (5.12) and (5.13), are suitable for the multicomponent processing. There are no significant differences for our setting.

The final step is the enhancement of the multicomponent data by stacking. The stacking aperture was 200 m both for the half-offset and the midpoint displacement. The enhanced sections are displayed in Fig. 5.11. The polarization-consistent stack section (Fig. 5.11a) is free of the wavefield inclination effect. It has both wave modes equally presented in this sense. Due to the unreliably determined polarization angle around the S-wave apex there are discontinuities present in the polarization-consistent stack. But they disappear in the enhanced single-component sections. We achieve the S/N improvement of the zero-offset sections for both displacement components by projecting pixel-by-pixel the polarization-consistant stack section onto the axes of the Cartesian coordinate system. The projecting is carried out by means of the polarization angle section given in Fig. 5.10b. Comparing the processed single component sections (Fig. 5.11b and c) with the raw noisy traces (Fig. 5.6) clearly demonstrates that all polarization features are preserved and the data are sufficiently enhanced. Note also an interpolation of the zero-offset traces made with the CRS stack by introducing central midpoints between the actual receiver locations.

Having the slowness (Fig. 5.9b) and polarization (Fig. 5.10b) attributes in hand, we are able to separate the P- and S-wave enhanced waveforms as well as the attribute sections. We construct a filter based on the separation criterion as presented in Fig. 5.12. The monotypic events are perfectly identified with an exception again near the S-wave apex where the wrong polarization angles are misleading. The identification applied to the converted waves, despite being not justified theoretically, apparently reveals dominating of the PS-wave energy.

We retrieve the compressional- and shear-wave velocities on the top of the model independently for every central midpoint by picking and processing the attributes. The estimated surface-velocities are plotted in Fig. 5.13. One way is to utilize horizontal slowness and polarization angle (first-order estimates). Alternatively, NIP-wave curvature attribute and polarization angle derivative with respect to the half-offset with eq. (5.23) are used (second-order estimates). Again, processing in the S-wave phase reversal zone at the apex faces difficulties. Let us concentrate on the P-wave. The first-order estimates are much more stable accurately matching with the original velocities away from the traveltime apex. However, in the vicinity of the apex they are unstable and the second-order approach demonstrates better matching. On the contrary, second-order estimates are strongly unstable at the flanks

due to the vanishing wavefront curvature. In this sense, the approaches are complementary to each other. We expect that observed velocity uncertainties caused by the inaccuracy of the attribute values can be compensated by an approach where attributes from adjacent central midpoints are jointly involved.

5.7 Discussion

We have described and applied polarization-consistent stacking as an extension of the conventional three-parameter CRS method. However, the idea of stacking multicomponent traces along the traveltimes, itself, is very general. Various multidimensional and -parameter processing techniques could benefit from such an extension, e.g., finite-offset CRS and converted-waves CRS. Enhancement of prestack multicomponent data may be organized as partial CRS (Baykulov and Gajewski, 2009) in terms of the polarization-consistent stacking with preliminary extracted polarization and wavefront attributes. The polarization attributes have a potential for P- and S-waves filtering in the prestack domain as well. Due to the same property of the polarization angle derivatives, ν_{x_m} and ν_h, to coincide in the case of diffractions they have a potential to be utilized for diffraction separation, in addition to the wavefront curvature attributes (see Dell and Gajewski, 2011).

The determination of the wavefront and polarization attributes by stacking in the phase reversal zone, such as an S-wave apex, is difficult. Analogues problems would arise in applications to edge diffractions and passive data where the phase reversals take place for P-waves as well. A possible solution may be an adapting of the stacking algorithm for rapidly changing amplitudes by using additional weighting (e.g., Fomel, 2009; Dell et al., 2018). Another important limitation we haven't addressed so far is an effect of the free surface on the retrieved polarizations. Surely, the wave conversion phenomenon should be taken into account for field data processing. It becomes crucial for the subsequent applications of the polarization attributes. However, this requirement doesn't apply to the data preconditioning itself at least for P-waves and subcritical emergence of S-waves. Further work needs to be done also to competitively compare miscellaneous polarization approximations, including higher order extensions, for adapting the presented method to larger offsets and non-hyperbolic events.

We have tested a pragmatic approach for the attribute determination which comprises a sequence of three-parameter searches. There are other options too. For instance, a search in the six-dimensional space spanned by both polarization and wavefront attributes is one of them. Another potential approach is a refinement of the wavefront attributes by the multicomponent semblance optimization. When the surface-velocity model is homogeneous and known, the polarization angle derivatives ν_{x_m} and ν_h are fully described by the wavefront attributes α_0, K_N, and K_{NIP}, as shown in eq. (5.18). In this case, the full six-dimensional attribute space degenerates to a four-dimensional one spanned by three wavefront attributes, α_0, K_N, K_{NIP}, and one polarization attribute, ν_0.

Polarization-consistent stacking and the concept of the local polarization, introduced in this paper, are reasonable for anisotropy as well. However, the interpretation of the polarization derivatives and the subsequent processing steps must be revised. We emphasize that polarization and its derivatives with respect to the midpoint coordinate and the half-offset very well fit into the concept of wavefront attributes in anisotropic media (Vanelle

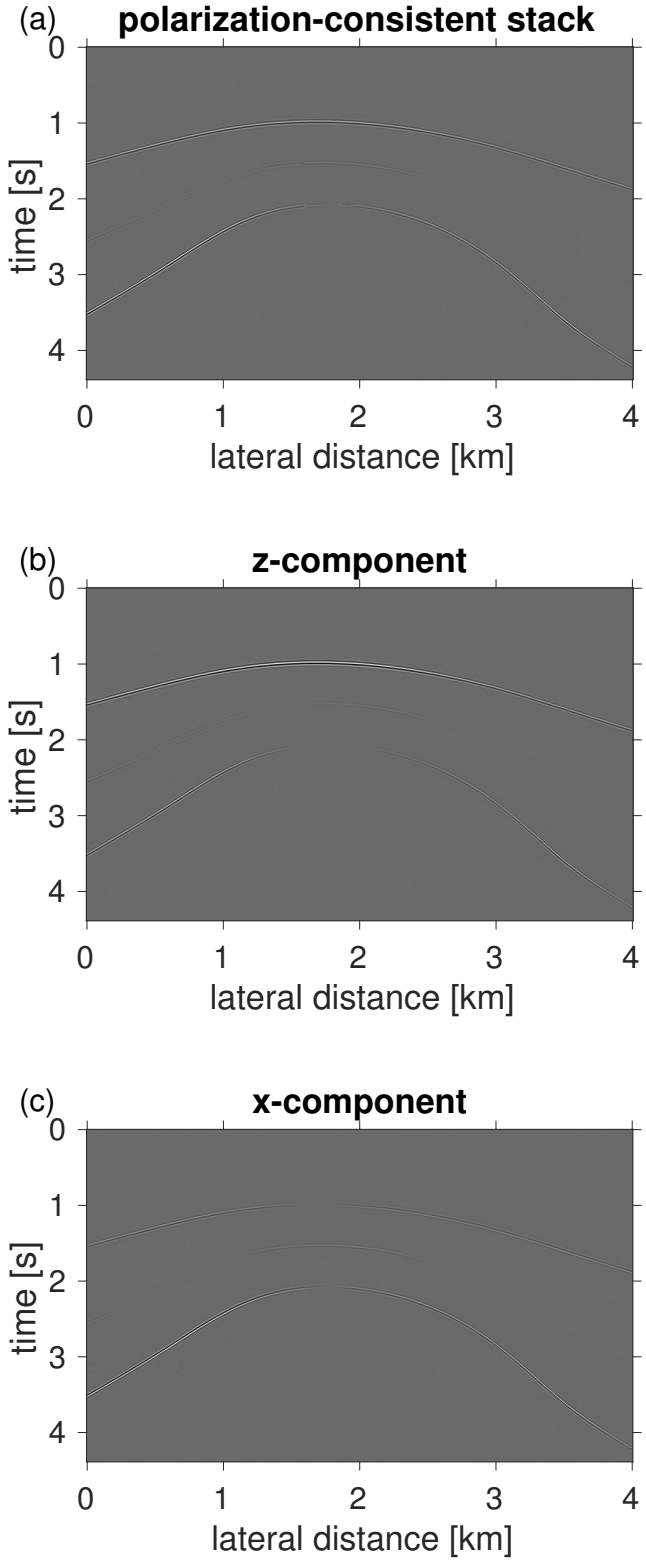

Figure 5.11: Enhanced zero-offset sections. Component sections (b) and (c) were derived with the pixel-by-pixel projection of the polarization-consistent stack (a) onto the z- and x-axes, respectively, with the help of the polarization angle section (Fig. 5.10b).

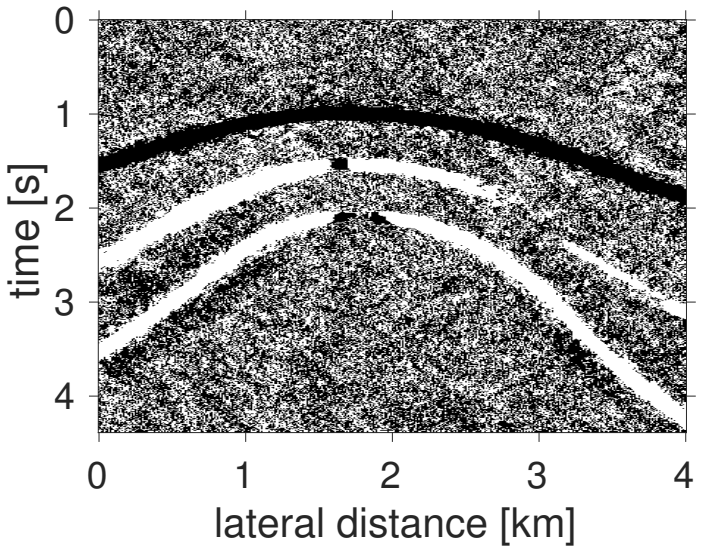

Figure 5.12: Result of the attributes-based arrival separation. Black pixels were identified as P-wave and white ones as S-wave.

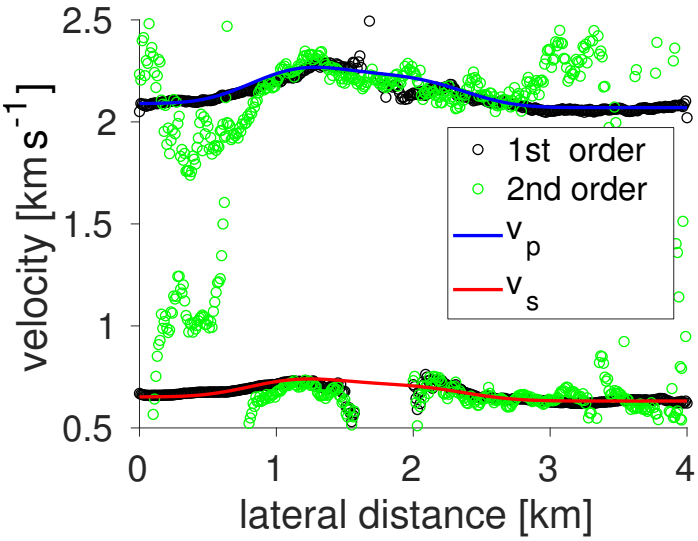

Figure 5.13: Retrieved acquisition line compressional and shear velocities compared to the original ones. Black circles display the first-order estimates using horizontal slowness and central polarization angle. Green circles display the second-order estimates using NIP-wave curvature attribute and polarization angle derivative with respect to the half-offset.

et al., 2018). Similarly to the isotropic case, the wavefront attributes together with the polarization attributes could be utilized for anisotropic surface-velocity model building. This enables a retrieval of initial conditions for the backpropagation with kinematic and dynamic ray tracing, which can be considered as input data for depth inversion. Subsurface model building could also benefit from constraining the elastic parameters at the acquisition line. Methods of polarization and slowness inversion for the local density-scaled stiffness tensor already exist (see Dewangan and Grechka, 2003; Tsvankin and Grechka, 2011). Obviously, one central midpoint and a single arrival are not sufficient to build a general stiffness tensor. Even reflections from multiple interfaces within a geological formation, picked all along the acquisition line, contain rather limited slowness information. Nevertheless, diffractions and microseismic events, since they have better illumination, may cover a part of the slowness surface sufficient for the inversion.

5.8 Conclusions

We have presented a polarization-consistent approach for stacking multicomponent data. It is formulated as an extension of the conventional common-reflection-surface method. The vertical and horizontal components are simultaneously stacked along the traveltimes computed using wavefront attributes. Contribution of a single wavefield component to the total stacked section is controlled by continuously changing polarization. Both wavefront and polarization attributes are automatically picked during a multicomponent semblance optimization. The polarization-consistent stack section is subsequently projected producing enhanced single component zero-offset sections.

We have introduced a concept of local polarization. Local approximations of polarization vector are described by a set of additional parameters. With regard to the multicomponent common-reflection-surface in 2D these new polarization attributes are central polarization angle and first-order derivatives of the polarization angle with respect to the midpoint and half-offset coordinates. The polarization angle derivatives can be interpreted in terms of the normal-incidence-point and normal waves. We have proved this for isotropic media by considering a polarization analogue of the NIP-wave theorem. A potential of using the polarization attributes has been demonstrated by some immediate applications, namely, utilizing them for the P- and S-waves separation and building of P- and S-waves velocities at the acquisition line.

The introduced polarization-consistent stacking has been successfully applied to 2D synthetic multicomponent diffraction data. The local polarization attributes have been determined by the multicomponent semblence optimization. The signal to noise ratio in the projected sections has been noticeably enhanced comparing to the prestack zero-offset sections. We have also utilized the wavefront and polarization attributes for the P- and S-waves identification and surface-velocities model building. The different arrivals have been successfully identified and the heterogeneous P- and S-wave velocities retrieved from a single diffraction have a good match with the synthetic model. Application to synthetic data has clearly demonstrated the capability of the proposed method to process and image the multicomponent data.

Acknowledgments

This work was carried out within the framework of the project by the Federal Ministry for Economic Affairs and Energy of Germany (project number 03SX427B). The authors appreciate the support of the Wave Inversion Technology (WIT) Consortium and sincerely thank the Applied Seismic Group of Hamburg University for the assistance and the fruitful discussions. The synthetic data were generated with Seismic Unix.

6 Conclusions

Wavefront attributes, including curvature matrices of the eigenwaves, contain fundamental information on the wavefront properties. Furthermore, the wavefront curvature being related to the geometrical spreading of waves and at the same time determined by kinematics is a unique physical quantity.

That is why the wavefront attributes definitely deserve a close attention of applied geophysicists. In this thesis, I established only a few possible applications of the zero-offset wavefront attributes. Undoubtedly, the zero-offset and the finite-offset wavefront attributes will find many other applications, especially with advances in the technology for their accurate extraction.

First, I developed a new well-conditioned method for macro-velocity model building. It is based on kinematic and dynamic ray tracing of normal-incidence-point waves and diffractions in reverse time and on minimizing geometrical spreading. The waves simultaneously focus, which updates the fictitious source positions and the velocity model. The input for the inversion are traveltime, the horizontal component of slowness vector, and the wavefront curvature. The new objective functional contains a single physical quantity and depends only on the velocity model. If compared to the conventional wavefront tomography based on data fitting, this reformulation by its smaller inversion matrix leads to favorable properties of the inverse problem such as relaxing regularization. Additionally, a reduced amount of tuning parameters in the objective functional allows one to easier obtain reproducible results. This concerns, e.g., weighting different physical parameters since the proposed functional comprises only a focusing measure. I tested the proposed tomographic inversion on the synthetic data comprising a salt body. The retrieved tomographic image highly correlates with the synthetic model. The end-points of normal-incidence-rays propagated into the final model constitute the layer boundaries. I further applied my approach to complex marine data. The inverted model was used in a common-shot depth migration. In the migrated section, I observed a clean and continuous image of the top of salt and well focused steep faults. In both synthetic and field data examples, I did not use any regularization terms, which confirmed the well-conditioned behavior of the new formulation.

In order to conceive anisotropic velocity model building by ray focusing in the same manner, I developed the first-order ray perturbation theory in the local wavefront-orthonormal coordinates. This is an alternative approach to Fréchet derivatives of ray and slowness vector with respect to the density normalized elastic moduli. In contrast to the standard Cartesian coordinates formulation, it has a reduced number of equations but requires additional tracing of the wavefront-orthonormal basis.

Next, I proposed an approach for identification and separation of wave modes in the data domain. This method allows one to distinguish seismic events between point diffractions, edge diffractions, and reflections. It is a generalization of the scalar curvature technique to an arbitrarily oriented and curved edge in 3D heterogeneous media, including anisotropy. The identification is performed by analyzing a matrix, which contains residuals of the wave-

front curvature matrices. Its determinant vanishes for both kinds of diffractions. Consequentially inspecting its elements, however, provides a tool to distinguish between point and edge diffractions. Using this residual wavefront curvature matrix, I also designed an algorithm to sort traces into specific groups in a way that rays of a single group focus at a particular point on the edge. This implies that the 3D edge diffraction can be focused, kinematically and dynamically, similarly to the point diffraction. The identification criterion and the methodology for receiver grouping were successfully verified with synthetic examples comprising an isotropic heterogeneous and an anisotropic model. The wavefront attributes extracted from the realistic SEG/EAGE dataset allowed for the edge diffraction identification under condition of moderate model heterogeneity even in the case of strong uncorrelated noise.

Finally, I formulated an extension of the conventional common-reflection-surface method to multicomponent data introducing a concept of local polarization. Local approximation of polarization is described by a set of new attributes. They are central polarization angle and first-order derivatives of the polarization angle with respect to the midpoint and half-offset coordinates. The polarization angle derivatives can be interpreted in terms of the eigenwave curvatures. The polarization-consistent stacking was successfully applied to a synthetic elastic diffraction data. This means that the local polarization attributes were determined by the multicomponent semblance optimization and the signal-to-noise ratio in the projected sections was noticeably enhanced. I successfully utilized the wavefront and the polarization attributes of a single elastic diffraction for the P- and S-waves identification and for the building of P- and S-velocities at the acquisition surface.

7 Outlook

Kinematic and/or dynamic ray focusing

Point diffractions can be focused in reverse time not only by the dynamic ray focusing, but also kinematically by minimizing distances between endpoints of rays, which belong to the same subsurface locations (Bauer et al., 2019). This requires slight modifications of the code and additional computing of the kinematic Fréchet derivatives. Apparently, in the dynamic ray focusing a single ray constraints the velocity model stronger than in the kinematic ray focusing since the curvature is related to the ray tube, i.e., to some vicinity of the ray. However, in the kinematic approach mutual focusing is imposed and no curvatures are needed, which may be important when they are determined unreliably. Finally, both objective functionals can be applied simultaneously.

3D dynamic ray focusing

The objective functional of dynamic ray focusing introduced in this work can easily be generalized to the 3D case. For doing this, it is necessary to define an acquisition-normalized matrix

$$Q(t) = Q^d(t)Q^d(t_i)^{-1},$$

where Q^d is the first dynamic ray tracing matrix of the registered wave (NIP-wave or diffraction), and t_i is the registered travel time. Indeed, this matrix is acquisition normalized:

$$Q(t_i) = I.$$

Let us define a second normalized dynamic ray tracing matrix:

$$P(t) = P^d(t)Q^d(t_i)^{-1},$$

where P^d is the second dynamic ray tracing matrix of the registered wave. Its initial condition (for the reverse propagation) is simply given by the wavefront curvature matrix obtainable from the measurements:

$$P(t_i) = P^d(t_i)Q^d(t_i)^{-1} = M^d(t_i).$$

Since the dynamic ray tracing system is linear, it is satisfied with the acquisition normalized matrices, Q and P. Therefore, the 4×4 propagator formalism can be applied to construct them. Furthermore, geometrical spreading computed using the acquisition normalized matrix vanishes together with the geometrical spreading of the registered wave:

$$\det Q(t) = \frac{\det Q^d(t)}{\det Q^d(t_i)},$$

which forms the basis of the dynamic ray focusing.

Edge diffractions in focusing tomography

In 2D, traveltime responses of point and edge diffractions are equivalent. However in 3D, one should distinguish and treat them differently to carefully account for such objects as faults, highly curved folds, fractures, and pinch-outs. Particularly, this is crucial for velocity model building by the kinematic ray focusing. For point diffractions, this method requires tagging of individual diffractions. For edge diffractions, it is necessary to additionally group receivers in a special way that they are back projected to single points on the edge. The method of receiver grouping based on the wavefront curvatures is outlined in this thesis.

Microseismic localization and velocity model building

Simultaneous microseismic localization and velocity model building is closely related to global seismology. For such acquisitions, there is a great challenge of determining the unknown source excitation time. A set of wavefront attributes can also be extracted from the passive seismic data (Schwarz et al., 2016) similarly as from the reflections and diffractions. Passive-seismic wavefront tomography with the source time as an additional unknown has a potential to solve the problem of determination of the source excitation time (Diekmann et al., 2019). However, the focusing methodology is also very promising, especially regarding the reduction of the number of unknowns.

Anisotropic model building

Seismic anisotropy in the subsurface is a well documented fact. It has either macroscopic or microscopic origin. Macroscopically, it is caused by thin layering of sediments or by presence of oriented fracturing. On the micro scale, seismic anisotropy is due to the intrinsic crystal properties. Concerning the inversion of anisotropic elastic parameters, a tremendous increase in the number of unknowns inevitably leads to a greater uncertainty. Therefore, the anisotropic inversion remains a big challenge. At the current state, the wavefront tomography is formulated only for the isotropic inversion. Even in this case, calculation of the Fréchet derivatives looks cumbersome and the data/unknowns ratio is low. Therefore, I expect generalization to anisotropy to be a non-trivial problem. To reduce the number of Fréchet derivatives and to increase stability, I suggest to apply the reverse time strategy as well. If a near-surface model is available, one can extract the same input for the dynamic ray focusing from the wavefront attributes in the most general anisotropic case (Vanelle et al., 2018). Moreover, the objective functional together with the methodology of computing the gradient, can be used to conceive inversion for anisotropic models. However, kinematic and dynamic ray tracing will require an adjustment. Additionally, the perturbed matrix of dynamic ray tracing needs to be reformulated in terms of perturbations of the anisotropic parameters.

Polarization-consistent stacking in anisotropic media

Polarization-consistent stacking and the concept of local polarization are reasonable for anisotropy as well. However, the interpretation of polarization derivatives with the NIP-

wave theorem has to be revised. Polarization and its derivatives with respect to the midpoint coordinate and the half-offset very well fit into the concept of wavefront attributes in anisotropic media (Vanelle et al., 2018). Similarly to the isotropic case, the wavefront attributes together with the polarization attributes could be utilized for building the elastic moduli at the acquisition-surface. Methods of polarization and slowness inversion for the local density-scaled stiffness tensor already exist (see Dewangan and Grechka, 2003; Tsvankin and Grechka, 2011). Obviously, one central midpoint and a single arrival are not sufficient to build a general stiffness tensor. Even reflections from multiple interfaces within a geological formation, picked all along the acquisition line, contain rather limited slowness information. Nevertheless, diffractions or microseismic events may cover a sufficient part of the slowness surface due to their superior illumination.

A Appendix for the Chapter 2

A.1 Illustrating the objective function for a single pick in a homogeneous medium

The illustration for a homogeneous medium gains some intuition on how the method works. Let us assume we have measured one-way traveltime t and the curvature attribute M in the homogeneous medium with velocity v_0. First, we compute the time-reversal propagator for a trial velocity model:

$$\Pi(0,t) = \Pi^{-1}(t,0) = \begin{pmatrix} 1 & -v^2 t \\ 0 & 1 \end{pmatrix}. \tag{A.1}$$

Next, we consider the objective function comprising the elements of the time-reversal propagator and the curvature attribute:

$$J(v) = \frac{1}{2}\left(Q^{(1)}(0,t) + Q^{(2)}(0,t)M\right)^2. \tag{A.2}$$

Since $t = Rv_0^{-1}$ and $M = (v_0 R)^{-1}$, it becomes

$$J(v) = \frac{1}{2}\left(1 - \frac{v^2}{v_0^2}\right)^2 \tag{A.3}$$

with a unique positive minimum at $v = v_0$.

A.2 On the initial condition for the perturbed ray-centered slowness

The horizontal slowness of the emerging ray p_x is determined from data. It is fixed in the focusing approach. The perturbed eikonal equation considered at the point of arrival

$$(\mathbf{p}, \triangle\mathbf{p}) = -\frac{\triangle v}{v^3} \tag{A.4}$$

reveals components of the perturbed slowness vector $\triangle\mathbf{p}$ in the local ray-centered coordinates. Transformation from the Cartesian to the ray-centered coordinate system

$$\begin{pmatrix} -\frac{\triangle v}{v^2} \\ p \end{pmatrix} = \begin{pmatrix} vp_x & vp_z \\ -vp_z & vp_x \end{pmatrix} \begin{pmatrix} 0 \\ \triangle p_z \end{pmatrix} \tag{A.5}$$

may be considered as a linear system of equations with respect to the perturbed ray-centered slowness p and the Cartesian component $\triangle p_z$. Its determinant, equal to vp_z, vanishes if the reference ray is tangent to the registration line. Otherwise,

$$p = -\frac{\triangle v}{v^2}\frac{p_x}{p_z}. \tag{A.6}$$

A.3 The adjoint-state formulation for the Fréchet derivative of the objective functional

We will derive the adjoint-state method formulation in a unified way (e.g., Plessix, 2006; Chavent, 2010) to illustrate how the adjoint-state variables λ_i^Q, λ_i^P are introduced as solutions of the adjoint dynamic ray tracing system.

Let us think of $\lambda_i^Q(t)$, $\lambda_i^P(t)$ as a set of functions that are undefined so far. We introduce an auxiliary functional $\overline{\triangle J}$ by taking a dot product of the perturbation theory system of equations 2.13 with a vector of elements λ_i^Q, λ_i^P, integrating resulting scalar over the corresponding time interval, and summing the quantities for all picks:

$$\overline{\triangle J} = \sum_{i=1}^{N_{data}} \int_{t_i}^{0} dt \left(- \begin{pmatrix} \lambda_i^Q & \lambda_i^P \end{pmatrix} \frac{d}{dt} \begin{pmatrix} \triangle Q_i \\ \triangle P_i \end{pmatrix} + \begin{pmatrix} \lambda_i^Q & \lambda_i^P \end{pmatrix} S \begin{pmatrix} \triangle Q_i \\ \triangle P_i \end{pmatrix} + \begin{pmatrix} \lambda_i^Q & \lambda_i^P \end{pmatrix} \triangle S \begin{pmatrix} Q_i \\ P_i \end{pmatrix} \right). \tag{A.7}$$

This is the zero functional since the perturbation theory system is satisfied. We integrate it by parts in order to isolate dynamic perturbations as multipliers:

$$\overline{\triangle J} = - \sum_{i=1}^{N_{data}} (\lambda_i^Q \triangle Q_i) \Big|_{t=t_i}^{t=0} - \sum_{i=1}^{N_{data}} (\lambda_i^P \triangle P_i) \Big|_{t=t_i}^{t=0} +$$

$$\sum_{i=1}^{N_{data}} \int_{t_i}^{0} dt \left(\frac{d}{dt} \begin{pmatrix} \lambda_i^Q & \lambda_i^P \end{pmatrix} \begin{pmatrix} \triangle Q_i \\ \triangle P_i \end{pmatrix} + \begin{pmatrix} \lambda_i^Q & \lambda_i^P \end{pmatrix} S \begin{pmatrix} \triangle Q_i \\ \triangle P_i \end{pmatrix} + \begin{pmatrix} \lambda_i^Q & \lambda_i^P \end{pmatrix} \triangle S \begin{pmatrix} Q_i \\ P_i \end{pmatrix} \right). \tag{A.8}$$

Adding the auxiliary zero functional, $\overline{\triangle J}$, to the derivative of the objective functional 2.7 expressed though the derivatives of the state variables,

$$\triangle J = \sum_{i=1}^{N_{data}} Q_i(0) \triangle Q_i(0), \tag{A.9}$$

doesn't change its value: $\triangle J = \triangle J + \overline{\triangle J}$. However, this representation makes possible to define the adjoint-state variables in order to get an alternative formulation for the gradient. Namely, we choose them to cancel out the quotients of the dynamic perturbations. Indeed, the adjoint-state variables defined with a system

$$\frac{d}{dt} \begin{pmatrix} \lambda_Q \\ \lambda_P \end{pmatrix} = -S^T \begin{pmatrix} \lambda_Q \\ \lambda_P \end{pmatrix} \tag{A.10}$$

eliminate two terms in the integrand of equation A.8. As was explained in the main body of the paper, dynamic perturbations equal zero at the arrival time: $\triangle Q_i(t_i) = 0$ and $\triangle P_i(t_i) = 0$. Therefore, to remove the remaining external terms, we have to impose initial conditions on the other side, in depth: $\lambda_i^Q(0) = Q_i(0)$, $\lambda_i^P(0) = 0$. Thus, the adjoint-state vector is a result of forward propagation with the adjoint dynamic ray tracing system A.10 and initial conditions containing the back-propagated geometrical spreading. The remainder represents the Fréchet derivative of the objective functional:

$$\triangle J = \sum_{i=1}^{N_{data}} \int_{t_i}^{0} \begin{pmatrix} \lambda_i^Q & \lambda_i^P \end{pmatrix} \triangle S \begin{pmatrix} Q_i \\ P_i \end{pmatrix} dt. \tag{A.11}$$

The operator of the dynamic ray tracing system 2.2 is not self-adjoint. However, its matrix has a special property related to the symplecticity of the propagator (e.g., Červený, 2001):

$$JS^T + SJ = 0, \qquad J = \begin{pmatrix} 0 & 1 \\ -1 & 0 \end{pmatrix}. \tag{A.12}$$

We use it to transform the matrix of the adjoint system A.10: $-S^T = J^{-1}SJ$. Consequently, the adjoint system of differential equations coincides with the initial one up to permutation of variables and change of a sign:

$$\frac{d}{dt} J \begin{pmatrix} \lambda_Q \\ \lambda_P \end{pmatrix} = SJ \begin{pmatrix} \lambda_Q \\ \lambda_P \end{pmatrix}. \tag{A.13}$$

Solving it with the dynamic ray tracing propagator and using the chain rule for the propagator, we get an expression for computing the adjoint vector at $\tilde{t} < t$:

$$\begin{pmatrix} \lambda_Q\left(\tilde{t}\right) \\ \lambda_P\left(\tilde{t}\right) \end{pmatrix} = J^T \Pi\left(\tilde{t}, 0\right) J \begin{pmatrix} Q(0) \\ 0 \end{pmatrix} = \Pi^{-1T}\left(\tilde{t}, 0\right) \begin{pmatrix} Q(0) \\ 0 \end{pmatrix} = \Pi^{-1T}\left(\tilde{t}, t\right) \Pi^T\left(0, t\right) \begin{pmatrix} Q(0) \\ 0 \end{pmatrix} = \tag{A.14}$$

$$Q(0)\Pi^{-1T}\left(\tilde{t}, t\right) \begin{pmatrix} Q^{(1)}(0,t) \\ Q^{(2)}(0,t) \end{pmatrix}. \tag{A.15}$$

B Appendix for the Chapter 3

B.1 First-order derivatives of the polarization vector

After determining an eigenvalue $v^2(\mathbf{x},\mathbf{n})$ and the corresponding eigenvector $\mathbf{g}(\mathbf{x},\mathbf{n})$, the Christoffel system may be considered as an identity valid for different $\mathbf{x}$ and $\mathbf{n}$:

$$a_{ijkl}(\mathbf{x})n_j n_k g_l(\mathbf{x},\mathbf{n}) = v(\mathbf{x},\mathbf{n})^2 g_i(\mathbf{x},\mathbf{n}), \qquad i=1,2,3. \tag{B.1}$$

Differentiating it with respect to the Cartesian coordinates leads to an inhomogeneous algebraic system with respect to the polarization derivatives:

$$(a_{ijkl}n_j n_k - v^2\delta_{il})\frac{\partial g_l}{\partial x_m} = \frac{\partial v^2}{\partial x_m}g_i - \frac{\partial a_{ijkl}}{\partial x_m}n_j n_k g_l, \qquad i,m=1,2,3. \tag{B.2}$$

δ_{ij} denotes the Kronecker delta. The symmetric matrix of this system comes from the Christoffel equation and has, therefore, zero determinant. The null-space of adjoint system is determined with the eigenvector $\mathbf{g}$, which is orthogonal to the right-hand side of the system. Therefore, the system (B.2) has solutions. Note that we are looking for the polarization derivatives that are orthogonal to the unit vector $\mathbf{g}$ and this way belong to the secondary eigenspace. To find their projections onto the secondary eigenvectors, we evaluate the dot product of eq. (B.2) with a secondary eigenvector $\mathbf{g}^{(\alpha)}$ ($\alpha=1,2$). Using the Christoffel equation written for the secondary eigenvectors

$$a_{ijkl}n_j n_k g_l^{(\alpha)} = (v^{(\alpha)})^2 g_i^{(\alpha)}, \qquad i=1,2,3, \qquad \alpha=1,2, \tag{B.3}$$

we get

$$\frac{\partial g_i}{\partial x_j}g_i^{(\alpha)} = \hat{V}_{ji}g_i^{(\alpha)}\frac{v^2}{v^2-(v^{(\alpha)})^2}, \qquad j=1,2,3, \qquad \alpha=1,2, \tag{B.4}$$

where the 3×3 matrix

$$\hat{V}_{ij} = \frac{\partial a_{jklm}}{\partial x_i}p_k p_l g_m, \qquad i,j=1,2,3, \tag{B.5}$$

is introduced. Eventually, with the help of the 3×3 matrix

$$B_{ij} = B_{ji} = v^2\sum_{\alpha=1}^{2}\frac{g_i^{(\alpha)}g_j^{(\alpha)}}{v^2-(v^{(\alpha)})^2}, \qquad i,j=1,2,3, \tag{B.6}$$

the polarization derivatives are formulated as follows:

$$\frac{\partial g_i}{\partial x_j} = \sum_{\alpha=1}^{2}\frac{\partial g_k}{\partial x_j}g_k^{(\alpha)}g_i^{(\alpha)} = (B\hat{V}^T)_{ij}, \qquad i,j=1,2,3. \tag{B.7}$$

Analogously, differentiating eq. (B.1) with respect to the components of the wavefront normal leads to another inhomogeneous algebraic system for the corresponding polarization derivatives:

$$(a_{ijkl}n_jn_k - v^2\delta_{il})\frac{\partial g_l}{\partial n_m} = \frac{\partial v^2}{\partial n_m}g_i - (a_{imkl} + a_{ikml})n_k g_l, \qquad i,m = 1,2,3. \tag{B.8}$$

Again, the determinant is zero and the right-hand side is orthogonal to the eigenvector $\mathbf{g}$. Evaluating the dot product of eq. (B.8) with the secondary eigenvectors, we get

$$\frac{\partial g_i}{\partial n_j}g_i^{(\alpha)} = \hat{W}_{ji}g_i^{(\alpha)}\frac{v}{v^2 - (v^{(\alpha)})^2}, \qquad j = 1,2,3, \qquad \alpha = 1,2, \tag{B.9}$$

where the 3×3 matrix

$$\hat{W}_{ij} = (a_{ijkl} + a_{ikjl})g_k p_l, \qquad i,j = 1,2,3, \tag{B.10}$$

is introduced. In dynamic ray tracing, we need derivatives with respect to the slowness vector components rather than with respect to the wavefront normal components. Polarization components are, however, homogeneous functions of zero degree with respect to the normal vector. Using the chain rule

$$\frac{\partial g_i}{\partial p_j} = \frac{\partial g_i}{\partial n_k}\frac{\partial n_k}{\partial p_j} = v\frac{\partial g_i}{\partial n_j} - v^2\frac{\partial g_i}{\partial n_k}n_k p_j, \qquad i,j = 1,2,3, \tag{B.11}$$

and the Euler's theorem for homogeneous functions, $\frac{\partial g_i}{\partial n_k}n_k = 0$ in this case, we conclude that the derivatives are proportional. Finally,

$$\frac{\partial g_i}{\partial p_j} = v\frac{\partial g_i}{\partial n_j} = v\sum_{\alpha=1}^{2}\frac{\partial g_k}{\partial n_j}g_k^{(\alpha)}g_i^{(\alpha)} = (B\hat{W}^T)_{ij}, \qquad i,j = 1,2,3. \tag{B.12}$$

For the perturbation by anisotropic model, we need derivatives of the polarization vector with respect to the normalized elastic moduli. We again consider the Christoffel eigenvalues and eigenvector problem

$$a_{ijkl}n_jn_kg_l = v^2g_i, \qquad i = 1,2,3. \tag{B.13}$$

However, since we are going to compute derivatives with respect to single components $a_{\alpha\beta\gamma\delta}$, we have to relax the stiffness tensor symmetries. Which means that for the eigenvalue we have to use exactly as it follows from eq. (B.13), $v^2 = a_{ijkl}n_jn_kg_ig_l$, without transposing the indices. Otherwise, one could end up with erroneous consequences. Differentiating the Christoffel equation in a form relating the elastic moduli and the wavefront normal and polarization components

$$a_{ijkl}n_jn_kg_l = a_{mjkl}n_jn_kg_mg_lg_i, \qquad i = 1,2,3, \tag{B.14}$$

with respect to a component $a_{\alpha\beta\gamma\delta}$ leads to a final inhomogeneous algebraic system:

$$(a_{ijkl}n_jn_k - v^2\delta_{il})\frac{\partial g_l}{\partial a_{\alpha\beta\gamma\delta}} = g_\alpha n_\beta n_\gamma g_\delta g_i - \delta_{i\alpha}n_\beta n_\gamma g_\delta, \qquad i,\alpha,\beta,\gamma,\delta = 1,2,3. \tag{B.15}$$

Again, the determinant is zero and the right-hand side is orthogonal to the eigenvector $\mathbf{g}$. Computing the dot product of eq. (B.15) with the secondary eigenvectors gives

$$\frac{\partial g_i}{\partial a_{\alpha\beta\gamma\delta}} g_i^{(\varepsilon)} = g_\alpha^{(\varepsilon)} p_\beta p_\gamma g_\delta \frac{v^2}{v^2 - (v^{(\varepsilon)})^2}, \qquad \alpha, \beta, \gamma, \delta = 1, 2, 3. \tag{B.16}$$

Eventually,

$$\frac{\partial g_i}{\partial a_{\alpha\beta\gamma\delta}} = \sum_{\varepsilon=1}^{2} \frac{\partial g_j}{\partial a_{\alpha\beta\gamma\delta}} g_j^{(\varepsilon)} g_i^{(\varepsilon)} = B_{i\alpha} p_\beta p_\gamma g_\delta, \qquad i, \alpha, \beta, \gamma, \delta = 1, 2, 3. \tag{B.17}$$

Note, it is crucial that the eigenvalues are assumed isolated. The given formulas are not valid in the case of S-wave degeneracy and may work unstable in cases close to the degeneracy.

B.2 Initial conditions for the kinematic perturbations

We will keep the initial ray point fixed since such a condition takes place in seismic inversion with back propagation we are working on (Znak et al., 2019).

As previously mentioned, physically reasonable initial conditions for the perturbations of ray and slowness vector are restricted with the perturbation of eikonal equation (3.44). Particularly, if the initial point of the ray is kept fixed, $\triangle\mathbf{x}(t_0) = 0$ and the equation for perturbed eikonal at the initial time t_0 reduces to

$$(\triangle\mathbf{p}, \mathbf{u}) = -\frac{\triangle v}{v} \tag{B.18}$$

imposing a restriction on the projection of the initial slowness vector perturbation. This projection to the direction of the unperturbed ray is determined with the anisotropic model perturbation at the initial ray point.

Thus, choosing remaining components orthogonally to the unperturbed ray is an option available in formulation of this perturbation problem. Equivalently, this option may be formulated in terms of the wavefront-orthonormal projections of the slowness vector perturbation, $\triangle p_1^q$ and $\triangle p_2^q$. Since $\triangle n(t_0) = (\triangle\mathbf{x}(t_0), \mathbf{e}_n(t_0)) = 0$ for the problem with fixed initial ray point, the wavefront-orthonormal projections are equal to the wavefront-orthonormal perturbations at the initial time (see eqs 3.54 and 3.56):

$$q_\alpha = \triangle x_\alpha^q = 0, \qquad p_\alpha^q = \triangle p_\alpha^q, \qquad \alpha = 1, 2. \tag{B.19}$$

Unit vectors in the ray-orthogonal plane $\mathbf{u}_1^\perp$ and $\mathbf{u}_2^\perp$ may be defined with the wavefront-orthonormal basis as follows:

$$\mathbf{u}_\alpha^\perp = \frac{v\mathbf{e}_\alpha - u_\alpha^q \mathbf{e}_n}{\sqrt{v^2 + (u_\alpha^q)^2}}, \qquad \alpha = 1, 2. \tag{B.20}$$

Using eq. (3.49), we can relate the ray-orthogonal projections and the wavefront-orthonormal perturbations at the initial time:

$$(\triangle\mathbf{p}, \mathbf{u}_\alpha^\perp) = \frac{v^3 p_\alpha^q + u_\alpha^q (\triangle v - v u_\beta^q p_\beta^q)}{v^2 \sqrt{v^2 + (u_\alpha^q)^2}}, \qquad \alpha = 1, 2. \tag{B.21}$$

When no model perturbation is present at the initial ray point, the projection $(\triangle\mathbf{p}, \mathbf{u})$ has to vanish. For the isotropic media, this statement reflects the fact that the perturbation of the constant length vector, $\mathbf{u} = \mathbf{p}$, is orthogonal to this vector. In the anisotropic case, it corresponds to another fact that the ray velocity vector is orthogonal to the slowness vector surface.

When the anisotropic model is perturbed at the initial point of the ray, more options are available. For instance, one could be interested in a perturbed ray that emerges with the same direction of the wavefront normal as the reference one. In this case, perturbation of the slowness vector is directed along the normal and $p_1^q = p_2^q = 0$. Perturbation in the anisotropic model affects dilation of the slowness vector in this case: $(\triangle\mathbf{p}, \mathbf{e}_n) = -\frac{\triangle v}{v^2}$.

In practice, there is a perturbation problem formulated provided that two Cartesian components of the slowness vector are fixed at the acquisition surface. Such a formulation arises in seismic inversion with back propagation, when the slowness vector components are measured at the receiver side and considered fixed during inversion.

Let us assume that Cartesian components of the slowness vector, p_1 and p_2, are fixed. To determine the initial values of the wavefront-orthonormal perturbations p_1^q and p_2^q, we consider a transformation from the Cartesian to the wavefront-orthonormal coordinates applied to the slowness vector perturbation:

$$\begin{pmatrix} p_1^q \\ p_2^q \\ -\frac{u_\alpha^q p_\alpha^q}{v} - \frac{\triangle v}{v^2} \end{pmatrix} = \begin{pmatrix} e_{11} & e_{12} & e_{13} \\ e_{21} & e_{22} & e_{23} \\ vp_1 & vp_2 & vp_3 \end{pmatrix} \begin{pmatrix} 0 \\ 0 \\ \triangle p_3 \end{pmatrix}. \tag{B.22}$$

Regarding it as a linear algebraic system with respect to p_1^q, p_2^q, and $\triangle p_3$,

$$\begin{pmatrix} 1 & 0 & -e_{13} \\ 0 & 1 & -e_{23} \\ u_1^q & u_2^q & v^2 p_3 \end{pmatrix} \begin{pmatrix} p_1^q \\ p_2^q \\ \triangle p_3 \end{pmatrix} = \begin{pmatrix} 0 \\ 0 \\ -\frac{\triangle v}{v} \end{pmatrix}, \tag{B.23}$$

we conclude that its determinant represents the vertical component of ray velocity vector, u_3, and

$$p_\alpha^q = -\frac{e_{\alpha 3}}{v u_3}\triangle v, \quad \alpha = 1, 2, \qquad \triangle p_3 = -\frac{1}{v u_3}\triangle v. \tag{B.24}$$

In practice, we most likely deal with rays which are not tangent to the acqusition surface and $u_3 \neq 0$. However in anisotropic media, this may happen when horizontal slowness vector components are not zero, for slowness vectors corresponding to the horizontally extreme points of the slowness vector surface. It is an interesting example of peculiarity when the standard first-order perturbation approach fails due to a root dependency between the perturbed values and the parameter perturbations. Let us examine this peculiarity.

In isotropic media, tangent ray implies tangent slowness vector. It is impossible to turn the full length of the slowness vector into the acquisition-surface component of the slowness vector by an arbitrary velocity perturbation. It is allowed only on a greater slowness sphere. Subtracting the unperturbed eikonal equation from the perturbed one yields $\triangle p_3 = \pm\sqrt{-\frac{2\triangle v}{v^3}}$, which is real only for negative values of $\triangle v$.

Standard first-order expansion of the eikonal equation (3.5) with $a_{ijkl}^{(1)} = a_{ijkl} + \triangle a_{ijkl}$, $p_i^{(1)} = p_i + \delta_{i3}\triangle p_3$, and $u_3 = a_{3jkl} g_j g_k p_l = 0$ leads to an erroneous identity $\triangle a_{ijkl} g_j g_k p_i p_l =$

0, which additionally indicates that the perturbation series needs to be accurately specified. If we now consider the perturbation parameter ε for the elastic moduli, $a^{(1)}_{ijkl} = a_{ijkl} + \varepsilon\triangle a_{ijkl}$, we should substitute $p^{(1)}_i = p_i + \sqrt{\varepsilon}\delta_{i3}\triangle p_3$ according to the previous observations. Collecting terms with ε^0 again gives the unperturbed eikonal equation. Terms with $\varepsilon^{\frac{1}{2}}$ vanish due to $u_3 = 0$. Finally, collecting terms of the first-order yields consistent asymptotics:

$$\triangle p_3 = \pm\sqrt{-\frac{\sum\limits_{i,j,k,l=1}^{3}\triangle a_{ijkl}g_jg_kp_ip_l}{\sum\limits_{i,j=1}^{3}a_{3ij3}g_ig_j}} = \pm\sqrt{-\frac{2\triangle v}{v\sum\limits_{i,j=1}^{3}a_{3ij3}g_ig_j}}. \tag{B.25}$$

C Appendix for the Chapter 4

C.1 Derivation of the identification criterion of the edge diffraction by dynamic ray tracing

We consider an edge as a smooth naturally parameterized curve $\mathbf{x}_0(\sigma)$ in space and assume it has a nonzero curvature at the normal-incidence-point, $\sigma = \sigma_0$. The standard Frenet-Serret basis on the edge consists of tangent $\mathbf{t}$, normal $\mathbf{n}$, and binormal $\mathbf{b}$ (Figure C.1). We introduce ray-coordinates of the N- and NIP-wave, which are measured with respect to this basis. For the N-wave, the second ray-coordinate γ_2, shooting angle of the normal to the wavefront φ, is computed with respect to the normal of the edge in the edge-orthogonal plane:

$$\mathbf{e}_n^N(0,\varphi,\sigma) = \cos\varphi\mathbf{n}(\sigma) + \sin\varphi\mathbf{b}(\sigma). \tag{C.1}$$

Tracing rays from position $\mathbf{x}_N(0,\varphi,\sigma) = \mathbf{x}_0(\sigma)$ with initial wavefront normals $\mathbf{e}_n^N(0,\varphi,\sigma)$ yields a set of rays $\mathbf{x}_N(\tau,\varphi,\sigma)$, where the third ray-coordinate γ_3 is the length parameter of the edge. For the NIP-wave, the shooting position $\mathbf{x}_{NIP}(0,\varphi,\theta) = \mathbf{x}_0(\sigma_0)$ is fixed and the ray coordinates are the spherical angles φ defined in the same way as for the N-wave and θ, a complementary shooting angle out of the edge-orthogonal plane:

$$\mathbf{e}_n^{NIP}(0,\varphi,\theta) = \sin\theta(\cos\varphi\mathbf{n}(\sigma_0) + \sin\varphi\mathbf{b}(\sigma_0)) + \cos\theta\mathbf{t}(\sigma_0). \tag{C.2}$$

Ray tracing yields a set of rays $\mathbf{x}_{NIP}(\tau,\varphi,\theta)$. When $\sigma = \sigma_0$ and $\theta = \frac{\pi}{2}$, the initial conditions coincide, which leads to the common one-parametric family of rays:

$$\mathbf{x}_{NIP}(\tau,\varphi,\pi/2) = \mathbf{x}_N(\tau,\varphi,\sigma_0), \qquad \mathbf{p}_{NIP}(\tau,\varphi,\pi/2) = \mathbf{p}_N(\tau,\varphi,\sigma_0). \tag{C.3}$$

We adhere the dynamic ray tracing formulated in the wavefront-orthonormal coordinates (e.g., Červený, 2001). To find initial conditions for the dynamic ray tracing of NIP- and

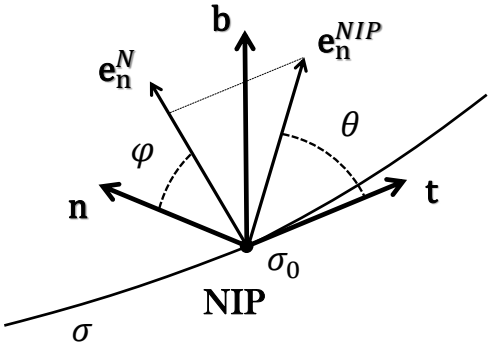

Figure C.1: NIP- and N-wave ray-coordinates measured with respect to the Frenet-Serret basis on the edge.

N-wave along the zero-offset ray, we first specify the wavefront-orthonormal basis at the initial moment of time:

$$\begin{aligned}
&\mathbf{e}_1(0) = \mathbf{e}_n^{NIP}(0,\varphi,\pi/2) = \mathbf{e}_n^{N}(0,\varphi,\sigma_0),\\
&\mathbf{e}_2(0) = \mathbf{t}(\sigma_0),\\
&\mathbf{e}_3(0) = [\mathbf{e}_2(0), \mathbf{e}_1(0)],
\end{aligned} \tag{C.4}$$

where brackets are used for the vector product. Further, we compute projections of the ray and slowness derivatives onto the wavefront-orthonormal basis

$$Q_{ij} = \left(\frac{\partial \mathbf{x}}{\partial \gamma_j}, \mathbf{e}_i\right), \qquad P_{ij} = \left(\frac{\partial \mathbf{p}}{\partial \gamma_j}, \mathbf{e}_i\right), \qquad i,j = 2,3. \tag{C.5}$$

at initial moment of time.

The NIP-wave is triggered by the point source, thus:

$$\frac{\partial \mathbf{x}_{NIP}}{\partial \varphi}(0,\varphi,\theta) = \frac{\partial \mathbf{x}_{NIP}}{\partial \theta}(0,\varphi,\theta) = 0, \tag{C.6}$$

$$Q_{ij}^{NIP}(0) = 0, \qquad i,j = 2,3. \tag{C.7}$$

$$\begin{aligned}
P_{22}^{NIP}(0) &= \left(\frac{\partial}{\partial\varphi}\frac{\mathbf{e}_n^{NIP}}{v\left(\mathbf{x}_{NIP}, \mathbf{e}_n^{NIP}\right)}, \mathbf{t}(\sigma_0)\right)(0,\varphi,\pi/2) = 0,\\
P_{23}^{NIP}(0) &= \left(\frac{\partial}{\partial\theta}\frac{\mathbf{e}_n^{NIP}}{v\left(\mathbf{x}_{NIP}, \mathbf{e}_n^{NIP}\right)}, \mathbf{t}(\sigma_0)\right)(0,\varphi,\pi/2) = -\frac{1}{v\left(\mathbf{x}_{NIP}, \mathbf{e}_n^{NIP}\right)}(0,\varphi,\pi/2),\\
P_{32}^{NIP}(0) &= \left(\frac{\partial}{\partial\varphi}\frac{\mathbf{e}_n^{NIP}}{v\left(\mathbf{x}_{NIP}, \mathbf{e}_n^{NIP}\right)}, \left[\mathbf{t}(\sigma_0), \mathbf{e}_n^{NIP}\right]\right)(0,\varphi,\pi/2) = \frac{1}{v\left(\mathbf{x}_{NIP}, \mathbf{e}_n^{NIP}\right)}(0,\varphi,\pi/2),\\
P_{33}^{NIP}(0) &= \left(\frac{\partial}{\partial\theta}\frac{\mathbf{e}_n^{NIP}}{v\left(\mathbf{x}_{NIP}, \mathbf{e}_n^{NIP}\right)}, \left[\mathbf{t}(\sigma_0), \mathbf{e}_n^{NIP}\right]\right)(0,\varphi,\pi/2) = 0,
\end{aligned} \tag{C.8}$$

where $v\left(\mathbf{x}, \mathbf{e}_n\right)$ stands for the phase velocity at a point $\mathbf{x}$ corresponding to the wavefront normal direction $\mathbf{e}_n$.

Initial conditions for the N-wave contain geometrical characteristics of the edge as a space curve:

$$\frac{\partial \mathbf{x}_N}{\partial \varphi}(0,\varphi,\sigma) = 0, \qquad \frac{\partial \mathbf{x}_N}{\partial \sigma}(0,\varphi,\sigma) = \mathbf{t}(\sigma), \tag{C.9}$$

$$Q_{i\,2}^{N}(0) = 0, \qquad Q_{i\,3}^{N}(0) = \delta_{i\,2}, \qquad i = 2,3; \tag{C.10}$$

$$\begin{aligned}
P_{22}^{N}(0) &= \left(\frac{\partial}{\partial\varphi}\frac{\mathbf{e}_n^{N}}{v\left(\mathbf{x}_{N}, \mathbf{e}_n^{N}\right)}, \mathbf{t}(\sigma)\right)(0,\varphi,\sigma_0) = 0,\\
P_{23}^{N}(0) &= \left(\frac{\partial}{\partial\sigma}\frac{\mathbf{e}_n^{N}}{v\left(\mathbf{x}_{N}, \mathbf{e}_n^{N}\right)}, \mathbf{t}(\sigma)\right)(0,\varphi,\sigma_0) = 0,\\
P_{32}^{N}(0) &= \left(\frac{\partial}{\partial\varphi}\frac{\mathbf{e}_n^{N}}{v\left(\mathbf{x}_{N}, \mathbf{e}_n^{N}\right)}, \left[\mathbf{t}(\sigma), \mathbf{e}_n^{N}\right]\right)(0,\varphi,\sigma_0) = \frac{1}{v\left(\mathbf{x}_{NIP}, \mathbf{e}_n^{NIP}\right)}(0,\varphi,\pi/2),\\
P_{33}^{N}(0) &= \left(\frac{\partial}{\partial\sigma}\frac{\mathbf{e}_n^{N}}{v\left(\mathbf{x}_{N}, \mathbf{e}_n^{N}\right)}, \left[\mathbf{t}(\sigma), \mathbf{e}_n^{N}\right]\right)(0,\varphi,\sigma_0) = \frac{\sin\varphi\cos\varphi K(\sigma_0) + T(\sigma_0)}{v\left(\mathbf{x}_{NIP}, \mathbf{e}_n^{NIP}\right)(0,\varphi,\pi/2)},
\end{aligned} \tag{C.11}$$

where the Frenet-Serret equations were used to introduce curvature K and torsion T of the edge.

These initial conditions are valid for all rays in the common ray family, for each shooting angle φ including the zero-offset ray. Note, initial geometrical spreading of both N- and NIP-waves is zero: $\det Q_{NIP}(0) = \det Q_N(0) = 0$. The ray tube collapses when propagated back for both the point source and the line source.

We will further use the matrices defining the wavefront curvature $M_{NIP} = P_{NIP}Q_{NIP}^{-1}$ and $M_N = P_N Q_N^{-1}$ expressed in terms of the 4×4 upward dynamic ray tracing propagator

$$\Pi(t,0) = \begin{pmatrix} Q_1(t,0) & Q_2(t,0) \\ P_1(t,0) & P_2(t,0) \end{pmatrix}. \tag{C.12}$$

$$Q_{NIP}(t) = Q_2 P_{NIP}(0), \quad P_{NIP}(t) = P_2 P_{NIP}(0), \quad M_{NIP} = P_2 Q_2^{-1}. \tag{C.13}$$

$$\begin{aligned} Q_N(t) &= Q_1 Q_N(0) + Q_2 P_N(0), \\ P_N(t) &= P_1 Q_N(0) + P_2 P_N(0). \end{aligned} \tag{C.14}$$

Using symplecticity of the propagator, one can find an identity

$$P_1 = P_2 Q_2^{-1} Q_1 - Q_2^{-1T}, \tag{C.15}$$

which helps to transform P_N:

$$P_N(t) = -Q_2^{-1T} Q_N(0) + P_2 Q_2^{-1} Q_N(t). \tag{C.16}$$

Therefore,

$$M_N(t) = -Q_2^{-1T} Q_N(0) Q_N^{-1}(t) + M_{NIP}(t) \tag{C.17}$$

and

$$\det\left(M_{NIP}(t) - M_N(t)\right) = \frac{1}{v^2\left(\mathbf{x}_{NIP}, \mathbf{e}_n^{NIP}\right)} (0, \varphi, \pi/2) \frac{\det Q_N(0)}{\det Q_{NIP}(t) \det Q_N(t)} = 0. \tag{C.18}$$

If both NIP-wave and N-wave have no caustic at the time t, the left side of this equation is defined and equals zero. It is an invariant for simultaneous point and line source wave propagation.

Now we provide the derivation for the second-derivatives matrices of traveltimes in Cartesian coordinates. Transformation to the wavefront-orthonormal coordinates of the 3×3 Cartesian matrix of second traveltime derivatives in general anisotropic medium gives a matrix

$$M^{(3\times3)} = H\hat{M}^{(3\times3)}H^T = \frac{1}{v} \cdot \begin{pmatrix} \left(\frac{d\mathbf{p}}{dt}, \mathbf{e}_1\right) - \left(\frac{d\mathbf{p}}{dt}, \frac{\mathbf{v}_r^\perp}{v}\right) + \left(\mathbf{v}_r^\perp, M\frac{\mathbf{v}_r^\perp}{v}\right) & \left(\left(\frac{d\mathbf{p}}{dt}\right)_\perp - M\mathbf{v}_r^\perp\right)^T \\ \left(\frac{d\mathbf{p}}{dt}\right)_\perp - M\mathbf{v}_r^\perp & vM \end{pmatrix}, \tag{C.19}$$

where H is an orthogonal matrix with rows being wavefront-orthonormal basis vectors, $\mathbf{v}_r$ is ray velocity, $\perp$ is used to denote a vector projected to the wavefront-tangent plane. Because

we consider curvatures of two waves along the same ray, the following relations hold:

$$M_{NIP}^{(3\times3)} - M_{N}^{(3\times3)} = H\left(\hat{M}_{NIP}^{(3\times3)} - \hat{M}_{N}^{(3\times3)}\right)H^{T} = \begin{pmatrix} \left(\frac{\mathbf{v}_r^{\perp}}{v}, (M_{NIP}-M_N)\frac{\mathbf{v}_r^{\perp}}{v}\right) & \left(-(M_{NIP}-M_N)\frac{\mathbf{v}_r^{\perp}}{v}\right)^{T} \\ -(M_{NIP}-M_N)\frac{\mathbf{v}_r^{\perp}}{v} & M_{NIP}-M_N \end{pmatrix}, \tag{C.20}$$

so that

$$\det\left(M_{NIP}^{(3\times3)} - M_{N}^{(3\times3)}\right) = \det\left(\hat{M}_{NIP}^{(3\times3)} - \hat{M}_{N}^{(3\times3)}\right) = 0. \tag{C.21}$$

Moreover, this holds for any two wavefronts on a coinciding ray.

Now we show that a more specific identity for 2×2 Cartesian matrices is present on a common ray for two wavefronts with vanishing geometrical spreading at one point (one of them must be a point source), as in the case of the NIP- and the N-front. We can represent the residual matrix as follows:

$$M_{NIP}^{(3\times3)} - M_{N}^{(3\times3)} = \begin{pmatrix} -\frac{(\mathbf{v}_r,\mathbf{e}_2)}{v} & -\frac{(\mathbf{v}_r,\mathbf{e}_3)}{v} \\ 1 & 0 \\ 0 & 1 \end{pmatrix} (M_{NIP}-M_N) \begin{pmatrix} -\frac{(\mathbf{v}_r,\mathbf{e}_2)}{v} & 1 & 0 \\ -\frac{(\mathbf{v}_r,\mathbf{e}_3)}{v} & 0 & 1 \end{pmatrix}. \tag{C.22}$$

For the 2×2 Cartesian matrices, we use an inverse transformation:

$$\hat{M}_{NIP}^{(x,y)} - \hat{M}_{N}^{(x,y)} = \begin{pmatrix} (\mathbf{e}_1)_x & (\mathbf{e}_2)_x & (\mathbf{e}_3)_x \\ (\mathbf{e}_1)_y & (\mathbf{e}_2)_y & (\mathbf{e}_3)_y \end{pmatrix} \left(M_{NIP}^{(3\times3)} - M_{N}^{(3\times3)}\right) \begin{pmatrix} (\mathbf{e}_1)_x & (\mathbf{e}_1)_y \\ (\mathbf{e}_2)_x & (\mathbf{e}_2)_y \\ (\mathbf{e}_3)_x & (\mathbf{e}_3)_y \end{pmatrix}. \tag{C.23}$$

Substituting the factorized representation (C.22), we obtain a 2×2 transformation

$$\hat{M}_{NIP}^{(x,y)} - \hat{M}_{N}^{(x,y)} = H^{(x,y)T}\left(M_{NIP}-M_N\right)H^{(x,y)} \tag{C.24}$$

with

$$H^{(x,y)} = \begin{pmatrix} -\frac{(\mathbf{v}_r,\mathbf{e}_2)}{v}(\mathbf{e}_1)_x + (\mathbf{e}_2)_x & -\frac{(\mathbf{v}_r,\mathbf{e}_2)}{v}(\mathbf{e}_1)_y + (\mathbf{e}_2)_y \\ -\frac{(\mathbf{v}_r,\mathbf{e}_3)}{v}(\mathbf{e}_1)_x + (\mathbf{e}_3)_x & -\frac{(\mathbf{v}_r,\mathbf{e}_3)}{v}(\mathbf{e}_1)_y + (\mathbf{e}_3)_y \end{pmatrix}. \tag{C.25}$$

Recalling (C.18) we finally obtain

$$\det\left(\hat{M}_{NIP}^{(x,y)} - \hat{M}_{N}^{(x,y)}\right) = 0. \tag{C.26}$$

Analogous invariant relations take place for other pairs of coordinates as well:

$$\det\left(\hat{M}_{NIP}^{(y,z)} - \hat{M}_{N}^{(y,z)}\right) = 0, \qquad \det\left(\hat{M}_{NIP}^{(x,z)} - \hat{M}_{N}^{(x,z)}\right) = 0. \tag{C.27}$$

The equations above represent the identification criterion for the edge diffraction, generally formulated in the paper as $\det(\hat{M}_{NIP} - \hat{M}_N) = 0$.

C.2 On regularity of a focusing curve

If NIP- and N-wave have no caustics at the acquisition point, the elements of the matrices $\hat{M}_{NIP}$ and $\hat{M}_N$ are finite. In this case, the focusing curve is regular due to existence of the unit length tangent with components $\dot{x}$ and $\dot{y}$. We first consider the family of rays common for the NIP- and the N-wave $\mathbf{x}(\tau, \varphi, \gamma_0)$. We also assume smoothness with respect to φ, otherwise $\dot{x}$, $\dot{y}$ don't exist at a cusp of the wavefront. γ_0 is the fixed value of the third ray-coordinate: for the N-wave – a length parameter of edge, for the NIP-wave – a complementary shooting angle of slowness out of the edge-orthogonal plane. An implicit equation for the traveltimes of each ray given as

$$z(\tau, \varphi, \gamma_0) = 0\,, \tag{C.28}$$

defines a function if $\frac{\partial z}{\partial \tau} = (\mathbf{v}_r)_z \neq 0$, where $\mathbf{v}_r$ is a vector of ray velocity. Using the ray tracing system (see e.g., Červený, 2001) implies existence of a function $\tau = \tau(\varphi)$ when the emerging ray is not tangent to the surface:

$$\frac{d\tau}{d\varphi} = -\frac{1}{(\mathbf{v}_r)_z}\frac{\partial z}{\partial \varphi}. \tag{C.29}$$

Therefore, we can construct the focusing curve parameterized with the ray-coordinate φ:

$$x = x(\tau(\varphi), \varphi, \gamma_0), \quad y = y(\tau(\varphi), \varphi, \gamma_0). \tag{C.30}$$

The focusing curve becomes irregular at a point when the derivatives

$$\begin{aligned} \frac{dx}{d\varphi} &= \frac{\partial x}{\partial \varphi} + \frac{\partial x}{\partial \tau}\frac{d\tau}{d\varphi} = \frac{\partial x}{\partial \varphi} - \frac{(\mathbf{v}_r)_x}{(\mathbf{v}_r)_z}\frac{\partial z}{\partial \varphi}, \\ \frac{dy}{d\varphi} &= \frac{\partial y}{\partial \varphi} + \frac{\partial y}{\partial \tau}\frac{d\tau}{d\varphi} = \frac{\partial y}{\partial \varphi} - \frac{(\mathbf{v}_r)_y}{(\mathbf{v}_r)_z}\frac{\partial z}{\partial \varphi} \end{aligned} \tag{C.31}$$

vanish. In this case, the ray Jacobian (transformation from the ray-coordinates to the Cartesian coordinates) equals zero:

$$J = \begin{vmatrix} \frac{\partial x}{\partial \tau} & \frac{\partial x}{\partial \varphi} & \frac{\partial x}{\partial \gamma} \\ \frac{\partial y}{\partial \tau} & \frac{\partial y}{\partial \varphi} & \frac{\partial y}{\partial \gamma} \\ \frac{\partial z}{\partial \tau} & \frac{\partial z}{\partial \varphi} & \frac{\partial z}{\partial \gamma} \end{vmatrix} = \frac{\partial z}{\partial \varphi}\frac{1}{(\mathbf{v}_r)_z}\begin{vmatrix} (\mathbf{v}_r)_x & (\mathbf{v}_r)_x & \frac{\partial x}{\partial \gamma} \\ (\mathbf{v}_r)_y & (\mathbf{v}_r)_y & \frac{\partial y}{\partial \gamma} \\ (\mathbf{v}_r)_z & (\mathbf{v}_r)_z & \frac{\partial z}{\partial \gamma} \end{vmatrix} = 0. \tag{C.32}$$

Therefore, if focusing curve is irregular there is a caustic of N- and also of NIP-wave. Vice versa, if both N- and NIP-waves have no caustics, the focusing curve is regular.

C.3 Geometrical spreading of reflected wave at zero offsets

In this appendix, we recapitulate derivation of equation (4.12) for the two-way zero-offset geometrical spreading (Equations 14 and 24 in Hubral (1983)). We first establish a relation between the second-derivatives of traveltime matrix of the reflected wave, which are

expressed by the curvature matrices of NIP- and N-waves. We follow the approach formulated in Krey (1983). Our derivations are however based on the CRS approximation for the sake of simplicity. The parabolic CRS approximation for reflected traveltimes reads as:

$$t = t_0 + 2(\mathbf{p}, \triangle\mathbf{x}_m) + \left(\mathbf{h}, \hat{M}_{NIP}\mathbf{h}\right) + \left(\triangle\mathbf{x}_m, \hat{M}_N \triangle\mathbf{x}_m\right). \tag{C.33}$$

Considering a special direction when $\triangle\mathbf{x}_m = \mathbf{h}$ allows for computing two-point traveltime between a central midpoint $\mathbf{x}_s = \mathbf{x}_0$ and a point $\mathbf{x}_r = \mathbf{x}_0 + 2\triangle\mathbf{x}_m$:

$$t(\mathbf{x}_0 + 2\triangle\mathbf{x}_m,\mathbf{x}_0) = \\ t_0 + 2(\mathbf{p}, \triangle\mathbf{x}_m) + \left(\triangle\mathbf{x}_m, \left(\hat{M}_{NIP} + \hat{M}_N\right)\triangle\mathbf{x}_m\right). \tag{C.34}$$

Expanding the two-point traveltime and cancelling out zero- and first-order terms provides a relation valid for an arbitrary direction of $\triangle\mathbf{x}_m$:

$$\left(\frac{\triangle\mathbf{x}_m}{||\triangle\mathbf{x}_m||}, \hat{M}\frac{\triangle\mathbf{x}_m}{||\triangle\mathbf{x}_m||}\right) = \left(\frac{\triangle\mathbf{x}_m}{||\triangle\mathbf{x}_m||}, \frac{1}{2}\left(\hat{M}_{NIP} + \hat{M}_N\right)\frac{\triangle\mathbf{x}_m}{||\triangle\mathbf{x}_m||}\right). \tag{C.35}$$

Since the direction is arbitrary and the matrices are symmetric, the following applies:

$$\hat{M} = \frac{1}{2}\left(\hat{M}_{NIP} + \hat{M}_N\right). \tag{C.36}$$

Analogously, one can obtain identities for every pair of Cartesian coordinates. The identity thus holds for the whole 3×3 second-derivatives of traveltime matrices, and, consequently, for the 2×2-matrix in the wavefront-orthonormal coordinates:

$$M = \frac{1}{2}\left(M_{NIP} + M_N\right). \tag{C.37}$$

Applying the derivation from Appendix A (formula C.17) but for the NIP-wave coupled with the reflected wave yields

$$M(t) = -Q_2^{-1T}Q(0)Q^{-1}(t) + M_{NIP}(t). \tag{C.38}$$

Comparing (C.37) with (C.38) followed by computing determinant provides

$$\det Q = \frac{4\det Q(0)}{\det Q_2 \det(M_{NIP} - M_N)}. \tag{C.39}$$

$\det Q(0)$ is a value of the geometrical spreading just after the reflection. Right before the reflection, geometrical spreading is equal to $\frac{1}{v^2}\det Q_2$ due to the reciprocity of the relative geometrical spreading $\det Q_2$ (e.g., Červený, 2001). The geometrical spreading undergoes a sign change when incident wavefront is tangent to the interface: $\det Q(0) = -\frac{1}{v^2}\det Q_2$. Finally, we obtain:

$$\det Q = -\frac{1}{v^2}\frac{4}{\det(M_{NIP} - M_N)}, \tag{C.40}$$

which corresponds to the equation 14 in Hubral (1983).

To explain the sign change, we consider an incident $\mathbf{x}^{(0)}(t, \gamma_2, \gamma_3)$ and reflected $\mathbf{x}^{(1)}(t, \gamma_2, \gamma_3)$ set of rays. Incident rays touch the reflected ones on the interface at the corresponding incidence time:

$$\mathbf{x}^{(0)}(t(\gamma_2, \gamma_3), \gamma_2, \gamma_3) = \mathbf{x}^{(1)}(t(\gamma_2, \gamma_3), \gamma_2, \gamma_3). \tag{C.41}$$

Differentiating the identity with respect to the ray-coordinates and accounting for the fact that normal-incidence ray has minimal time, leads us to conclusion that the whole vector remains continuous:

$$\frac{\partial \mathbf{x}^{(0)}}{\partial \gamma_i} = \frac{\partial \mathbf{x}^{(1)}}{\partial \gamma_i}, \qquad i = 2, 3. \tag{C.42}$$

However, if we aim at preserving the orientation of the basis after reversing of the wavefront normal, we should choose the basis vectors in a way they undergo a jump. For instance, we choose $\mathbf{e}_2^{(1)} = \mathbf{e}_3^{(0)}$ and $\mathbf{e}_3^{(1)} = \mathbf{e}_2^{(0)}$, which together with condition (C.42) and definition (C.5) results in

$$Q^{(0)} = \mathcal{P} Q^{(1)}, \quad \mathcal{P} = \begin{pmatrix} 0 & 1 \\ 1 & 0 \end{pmatrix}, \quad \det Q^{(1)} = -\det Q^{(0)}. \tag{C.43}$$

D Appendix for the Chapter 5

D.1 NIP-wave theorem for polarization vector

In this section, we provide formulas for the polarization derivatives with respect to the midpoint coordinate and the half-offset in isotropic media. We consider monotypic waves only and also do not acknowledge the free surface. The formulas are given in terms of the natural representations (see Section 5.4).

First, we look upon the P-wave polarization. Considering a zero-offset experiment provides a way to express the reflected-wave polarization in terms of the exploding-reflector traveltimes (N-wave):

$$\mathbf{g}_P(x_0, \triangle x_m, 0) = -v_P(x_0 + \triangle x_m, 0)\nabla t_N^P(x_0 + \triangle x_m, 0). \tag{D.1}$$

Thus, the derivative of the reflected-wave polarization with respect to the midpoint coordinate is equal to a space derivative of the N-wave polarization:

$$\partial_{\triangle x_m}\mathbf{g}_P(x_0, 0, 0) = -\left(v_P \begin{pmatrix}\partial_{xx}\\ \partial_{xz}\end{pmatrix} t_N^P + \partial_x v_P \mathbf{p}_P\right) = \partial_x \mathbf{g}_N^P. \tag{D.2}$$

We then consider a CMP experiment in order to get the polarization derivative with respect to the half-offset, i.e., we set the midpoint displacement to zero. Polarization vector in this case can be expressed in terms of the two-point reflected-wave traveltime:

$$\mathbf{g}_P(x_0, 0, h) = -v_P(\mathbf{x}_r)\nabla_{\mathbf{x}_r} t_P(\mathbf{x}_r; \mathbf{x}_s). \tag{D.3}$$

According to the definition (5.1), components of the source-position vector, $\mathbf{x}_s$, and receiver-position vector, $\mathbf{x}_r$, are related to the common-midpoint method coordinate, $x_m = x_0$, and

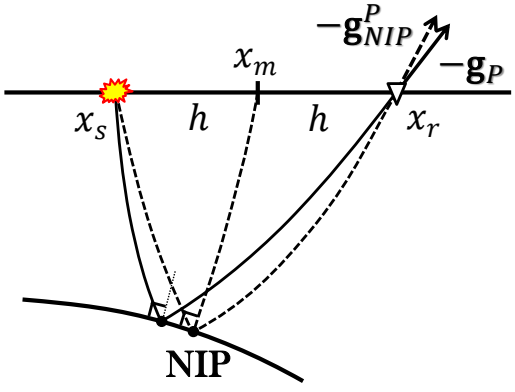

Figure D.1: NIP-wave theorem illustration. Reflected wave (solid rays) is approximated by the NIP-wave (dashed rays) in a sense of traveltime and polarization.

the half-offset, h, as $x_s = x_0 - h$, $x_r = x_0 + h$, $z_s = z_r = 0$. Differentiating eq. (D.3) with respect to the half-offset leads to an expression containing the second-order derivatives of the two-point traveltime:

$$\begin{aligned}\partial_h \mathbf{g}_P(x_0, 0, 0) &= -\partial_h \left(\begin{array}{c} v_P(x_0 + h, 0)\partial_{x_r} t_P(x_0 + h, 0; x_0 - h, 0) \\ v_P(x_0 + h, 0)\partial_{z_r} t_P(x_0 + h, 0; x_0 - h, 0) \end{array} \right)\Bigg|_{h=0} \\ &= \left(\begin{array}{c} v_P(\mathbf{x}_0)\left(\partial_{x_s x_r} - \partial_{x_r x_r}\right) - \partial_x v_P(\mathbf{x}_0)\partial_{x_r} \\ v_P(\mathbf{x}_0)\left(\partial_{x_s z_r} - \partial_{x_r z_r}\right) - \partial_x v_P(\mathbf{x}_0)\partial_{z_r} \end{array} \right) t_P(\mathbf{x}_0; \mathbf{x}_0). \end{aligned} \tag{D.4}$$

The first-order derivatives constitute the slowness vector of the zero-offset ray:

$$\partial_{x_r} t_P(\mathbf{x}_0; \mathbf{x}_0) = p_x^P, \quad \partial_{z_r} t_P(\mathbf{x}_0; \mathbf{x}_0) = p_z^P. \tag{D.5}$$

We have to investigate the value of two-point traveltime Hessian,

$$H_P(\mathbf{x}_r; \mathbf{x}_s) = \left(\begin{array}{cccc} \partial_{x_r x_r} & \partial_{x_r z_r} & \partial_{x_r x_s} & \partial_{x_r z_s} \\ \partial_{z_r x_r} & \partial_{z_r z_r} & \partial_{z_r x_s} & \partial_{z_r z_s} \\ \partial_{x_s x_r} & \partial_{x_s z_r} & \partial_{x_s x_s} & \partial_{x_s z_s} \\ \partial_{z_s x_r} & \partial_{z_s z_r} & \partial_{z_s x_s} & \partial_{z_s z_s} \end{array} \right) t_P(\mathbf{x}_r; \mathbf{x}_s), \tag{D.6}$$

when source and receiver positions coincide, i.e., $\mathbf{x}_r = \mathbf{x}_s = \mathbf{x}_0$. For this, we follow the approach given in the NIP-wave theorem proof by Chernjak and Gritsenko (1979). We omit the wave type subscript in this derivations since they are common for both monotypic waves. The two-point traveltime can be represented as a sum of one-way times:

$$t(\mathbf{x}_r; \mathbf{x}_s) = T(\mathbf{x}_s; x_{refl}(\mathbf{x}_r; \mathbf{x}_s)) + T(\mathbf{x}_r; x_{refl}(\mathbf{x}_r; \mathbf{x}_s)) = F(\mathbf{x}_r; \mathbf{x}_s; x_{refl}(\mathbf{x}_r; \mathbf{x}_s)), \tag{D.7}$$

where $x_{refl}(\mathbf{x}_r; \mathbf{x}_s)$ denotes a horizontal coordinate of the reflection point. This coordinate becomes a function of source and receiver positions for a given reflector.

$$\begin{aligned} \nabla_{\mathbf{x}_r} t &= \nabla_{\mathbf{x}_r} F + \partial_{x_{refl}} F \ \nabla_{\mathbf{x}_r} x_{refl}, \\ \nabla_{\mathbf{x}_s} t &= \nabla_{\mathbf{x}_s} F + \partial_{x_{refl}} F \ \nabla_{\mathbf{x}_s} x_{refl}. \end{aligned} \tag{D.8}$$

Due to the Fermat principle

$$\partial_{x_{refl}} F(\mathbf{x}_r; \mathbf{x}_s; x_{refl}(\mathbf{x}_r; \mathbf{x}_s)) = 0 \tag{D.9}$$

and, therefore,

$$\begin{aligned} \nabla_{\mathbf{x}_r} t(\mathbf{x}_r; \mathbf{x}_s) &= \nabla_{\mathbf{x}} T(\mathbf{x}_r; x_{refl}(\mathbf{x}_r; \mathbf{x}_s)), \\ \nabla_{\mathbf{x}_s} t(\mathbf{x}_r; \mathbf{x}_s) &= \nabla_{\mathbf{x}} T(\mathbf{x}_s; x_{refl}(\mathbf{x}_r; \mathbf{x}_s)). \end{aligned} \tag{D.10}$$

Differentiating these identities once again yields a representation for the two-point travel-

time Hessian:

$$H(\mathbf{x}_r;\mathbf{x}_s) = \begin{pmatrix} \begin{pmatrix}\partial_{xx}\,\partial_{xz}\\ \partial_{zx}\,\partial_{zz}\end{pmatrix} T(\mathbf{x}_r; x_{refl}(\mathbf{x}_r;\mathbf{x}_s)) & \mathbf{0} \\ \mathbf{0} & \begin{pmatrix}\partial_{xx}\,\partial_{xz}\\ \partial_{zx}\,\partial_{zz}\end{pmatrix} T(\mathbf{x}_s; x_{refl}(\mathbf{x}_r;\mathbf{x}_s)) \end{pmatrix} + \begin{pmatrix}\partial_{x_r}\ \partial_{z_r}\ \partial_{x_s}\ \partial_{z_s}\end{pmatrix}^T x_{refl}(\mathbf{x}_r;\mathbf{x}_s) \cdot \Big(\partial_{xx_{refl}} T(\mathbf{x}_r; x_{refl}(\mathbf{x}_r;\mathbf{x}_s))\ \partial_{zx_{refl}} T(\mathbf{x}_r; x_{refl}(\mathbf{x}_r;\mathbf{x}_s)) \\ \partial_{xx_{refl}} T(\mathbf{x}_s; x_{refl}(\mathbf{x}_r;\mathbf{x}_s))\ \partial_{zx_{refl}} T(\mathbf{x}_s; x_{refl}(\mathbf{x}_r;\mathbf{x}_s)) \Big). \tag{D.11}$$

Now, we can return to the polarization derivative calculation (D.4). By means of the two-point Hessian representation (D.11) we evaluate the following differences:

$$\begin{aligned}(\partial_{x_r x_r} - \partial_{x_s x_r}) t_P(\mathbf{x}_r;\mathbf{x}_s) &= \partial_{xx} T_P(\mathbf{x}_r; x^P_{refl}(\mathbf{x}_r;\mathbf{x}_s)) \\ &+ (\partial_{x_r} - \partial_{x_s}) x^P_{refl}(\mathbf{x}_r;\mathbf{x}_s) \partial_{xx_{refl}} T_P(\mathbf{x}_r; x^P_{refl}(\mathbf{x}_r;\mathbf{x}_s)),\end{aligned}$$

$$\begin{aligned}(\partial_{x_r z_r} - \partial_{x_s z_r}) t_P(\mathbf{x}_r;\mathbf{x}_s) &= \partial_{xz} T_P(\mathbf{x}_r; x^P_{refl}(\mathbf{x}_r;\mathbf{x}_s)) \\ &+ (\partial_{x_r} - \partial_{x_s}) x^P_{refl}(\mathbf{x}_r;\mathbf{x}_s) \partial_{zx_{refl}} T_P(\mathbf{x}_r; x^P_{refl}(\mathbf{x}_r;\mathbf{x}_s)).\end{aligned} \tag{D.12}$$

Position of the reflection point is reciprocal for any monotypic wave:

$$x^P_{refl}(\mathbf{x}_r;\mathbf{x}_s) = x^P_{refl}(\mathbf{x}_s;\mathbf{x}_r). \tag{D.13}$$

This reciprocity results in an identity

$$(\partial_{x_r} - \partial_{x_s}) x^P_{refl}(\mathbf{x}_0;\mathbf{x}_0) = 0. \tag{D.14}$$

Furthermore, setting $\mathbf{x}_r$ equal to $\mathbf{x}_s$ in eqs (D.12) yields relations to the NIP-wave:

$$\begin{aligned}(\partial_{x_r x_r} - \partial_{x_s x_r}) t_P(\mathbf{x}_0;\mathbf{x}_0) &= \partial_{xx} t^P_{NIP}, \\ (\partial_{x_r z_r} - \partial_{x_s z_r}) t_P(\mathbf{x}_0;\mathbf{x}_0) &= \partial_{xz} t^P_{NIP}.\end{aligned} \tag{D.15}$$

Finally,

$$\partial_h \mathbf{g}_P(x_0,0,0) = -\left(v_P \begin{pmatrix}\partial_{xx}\\ \partial_{xz}\end{pmatrix} t^P_{NIP} + \partial_x v_P \mathbf{p}_P \right) = \partial_x \mathbf{g}^P_{NIP}. \tag{D.16}$$

We call this identity the NIP-wave theorem for polarization vector. It states that at the zero offset, the derivative of the reflected-wave polarization with respect to the half-offset is equal to the spacial derivative of the fictitious NIP-wave polarization.

NIP-wave theorem for traveltimes (Chernjak and Gritsenko, 1979; Hubral and Krey, 1980) states that reflected-wave traveltimes can be approximated up to the second order with a sum of traveltimes of two NIP-wave branches if offsets are small. Both of the statements are illustrated in Fig. D.1. In terms of the second-order derivatives the theorem for traveltimes means the following identity:

$$\partial_{hh} t(x_0,0,0) = 2\partial_{xx} t_{NIP}.$$

It remains valid in heterogeneous anisotropic media until the traveltime is smooth and there is no focusing at the acquisition line (Fomel and Grechka, 2001). However, the term NIP-wave itself is confusing since for general anisotropy a zero-offset ray is not necessarily orthogonal to the reflector. Its extension to higher order derivatives is given by Fomel (1994). Similarly, the NIP-wave theorem for polarizations can be formulated as an approximation for small offsets. Polarization of reflected wave is approximated with polarization of the NIP-wave up to the first order.

The derivation for S-waves is similar to the derivation for P-waves. The only difference is the S-wave polarization given by a 90° clockwise rotation of the slowness vector:

$$\begin{aligned}
\partial_{\triangle x_m}\mathbf{g}_S(x_0,0,0) &= R^+\left(v_S\begin{pmatrix}\partial_{xx}\\ \partial_{xz}\end{pmatrix}t_N^S + \partial_x v_S \mathbf{p}_S\right) = \partial_x \mathbf{g}_N^S,\\
\partial_h \mathbf{g}_S(x_0,0,0) &= R^+\left(v_S\begin{pmatrix}\partial_{xx}\\ \partial_{xz}\end{pmatrix}t_{NIP}^S + \partial_x v_S \mathbf{p}_S\right) = \partial_x \mathbf{g}_{NIP}^S.
\end{aligned} \tag{D.17}$$

Bibliography

Al-Yahya, K. (1989). Velocity analysis by iterative profile migration. *Geophysics*, 54(6):718–729.

Alonaizi, F., Pevzner, R., Bóna, A., Shulakova, V., and Gurevich, B. (2013). 3D diffraction imaging of linear features and its application to seismic monitoring. *Geophysical Prospecting*, 61(6):1206–1217.

Aminzadeh, F., Burkhard, N., Kunz, T., Nicoletis, L., and Rocca, F. (1994). 3-D Modeling Project: 2nd Update. *The Leading Edge*, 13(9).

Aminzadeh, F., Burkhard, N., Long, J., Kunz, T., and Duclos, P. (1996). Three dimensional SEG/EAGE models - An Update. *The Leading Edge*, 15(2).

Amundsen, L. and Reitan, A. (1995). Decomposition of multicomponent sea-floor data into upgoing and downgoing P- and S-waves. *Geophysics*, 60(2):563–572.

Asgedom, E. G., Gelius, L. J., and Tygel, M. (2013). 2D common-offset traveltime based diffraction enhancement and imaging. *Geophysical Prospecting*, 61(6):1178–1193.

Babich, V. and Buldyrev, V. S. (1972). Asymptotic methods in short wave diffraction problems.

Babich, V. and Kiselev, A. (2018). *Elastic Waves: High Frequency Theory*. Chapman and Hall/CRC.

Babich, V. M. (1961). Ray method of the computation of the intensity of wave fronts in elastic inhomogeneous anisotropic medium. *Problems of the Dynamic Theory of Propagation of Seismic Waves*, 5:36–46 (in Russian).

Babich, V. M. (1994). Ray method of calculating the intensity of wavefronts in the case of a heterogeneous, anisotropic, elastic medium. *Geophys. J. Int.*, 118(2):379–383.

Bakker, P. (1990). Theory of edge diffraction in terms of dynamic ray tracing. *Geophysical Journal International*, 102(1):177–189.

Bakker, P. (1996). Theory of anisotropic dynamic ray tracing in ray-centred coordinates. *Pure appl. Geophys.*, 148(3-4):583–589.

Bauer, A., Schwarz, B., and Gajewski, D. (2016). Enhancement of prestack diffraction data and attributes using a traveltime decomposition approach. *Studia Geophysica et Geodaetica*, 60(3):471–486.

Bauer, A., Schwarz, B., and Gajewski, D. (2017). Utilizing diffractions in wavefront tomography. *Geophysics*, 82(2):R65–R73.

Bauer, A., Schwarz, B., Werner, T., and Gajewski, D. (2019). Unsupervised event indentification and tagging for diffraction focusing. *Geophysical Journal International*, 217(3):2165–2176.

Baykulov, M. and Gajewski, D. (2009). Prestack seismic data enhancement with partial common-reflection-surface (CRS) stack. *Geophysics*, 74(3):V49–V58.

Bergler, S., Duveneck, E., Höcht, G., Zhang, Y., and Hubral, P. (2002). Common-Reflection-Surface stack for converted waves. *Studia Geophysica et Geodaetica*, 46(2):165–175.

Berkovitch, A., Belfer, I., Hassin, Y., and Landa, E. (2009). Diffraction imaging by multifocusing. *Geophysics*, 74(6):WCA75–WCA81.

Billette, F. and Lambaré, G. (1998). Velocity macro-model estimation by stereotomography. *Geophysical Journal International*, 135(2):671–690.

Bishop, T., Bube, K., Cutler, R., Langan, R., Love, P., Resnick, J., Shuey, R., Spindler, D., and Wyld, H. (1985). Tomographic determination of velocity and depth in laterally varying media. *Geophysics*, 50(6):903–923.

Bloot, R., Coimbra, T. A., Faccipieri, J. H., and Tygel, M. (2018). Common-reflection-surface method in weakly anisotropic vertical transverse isotropic media. *Geophysics*, 83(3):C99–C113.

Brossier, R., Operto, S., and Virieux, J. (2009). Seismic imaging of complex onshore structures by 2D elastic frequency-domain full-waveform inversion. *Geophysics*, 74(6):WCC105–WCC118.

Byrd, R., Lu, P., and Nocedal, J. (1995). A limited memory algorithm for bound constrained optimization. *SIAM Journal on Scientific Computing*, 16(5):1190–1208.

Cartwright, J. and Jackson, M. (2008). Initiation of gravitational collapse of an evaporite basin margin: The Messinian saline giant, Levant Basin, eastern Mediterranean. *Geological Society of America Bulletin*, 120(3-4):399–413.

Červený, V. (1972). Seismic rays and ray intensities in inhomogeneous anisotropic media. *Geophys. J. R. astr. Soc.*, 29(1):1–13.

Červený, V. (2001). *Seismic Ray Theory*. Cambridge University Press.

Červený, V. (2007). A note on dynamic ray tracing in ray-centered coordinates in anisotropic inhomogeneous media. *Stud. Geophys. Geod.*, 51(3):411–422.

Cervenỳ, V. and Jan Moser, T. (2007). Ray propagator matrices in three-dimensional anisotropic inhomogeneous layered media. *Geophysical Journal International*, 168:593–604.

Chang, W. F. and McMechan, G. A. (1994). 3-D elastic prestack, reverse-time depth migration. *Geophysics*, 59(4):597–609.

Chauris, H., Noble, M. S., Lambare, G., and Podvin, P. (2002). Migration velocity analysis from locally coherent events in 2-D laterally heterogeneous media, Part I: Theoretical aspects. *Geophysics*, 67(4):1202–1212.

Chavent, G. (2010). *Nonlinear least squares for inverse problems: theoretical foundations and step-by-step guide for applications*. Springer Science & Business Media.

Chernjak, V. and Gritsenko, S. (1979). Interpretation of effective common-depth-point parameters for a spatial system of homogeneous beds with curved boundaries. *Soviet Geology and Geophysics*, 20(12):91–98.

Costa, J., Silva, F., Gomes, E., Schleicher, J., Melo, L., and Amazonas, D. (2008). Regularization in slope tomography. *Geophysics*, 73(5):VE39–VE47.

Crampin, S. (1985). Evaluation of anisotropy by shear-wave splitting. *Geophysics*, 50(1):142–152.

Dankbaar, J. W. M. (1985). Separation of P- and S-waves. *Geophysical Prospecting*, 33(7):970–986.

de Franco, R. and Musacchio, G. (2001). Polarization filter with singular value decomposition. *Geophysics*, 66(3):932–938.

Dell, S., Abakumov, I., Znak, P., Gajewski, D., Kashtan, B., and Ponomarenko, A. (2019). On the rule of diffractions in velocity model building: a full-waveform inversion example. *Studia Geophysica et Geodaetica*, 63:1–16.

Dell, S. and Gajewski, D. (2011). Common-reflection-surface-based workflow for diffraction imaging. *Geophysics*, 76(5):S187–S195.

Dell, S., Gajewski, D., and Tygel, M. (2014). Image-ray Tomography. *Geophys. Prospect.*, 62(3):413–426.

Dell, S., Gajewski, D., and Vanelle, C. (2012). Prestack time migration by common-migrated-reflector-element stacking. *Geophysics*, 77:S73–S82.

Dell, S., Hoelker, A., and Gajewski, D. (2018). Using seismic diffractions for assessment of tectonic overprint and fault interpretation. *Geophysics*, 84(1):IM1–IM9.

Dewangan, P. and Grechka, V. (2003). Inversion of multicomponent, multiazimuth, walkaway VSP data for the stiffness tensor. *Geophysics*, 68(3):1022–1031.

Diekmann, L., Schwarz, B., Bauer, A., and Gajewski, D. (2019). Source localisation and joint velocity model building using wavefront attributes. *Geophysical Journal International*, 219(2):995–1007.

Dümmong, S., Meier, K., Gajewski, D., and Hübscher, C. (2008). Comparison of prestack stereotomography and NIP wave tomography for velocity model building: Instances from the Messinian evaporites. *Geophysics*, 73(5):VE291–VE302.

Duveneck, E. (2004). Velocity model estimation with data-derived wavefront attributes. *Geophysics*, 69(1):265–274.

Farra, V. (1989). Ray perturbation theory for heterogeneous hexagonal anisotropic media. *Geophys. J. Int.*, 99(3):723–737.

Farra, V. and Madariaga, R. (1987). Seismic waveform modeling in heterogeneous media by ray perturbation theory. *Journal of Geophysical Research*, 92(B3):2697–2712.

Felsen, L. B. (1970). Rays, dispersion surfaces and their uses for radiation and diffraction problems. *SIAM Review*, 12(3):424–448.

Feng, Z. and Schuster, G. T. (2017). Elastic least-squares reverse time migration. *Geophysics*, 82(2):S143–S157.

Fomel, S. (1994). Recurrent formulas for derivatives of a CDP travel-time curve. *Russian Geology and Geophysics*, 35(2):118–126.

Fomel, S. (2009). Velocity analysis using AB semblance. *Geophysical Prospecting*, 57(3):311–321.

Fomel, S. and Grechka, V. (2001). Nonhyperbolic reflection moveout of P-waves: An overview and comparison of reasons. *CWP-372: Colorado School of Mines*.

Fomel, S. and Kazinnik, R. (2013). Non-hyperbolic common reflection surface. *Geophysical Prospecting*, 61(1):21–27.

Foster, D. J. and Gaiser, J. E. (1986). Elastic wave field decomposition of offset VSP data. In *SEG Technical Program Expanded Abstracts 1986*, pages 563–565.

Gajewski, D. and Pšenčik, I. (1990). Vertical seismic profile synthetics by dynamic ray tracing in laterally varying layered anisotropic structures. *J. geophys. Res.*, 95(B7):11301–11315.

Gajewski, D. and Tessmer, E. (2005). Reverse modelling for seismic event characterization. *Geophysical Journal International*, 163(1):276–284.

Gal'perin, E. I. (1984). *The polarization method of seismic exploration*. D. Reidel publishing company.

Gilbert, F. and Backus, G. E. (1966). Propagator matrices in elastic wave and vibration problems. *Geophysics*, 31(2):326–332.

Granli, J. R., Arntsen, B., Sollid, A., and Hilde, E. (1999). Imaging through gas-filled sediments using marine shear-wave data. *Geophysics*, 64(3):668–677.

Greenhalgh, S., Mason, I., Lucas, E., Pant, D., and Eames, R. (1990). Controlled direction reception filtering of P- and S-waves in τ-p space. *Geophysical Journal International*, 100(2):221–234.

Hansen, P. (1998). *Rank-deficient and discrete ill-posed problems: numerical aspects of linear inversion*. Society for Industrial and Applied Mathematics.

Hanyga, A. (1982). Dynamic ray tracing in an anisotropic medium. *Tectonophysics*, 90(1-2):243–251.

Hoecht, G., Ricarte, P., Bergler, S., and Landa, E. (2009). Operator-oriented CRS interpolation. *Geophysical Prospecting*, 57(6):957–979.

Hokstad, K. (2000). Multicomponent Kirchhoff migration. *Geophysics*, 65(3):861–873.

Hubral, P. (1983). Computing true amplitude reflections in a laterally inhomogeneous earth. *Geophysics*, 48(8):1051–1062.

Hubral, P. and Krey, T. (1980). *Interval velocities from seismic reflection time measurements*. Society of Exploration Geophysicists.

Ikeda, T., Matsuoka, T., Tsuji, T., and Nakayama, T. (2014). Characteristics of the horizontal component of Rayleigh waves in multimode analysis of surface waves. *Geophysics*, 80(1):EN1–EN11.

Jäger, R., Mann, J., Höcht, G., and Hubral, P. (2001). Common-reflection-surface stack: Image and attributes. *Geophysics*, 66(1):97–109.

Jech, J. and Pšenčík, I. (1989). First-order perturbation method for anisotropic media. *Geophys. J. Int.*, 99(2):369–376.

Jurkevics, A. (1988). Polarization analysis of three-component array data. *Bulletin of the Seismological Society of America*, 78(5):1725–1743.

Kashtan, B. M. and Petrashen, G. I. (1983). On calculation of geometrical spreading in inhomogeneous anisotropic elastic media. *Problems of the Dynamic Theory of Propagation of Seismic Waves*, 23:31–37 (in Russian).

Keller, J. B. (1962). Geometrical theory of diffraction. *Journal of the Optical Society of America*, 52(2):116–130.

Keydar, S. and Landa, E. (2019). Wave refocusing for linear diffractor using the time-reversal principle. *Geophysical Prospecting*, 67(5):1345–1353.

Klem-Musatov, K., Aizenberg, A. M., Pajchel, J., and Helle, H. B. (2008). *Edge and tip diffractions: Theory and applications in seismic prospecting*. Society of Exploration Geophysicists.

Klimeš, L. (2006). Ray-centred coordinate systems in anisotropic media. *Stud. Geophys. Geod.*, 50(3):431–447.

Klokov, A. and Fomel, S. (2012). Separation and imaging of seismic diffractions using migrated dip-angle gathers. *Geophysics*, 77(6):S131–S143.

Kosloff, D., Filho, A. Q., Tessmer, E., and Behle, A. (1989). Numerical solution of the acoustic and elastic wave equations by a new rapid expansion method. *Geophysical Prospecting*, 37(4):383–394.

Kosloff, D. D. and Baysal, E. (1982). Forward modeling by a Fourier method. *Geophysics*, 47(10):1402–1412.

Krey, T. (1983). A short and straightforward derivation of two equations from Hubral's paper "Computing true amplitude reflections in a laterally inhomogeneous earth". *Geophysics*, 48(8):1129–1131.

Kuo, J. T. and Dai, T. (1984). Kirchhoff elastic wave migration for the case of noncoincident source and receiver. *Geophysics*, 49(8):1223–1238.

Lambaré, G. (2008). Stereotomography. *Geophysics*, 73(5):VE25–VE34.

Landa, E., Keydar, S., and Jan Moser, T. (2010). Multifocusing revisited - inhomogeneous media and curved interfaces. *Geophysical Prospecting*, 58(6):925–938.

Lellouch, A. and Landa, E. (2018). Seismic velocity estimation using time-reversal focusing. *Geophysics*, 83(4):U43–U50.

Leung, S. and Qian, J. (2006). An adjoint state method for three-dimensional transmission traveltime tomography using first-arrivals. *Communications in Mathematical Sciences*, 4(1):249–266.

Mann, J. (2002). *Extensions and applications of the common reflection surface stack method*. Logos-Verlag.

Mann, J., Jäger, R., Müller, T., Höcht, G., and Hubral, P. (1999). Common-reflection-surface stack – a real data example. *Journal of Applied Geophysics*, 42(3-4):283–300.

Martin, M. A. and Davis, T. L. (1987). Shear-wave birefringence: A new tool for evaluating fractured reservoirs. *The Leading Edge*, 6(10):22–28.

Mayne, W. (1962). Common reflection point horizontal data stacking techniques. *Geophysics*, 27(6):927–938.

Mensch, T. and Farra, V. (1999). Computation of qP-wave rays, traveltimes and slowness vectors in orthorhombic media. *Geophys. J. Int.*, 138(1):244–256.

Morozov, I. B. and Smithson, S. B. (1996). Instantaneous polarization attributes and directional filtering. *Geophysics*, 61(3):872–881.

Moser, T. and Howard, C. (2008). Diffraction imaging in depth. *Geophysical Prospecting*, 56(5):627–641.

Neidell, N. S. and Taner, M. T. (1971). Semblance and other coherency measures for multichannel data. *Geophysics*, 36(3):482–497.

Netzeband, G., Hübscher, C., and Gajewski, D. (2006). The structural evolution of the Messinian evaporites in the Levantine Basin. *Marine Geology*, 230(3-4):249–273.

Nguyen, S., Baina, R., Alerini, M., Lambaré, G., Devaux, V., and Noble, M. (2008). Stereotomography assisted by migration of attributes. *Geophysical Prospecting*, 56(5):613–625.

Nowack, R. L. and Pšenčík, I. (1991). Perturbation from isotropic to anisotropic heterogeneous media in the ray approximation. *Geophysical Journal International*, 106(1):1–10.

Perelberg, A. I. and Hornbostel, S. C. (1994). Applications of seismic polarization analysis. *Geophysics*, 59(1):119–130.

Petrashen, G. and Kashtan, B. (1984). Theory of body-wave propagation in inhomogeneous anisotropic media. *Geophysical Journal International*, 76(1):29–39.

Pinnegar, C. R. (2006). Polarization analysis and polarization filtering of three-component signals with the time-frequency S transform. *Geophysical Journal International*, 165(2):596–606.

Plessix, R. (2006). A review of the adjoint-state method for computing the gradient of a functional with geophysical applications. *Geophysical Journal International*, 167(2):495–503.

Popov, M. M. and Pšenčík, I. (1978). Computation of ray amplitudes in inhomogeneous media with curved interfaces. *Stud. Geophys. Geod.*, 22(3):248–258.

Prieux, V., Brossier, R., Operto, S., and Virieux, J. (2013). Multiparameter full waveform inversion of multicomponent ocean-bottom-cable data from the Valhall field. Part 1: imaging compressional wave speed, density and attenuation. *Geophysical Journal International*, 194(3):1640–1664.

Pšenčík, I. and Farra, V. (2005). First-order ray tracing for qp waves in inhomogeneous, weakly anisotropic media. *Geophysics*, 70(6):D65–D75.

Rad, P. B., Schwarz, B., Gajewski, D., and Vanelle, C. (2018). Common-reflection-surface-based prestack diffraction separation and imaging. *Geophysics*, 83(1):S47–S55.

Rene, R., Fitter, J., Forsyth, P., Kim, K., Murray, D., Walters, J., and Westerman, J. (1986). Multicomponent seismic studies using complex trace analysis. *Geophysics*, 51(6):1235–1251.

Rosenbaum, S. (1967a). Edge diffraction in an arbitrary anisotropic medium. I. *Canadian Journal of Physics*, 45(11):3479–3502.

Rosenbaum, S. (1967b). Edge diffraction in an arbitrary anisotropic medium. II. *Canadian Journal of Physics*, 45(11):3503–3519.

S. Dell, D. G. and Hoelker, A. (2019). Azimuthal Diffraction Imaging: a Land Data Example from Northern Switzerland. *81st EAGE Conference and Exhibition*, expanded abstract.

Sambolian, S., Operto, S., Ribodetti, A., Tavakoli F., B., and Virieux, J. (2019). Parsimonious slope tomography based on eikonal solvers and the adjoint-state method. *Geophysical Journal International*, 218(1):456–478.

Schalkwijk, K., Wapenaar, C., and Verschuur, D. (2003). Adaptive decomposition of multicomponent ocean-bottom seismic data into downgoing and upgoing P- and S-waves. *Geophysics*, 68(3):1091–1102.

Schwarz, B. (2019). Coherent wavefield subtraction for diffraction separation. *Geophysics*, 84(3):V157–V168.

Schwarz, B., Bauer, A., and Gajewski, D. (2016). Passive seismic source localization via common-reflection-surface attributes. *Studia Geophysica et Geodaetica*, 60(3):531–546.

Schwarz, B., Vanelle, C., Gajewski, D., and Kashtan, B. (2014). Curvatures and inhomogeneities: An improved common-reflection-surface approach. *Geophysics*, 79(5):S231–S240.

Sears, T. J., Singh, S. C., and Barton, P. J. (2008). Elastic full waveform inversion of multi-component OBC seismic data. *Geophysical Prospecting*, 56(6):843–862.

Shieh, C. F. and Herrmann, R. B. (1990). Ground roll: Rejection using polarization filters. *Geophysics*, 55(9):1216–1222.

Soukina, S., Gajewski, D., and Kashtan, B. (2003). Traveltime computation for 3D anisotropic media by a finite-difference perturbation method. *Geophys. Prospect.*, 51(5):431–441.

Stork, C. (1992). Reflection tomography in the postmigrated domain. *Geophysics*, 57(5):680–692.

Sword, C. H. (1986). Tomographic determination of interval velocities from picked reflection seismic data. In *SEG Technical Program Expanded Abstracts 1986*, pages 657–660. Society of Exploration Geophysicists.

Tarantola, A. (1987). *Inverse Problem Theory*. Elsevier Science.

Tatham, R. H., McCormack, M. D., and Neitzel, E. (1991). *Multicomponent seismology in petroleum exploration*. Society of Exploration Geophysicists.

Tavakoli, F. B., Operto, S., Ribodetti, A., and Virieux, J. (2017). Slope tomography based on eikonal solvers and the adjoint-state method. *Geophysical Journal International*, 209(3):1629–1647.

Thomsen, L. (1986). Weak elastic anisotropy. *Geophysics*, 51(10):1954–1966.

Tsvankin, I. and Grechka, V. (2011). *Seismology of azimuthally anisotropic media and seismic fracture characterization*. Society of Exploration Geophysicists.

Vanelle, C., Abakumov, I., and Gajewski, D. (2018). Wavefront attributes in anisotropic media. *Geophysical Journal International*, 214(1):430–443.

Virieux, J. and Operto, S. (2009). An overview of full-waveform inversion in exploration geophysics. *Geophysics*, 74(6):WCC1–WCC26.

Waheed, U. B., Yarman, C. E., and Flagg, G. (2015). An iterative, fast-sweeping-based eikonal solver for 3D tilted anisotropic media. *Geophysics*, 80(3):C49–C58.

Walda, J. and Gajewski, D. (2017). Determination of wavefront attributes by differential evolution in the presence of conflicting dips. *Geophysics*, 82(4):V229–V239.

Walda, J., Schwarz, B., and Gajewski, D. (2017). A competitive comparison of multiparameter stacking operators. *Geophysics*, 82(4):V275–V283.

Wang, Y., Singh, S. C., and Barton, P. J. (2002). Separation of P- and SV-wavefields from multi-component seismic data in the τ-p domain. *Geophysical Journal International*, 151(2):663–672.

Xie, Y. and Gajewski, D. (2017). 5-D interpolation with wave-front attributes. *Geophysical Journal International*, 211(2):897–919.

Xie, Y. and Gajewski, D. (2019). Reliability of data-driven wavefront attributes in laterally heterogeneous media. *Geophysics*, 84(3):O49–O62.

Yang, J., Zhu, H., Huang, J., and Li, Z. (2018). 2D isotropic elastic Gaussian-beam migration for common-shot multicomponent records. *Geophysics*, 83(2):S127–S140.

Yang, P., Dell, S., Gajewski, D., and Znak, P. (2019). Improving focusing and estimation of excitation time for passive seismic events: sparse and limited-aperture data examples. In *SEG Technical Program Expanded Abstracts 2019*, pages 3096–3100. Society of Exploration Geophysicists.

Yin, J. and Nakata, N. (2019). Diffraction imaging using geometric-mean reverse time migration and common-reflection surface. *Geophysics*, 84(4):S355–S364.

Zhang, Y., Bergler, S., and Hubral, P. (2001). Common-reflection-surface (CRS) stack for common offset. *Geophysical Prospecting*, 49(6):709–718.

Zhe, J. and Greenhalgh, S. A. (1997). Prestack multicomponent migration. *Geophysics*, 62(2):598–613.

Znak, P., Dell, S., Kashtan, B., and Gajewski, D. (2019). Identification and focusing of edge diffractions with wavefront attributes. In *SEG Technical Program Expanded Abstracts 2019*, pages 5060–5064. Society of Exploration Geophysicists.

Znak, P., Dell, S., Kashtan, B., and Gajewski, D. (2020a). Identification and focusing of edge diffractions with wavefront attributes. *Geophysics*, to be submitted soon.

Znak, P., Dell, S., Kashtan, B., and Gajewski, D. (2020b). Polarization-consistent stacking of multicomponent seismic data. *Geophysical Journal International*, under review.

Znak, P., Dell, S., Kashtan, B., and Gajewski, D. (2020c). Velocity model building by dynamic ray focusing. *Geophysics*, under review.

Znak, P., Kashtan, B., and Gajewski, D. (2017). Wavefront tomography by dynamic focusing. In *SEG Technical Program Expanded Abstracts 2017*, pages 1017–1022. Society of Exploration Geophysicists.

Znak, P., Kashtan, B., and Gajewski, D. (2018). Velocity model building by geometrical spreading focusing. In *SEG Technical Program Expanded Abstracts 2018*, pages 5188–5192. Society of Exploration Geophysicists.

Znak, P., Kashtan, B., and Gajewski, D. (2020d). Ray perturbation theory in wavefront-orthonormal coordinates: generally anisotropic 3D elastic solids. *Geophysical Journal International*, under review.

List of peer-reviewed publications

Journal papers

- Znak, P., Dell, S., Kashtan, B., and Gajewski, D. (2020c). Velocity model building by dynamic ray focusing. *Geophysics*, under review

- Znak, P., Kashtan, B., and Gajewski, D. (2020d). Ray perturbation theory in wavefront-orthonormal coordinates: generally anisotropic 3D elastic solids. *Geophysical Journal International*, under review

- Znak, P., Dell, S., Kashtan, B., and Gajewski, D. (2020a). Identification and focusing of edge diffractions with wavefront attributes. *Geophysics*, to be submitted soon

- Znak, P., Dell, S., Kashtan, B., and Gajewski, D. (2020b). Polarization-consistent stacking of multicomponent seismic data. *Geophysical Journal International*, under review

- Dell, S., Abakumov, I., Znak, P., Gajewski, D., Kashtan, B., and Ponomarenko, A. (2019). On the rule of diffractions in velocity model building: a full-waveform inversion example. *Studia Geophysica et Geodaetica*, 63:1–16

Expanded abstracts

- Znak, P., Kashtan, B., and Gajewski, D. (2017). Wavefront tomography by dynamic focusing. In *SEG Technical Program Expanded Abstracts 2017*, pages 1017–1022. Society of Exploration Geophysicists

- Znak, P., Kashtan, B., and Gajewski, D. (2018). Velocity model building by geometrical spreading focusing. In *SEG Technical Program Expanded Abstracts 2018*, pages 5188–5192. Society of Exploration Geophysicists

- Znak, P., Dell, S., Kashtan, B., and Gajewski, D. (2019). Identification and focusing of edge diffractions with wavefront attributes. In *SEG Technical Program Expanded Abstracts 2019*, pages 5060–5064. Society of Exploration Geophysicists

- Yang, P., Dell, S., Gajewski, D., and Znak, P. (2019). Improving focusing and estimation of excitation time for passive seismic events: sparse and limited-aperture data examples. In *SEG Technical Program Expanded Abstracts 2019*, pages 3096–3100. Society of Exploration Geophysicists

Acknowledgments

- I'm truly thankful to **Prof. Dr. Dirk Gajewski** for the opportunity to be a part of his team at the University of Hamburg. His smart vision and enthusiasm on seismic diffractions, wavefront attributes, and wave focusing inspired me a lot and became a leitmotif of my work. Prof. Gajewski revealed to me the art of scientific writing, that I'm very grateful for.

- **Prof. Dr. Boris Kashtan** is my teacher starting from my student time at the Faculty of Physics in St. Petersburg. He instilled in me an interest for wave physics. He is always eager to work with his students, no matter how much it takes. Prof. Kashtan teaches and helps, including myself.

- I acknowledge **Dr. Sergius Dell** for being always supportive and listening to my ideas, for his contributions to our papers, and for the amount of time he spent with me discussing the nasty technical details. His strong industrial background and programming skills were invaluable.

- I thank **Dr. Jan Walda** for assistance, for many motivating and philosophical talks, and for encouraging my ideas on improving stability and reproducibility of the wavefront tomography.

- I thank **PD Dr. Claudia Vanelle** for improving my presentations by continuous discussions and advices on the seminars.

- I thank **Paola Dal Corso**, **Dr. Ekkehart Tessmer** and **Dr. Ivan Abakumov** for helping to organize things in my early days in Hamburg.

- I'm grateful to **Dr. Alexander Bauer** for assistance and the wonderful road trip in California. The materials he prepared and kindly shared really simplified my life.

- Next, I want to note my office mates, **Leon Diekmann** and **Stefan Knispel**. With Leon, I traveled across California. I met Stefan in St. Petersburg, which I also appreciate a lot. Thank you both for being super friendly.

The most important support was given to me by my dearest people, my beloved, **Olga**, and my mother, **Inna**. Thank you for your love, understanding, and patience.

Eidesstattliche Versicherung

Hiermit versichere ich an Eides statt, dass ich die vorliegende Dissertation mit dem Titel Wavefront curvatures: dynamic ray focusing and diffraction classification selbstständig verfasst und keine anderen als die angegebenen Hilfsmittel – insbesondere keine im Quellenverzeichnis nicht benannten Internetquellen – benutzt habe. Alle Stellen, die wörtlich oder sinngemäß aus Veröffentlichungen entnommen wurden, sind als solche kenntlich gemacht. Ich versichere weiterhin, dass ich die Dissertation oder Teile davon vorher weder im In- noch im Ausland in einem anderen Prüfungsverfahren eingereicht habe und die eingereichte schriftliche Fassung der auf dem elektronischen Speichermedium entspricht.

Hamburg, den 9. Oktober 2019

Pavel Znak